Quasi-Static Contact and Sliding of Crystalline Materials

by

Tristan A. Sharp

A dissertation submitted to The Johns Hopkins University in conformity with the requirements for the degree of Doctor of Philosophy.

Baltimore, Maryland

December, 2015

Abstract

The mechanical properties of solid-solid contact are important in both engineered systems and in the explanation of everyday phenomena. However, predicting those properties from the surface geometry is a challenge for several reasons. The surface of a solid is typically rough, exhibiting effectively random geometry extending from the long-wavelength topography down to the atomic-scale structure. The surfaces often remain separated over most of their area. Even within a single region of contact, the solids can deform into one of many possible configurations.

In this thesis we use quasi-static molecular dynamics simulation to determine the mechanical properties of crystalline contacts. We help develop the Green's function molecular dynamics method to enable simulations to reach the necessary wide range of length-scales. We focus on simple interatomic potentials and models to isolate the underlying mechanical phenomena. We design simulations that test with atomic-scale resolution the normal contact of rough solids and the quasi-static sliding of clean crystalline contacts.

We find for rough solids at typical normal loads that the average surface separation decreases as a logarithm of load. Correspondingly, the mechanical stiffness associated with the rough surface is proportional to the load. In both the continuum case and the atomistic case, the fraction of the surface in repulsive contact increases approximately linearly with load. In the atomistic case, the dimensionless proportionality constant can be increased several times by nanometer-scale features. Surface steps frequently found on crystalline materials can dramatically increase con-

ABSTRACT

tact area by increasing the amount of plastic rearrangement and, in turn, decreasing the average surface stress.

The static friction of a contact between elastic crystals depends sensitively on contact size, crystal orientation, and the microscopic friction law at the interface. In non-adhesive commensurate simulations, we show that the friction coefficient decreases over several decades as $(a^2/Rb)^{-2/3}$ where a is the contact radius, R is the sphere radius, and b is the Burgers vector of dislocations that are produced. Incommensurate contacts, despite exhibiting complex deformations while sliding, show surprisingly universal characteristics in the large size limit. We discuss the elastic breakdown of superlubricity by showing the rapid rise in friction from lowering the material modulus of large incommensurate contacts.

Primary Reader: Professor Mark O. Robbins, Johns Hopkins University

Secondary Reader: Professor Michael L. Falk, Johns Hopkins University

Acknowledgments

It has been my good fortune to work with some of the field's leading researchers.

Foremost and with deep gratitude I thank my advisor, Professor Mark O. Robbins, who provided guidance, insight, and analysis during this research program. Mark opened many doors for my research at every stage, through his scientific support, leveraging of institutional resources, and engagement in the scientific community.

Dr. Lars Pastewka co-advised my research during many important parts of these thesis projects. He also hosted my stay at the Fraunhofer Institut Werkstoff Mechanik in Freiburg, Germany, where I conducted part of the research. Lars generously shared his sharp insights and scientific skill for which I am incredibly thankful and which made many parts of this work possible.

Among my fellow graduate students in the group, I want to acknowledge my friend Ting Ge who shared essential academic and life wisdom with me. K. Michael Salerno generously helped me get started in condensed matter physics research. Lin Guo was a steadfast teammate at the forefront of nano-scale mechanics research, providing many fruitful discussions. I am thankful for the conversations with Thomas O'Connor, who shared his knowledge about broad ranges of condensed matter topics. Joel Clemmer's insightful questions improved the work discussed in this thesis on multiple occasions. Additionally, Dr. Vikram Jadhao provided valuable mentorship in academic science; thank you.

My other graduate school friends, cohorts, and colleagues provided me a

foundation on which life as a graduate student could be defined. It has meant a lot to me.

My parents, Lisa M. Rhoads Sharp and Dale O. Sharp, through compassion, work ethic, intelligence, and commitment to their convictions, gave me the gift of opportunity. They have been there for me the whole way and I wish everyone in the world could know people that are so wonderful. The entirety of my family has been the greatest team for me and I am joyful to be a part.

This work was supported by the National Science Foundation (IGERT Fellowship Grant 0801471 and grants OCI-0963185, DMR-1006805, and DMR-1411144); the Johns Hopkins University Department of Physics and Astronomy (The Kerr Fellowship and a Teaching Assistantship); the Air Force Office of Science Research (grant FA95500910232); and the Deutscher Akademisches Austausch Dienst (DAAD Research Grant at the Fraunhofer Institut Werkstoff Mechanik Freiburg).

Sections of Ch. 3 are reprinted with permission from L. Pastewka, T. A. Sharp, and M. O. Robbins, *Physical Review B*, vol. 86, no. 7, p. 075459, 2012. Copyright 2012 by the American Physical Society. `http://dx.doi.org/10.1103/physrevb.86.075459` Ch. 4 is reprinted with permission from S. Akarapu, T. Sharp, and M. O. Robbins, *Physical Review Letters*, vol. 87, no. 11, p. 116101, 2001. Copyright 2001 by the American Physical Society. `http://dx.doi.org/10.1103/PhysRevLett.106.204301`

Dedication

This work is dedicated to all people trying to do what they believe is right for the world.

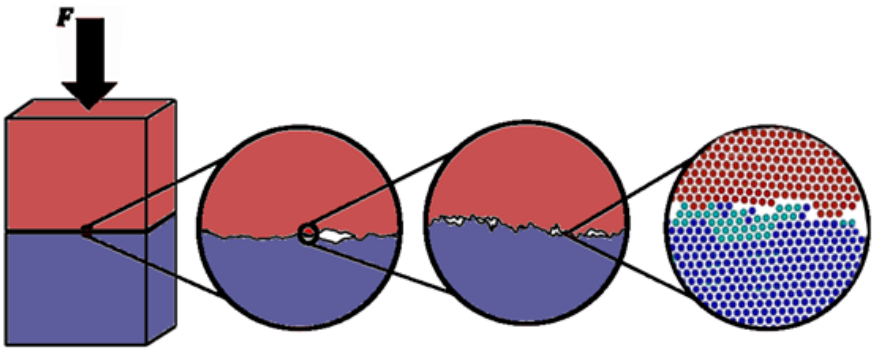
F

Contents

List of Figures

Chapter 1

Introductory remarks

1.1 Impetus for research on atomic-scale contact mechanics and friction

Nanotechnology aims to provide new capabilities through engineering on sub-micron length-scales and can lead to the development of microscopic devices with applications ranging across fields such as medicine and energy. However, one obstacle to designing small machines is that aspects of continuum solid mechanics theory break down at the atomic scale. That is a problem, since continuum solid mechanics is the standard tool used to describe how solids deform. Stress, strain, pressure, and contact area are examples of familiar quantities defined conveniently within the continuum framework. But at small scales, the discrete atomic geometry even precludes unique definitions of these quantities. Insight is needed into how to treat the mechanics of atomic systems.

One part of continuum theory that fails in atomic-scale systems is contact mechanics.[1] Contact mechanics focuses on the deformations near the region where two solids meet. It is the conceptual starting point for calculations of friction, adhesion, interfacial stiffness, electrical contact, and sealing. These interfacial properties, while already important in macroscopic systems, become even more dominant in small systems. As the system size is reduced, surface effects that scale with the area become larger than bulk effects that scale with the volume. It is also in small systems that continuum approximations for these properties become especially ineffective.

1.2 This thesis

This thesis describes original computational research projects targeting a better understanding of microscopic contact and friction. Underlying the work is the recognition that typical solid surfaces are rough. Surface roughness means that contact only occurs at separated regions called asperities. Research questions are divided into questions about a single asperity and questions about rough (multi-asperity) contacts. Models of single asperities connect with scanning probe experiments like atomic force microscopy which have provided much of the experimental insight into atomic scale contact.[2] Meanwhile models of full rough contacts can help explain ubiquitous phenomena in engineered devices or in everyday experiences.

The rest of this chapter, Ch. 1, describes the context of the research. Ch. 2 provides theoretical background that supports the remaining chapters. Ch. 3 explains the Green's function molecular dynamics simulation method, emphasizing our extensions to it. Ch. 4 describes the contact stiffness of randomly rough continuum surfaces. Ch. 5 reports on contact between randomly rough atomic surfaces. Ch. 6 and Ch. 7 explain the static friction of spherical crystalline asperities. Ch. 8 synthesizes the conclusions with implications for solid friction in general.

1.3 Contact and friction as a classic problem

This work is within the field of tribology, which addresses questions related to the friction and wear between solids. The history is long, as friction was studied already by da Vinci, Amontons, and Coulomb.[3] Early ideas about simple geometrical origins of friction were discarded as research revealed the complexity of friction in different systems. Beginning in the 1960's, the British government recognized the economic importance of the research

and helped support the emerging science under the name tribology.[4] At first, primarily simple experiments and phenomenological research occurred under the title of tribology. At present, advances in experimental techniques, theory, and computer modeling are providing a more fundamental understanding at a time when potential application to new mechanical systems is growing.

Appreciation of the problem of solid-solid friction comes from recognizing the multiple length scales that affect friction. Surface roughness on many objects is often approximately random self-affine fractal over decades of lengths.[5,6] There is long-range elastic coupling between different parts of the system.[7,8] Moreover, even atomic-scale structure affects what elastic deformations may occur (*c.f.* Refs. 9–12). Chemical bonding and electronic degrees of freedom at the interface can be important,[13] as well as what energy dissipation can occur within the bulk.[14] Friction, an indispensable concept in macroscopic systems, is a complex emergent phenomenon from smaller-scale processes.

In much of this work we focus on one of the most promising systems of study, bare crystalline materials. Surfaces are often not bare, and in fact loose particles trapped between solids, termed "third bodies", can often be responsible for solid-solid friction.[9] However, bare crystalline lattices serve as a fundamental starting place to understand the interplay of atomic-scale interactions and long-range elastic interactions in contact mechanics. The regular ordering of atoms makes the systems more transparent to analysis. These systems promise some of the clearest insight into ubiquitous mechanisms of friction. Moreover, bare crystal sliding occurs in situations ranging from fundamental force microscopy experiments[15,16] to metal-on-metal sliding in industrial applications.[17] Finally, precise engineering in future small devices may also attain very low friction coefficients from "structural-lubricity" of bare crystals.[18]

A deeper understanding has come hand-in-hand with more powerful computers and computational techniques. In this work we adapt the method of Green's function molecular

dynamics (GFMD), initiated for tribology by Müser and Campaña.[19] The method allows large portions of the atomic lattice to be *integrated out* of an MD simulation, reducing computation time. The technique, implemented on graphical processing units (GPUs), makes it possible to simulate the necessary system sizes, effectively consisting of billions of atoms. We hope that the results presented here will be useful for future research into the properties of rough contact and the mechanisms of friction.

Chapter 2

Background: Contact mechanics, friction, and lattice dislocations

This chapter summarizes work useful to the understanding of the following chapters and may be referred to as needed.

2.1 Continuum pictures of single-asperity sliding

Standard textbooks such as Johnson's *Contact Mechanics* (Ref. 20) describe the continuum picture of the stresses that arise between contacting solids. In this section we briefly mention a few key results from that reference. Using isotropic linear elasticity, each solid has a Young's modulus E, Poisson ratio ν, and stress field $\boldsymbol{\sigma}$ within its domain. The dot product of the 3×3 tensor $\boldsymbol{\sigma}$ with the surface normal direction is the interfacial traction, $\boldsymbol{\tau} = \boldsymbol{\sigma} \cdot \hat{\boldsymbol{n}}$, and the component of $\boldsymbol{\tau}$ normal to the interface is the normal pressure, $p = \boldsymbol{\tau} \cdot \hat{\boldsymbol{n}}$.

2.1.1 Hertz - normal pressure and contact radius

Many geometries can be mapped to a sphere contacting a large, flat substrate.[20] This is the case, for example, for two lightly-contacting, curved surfaces forming a smooth asperity. The pressure under a sphere of radius R at low pressure follows the analytic solution given by Hertz:[20]

$$p(r) = \frac{3F_z}{2\pi a^2}\sqrt{1 - r^2/a^2} \qquad (r \leq a) \tag{2.1}$$

$$a = \left(\frac{3F_z R}{4E'}\right)^{1/3} \tag{2.2}$$

where r is the distance from the center of the contact, a is the contact radius, and F_z is the normal load. The pressure is zero outside the contact, at $r > a$. The elastic parameters of each solid enter only as the contact modulus $E' \equiv ((1-\nu_1^2)/E_1 + (1-\nu_2^2)/E_2)^{-1}$ where subscripts refer to each of the two solids. Since only E' enters in the equations above, it is often convenient to simulate with an infinitely-stiff sphere, $E_2 \to \infty$. Then the Hertz pressure produces surface displacements in the contact

$$u_z = \frac{\pi p_0}{E' 4a}(2a^2 - r^2) \qquad (r \le a) \tag{2.3}$$

$$u_r = -\frac{(1-2\nu_1)(1+\nu_1)a^2 p_0}{3E_1 r}(1-(1-r^2/a^2)^{3/2}) \qquad (r \le a) \tag{2.4}$$

which follow the shape of the sphere.

2.1.2 Uniformly displaced circular contact

After applying a normal load to the two solids to produce a contact radius a, consider applying a lateral load F_x. If the upper solid is very stiff and the surfaces remained pinned in the contact, the contacting surface of the substrate will be uniformly displaced from its initial position. An x-traction of the form

$$\tau_x = q_0/\sqrt{1-r^2/a^2} \tag{2.5}$$

with magnitude $q_0 \equiv \frac{F_x}{2\pi a^2}$ produces the required surface displacement within the contact (at $r \le a$):[20]

$$u_x = \pi(2-\nu)q_0 a/(4G) \qquad \text{(a constant)} \tag{2.6}$$

$$u_y = 0 \tag{2.7}$$

$$u_z = -\frac{(1-2\nu)q_0 a}{2G}(a/r - \sqrt{a^2-r^2}/r) \tag{2.8}$$

A uniqueness theorem[20] guarantees that τ_x as given above is the unique traction to create a laterally-displaced contact. Note the singularity in τ_x at the contact edge, $r \to a$. Near the edge, the geometry is the same as at a crack tip, and the stress singularity has the same well-known inverse square-root form.

A related geometry is a circular contact displaced uniformly in the normal direction. This occurs due to normal loading of a rigid flat punch on a flat elastic solid. The normal pressure has the same form as above, $p = p_0/\sqrt{1 - r^2/a^2}$ where $p_0 \equiv \frac{F_z}{2\pi a^2}$ and there is the same square-root singularity at the edge. Within the contact ($r \leq a$) this produces a uniform normal displacement $u_z = \pi(1 - \nu^2)p_0 a/E$.[20]

2.1.3 Mindlin model - local friction coefficient

The Cattaneo-Mindlin model[21] describes the case where the solids mentioned above can locally unpin and slip wherever the lateral traction is above a threshold which may be called τ_{max}. In tribology it is often found[9] that the shear strength of the interface can have a dependence on pressure and may be written $\tau_{max} \approx \tau_0 + \alpha p$. Here, τ_0 is independent of pressure, and α is a dimensionless constant. The Mindlin model assumes that the first term is negligible, so that the traction required to slip follows Amonton's law: $\tau_{max} = \alpha p$.

Because the Hertzian pressure goes to zero at the edge, the edges in the Mindlin model can slip easily while the center remains pinned. The radius of the pinned region is $c = a(1 - F_x/(\alpha F_z))^{1/3}$. Outside the pinned region, there is an annulus $c < r < a$ that has slipped, where the sliding-direction traction remains at $\tau_x = \alpha p$. Continued incremental lateral loading causes the pinned region to shrink until the whole surface has slipped. The maximum traction occurs when steady-state sliding is reached, and everywhere $\tau_x = \alpha p$.

2.1.4 Savkoor model - pressure-independent friction and fracture

The Savkoor model[22] is an example of an alternative to the Mindlin model and connects to work in Ch. 6 and Ch. 7. The Savkoor model assumes an interfacial shear strength

independent of pressure. Again there is a center region that is pinned, and outside of that, a slipped annulus where the traction remains at $\tau_x = \tau_{max}$ but now $\tau_{max} = \tau_0$ is a material constant. At the edges of the pinned region, the situation is taken to be the same as at a crack tip. To unpin more of the contact, lateral loading is increased until a fracture criterion is met, *i.e.* that the stress intensity factor exceeds a critical value.[22] Increasing the lateral load makes the crack front propagate, and the annulus region of slip grows inward. The maximum friction force occurs before the contact is entirely unpinned. Once everything is unpinned and in steady state sliding, the traction is everywhere $\tau_x = \tau_0$.

2.2 Dislocations

Dislocations are topological defects in a crystal lattice discussed in standard texts (*c.f.* Refs. 23–25) and they become important in much of the analysis in this thesis. They are characterized by their Burgers vector, $\boldsymbol{b}$, and their line direction, $\hat{\boldsymbol{\xi}}$. Edge dislocations, where $\boldsymbol{b}$ and $\hat{\boldsymbol{\xi}}$ are perpendicular, can be considered as the insertion of an additional half-plane of atoms into the crystal lattice. A screw dislocation is the case when $\boldsymbol{b}$ and $\hat{\boldsymbol{\xi}}$ are parallel (or anti-parallel), and for other angles the dislocation is called mixed character.

Dislocations create long-range elastic fields in the solid. At long distances, the stress and strain decay inversely with the distance from the dislocation line segment,[24] $\sim 1/r$. The singularity at the origin is regularized by non-linearities on the length scale b_{core} that characterizes the dislocation core width. The total dislocation energy is then the elastic plus the core energy.[26]

Continuum analysis shows that dislocations move in response to the stress field. The configurational force on an isolated dislocation segment of length ξ in an infinite uniform crystal lattice is given by the Peach-Koehler law, $F = (\boldsymbol{b} \cdot \boldsymbol{\sigma}) \times \boldsymbol{\xi}$.[23] The dislocation moves if the component of the stress $\boldsymbol{\sigma}$ that drives the dislocation in its glide plane exceeds a threshold called the Peierls stress, $\tau_{Peierls}$. The stress $\boldsymbol{\sigma}$ may be due to other dislocations,

image forces from free surfaces, or externally applied stress. Not included in the Peach-Koehler law is that a gradient in corrugation amplitude or elastic modulus also produces a force on a dislocation. This occurs in simulations in Ch. 7.

Dislocations that naturally form between two slightly dissimilar lattices are called misfit dislocations.[25] For example, consider a large contact between lattices that are identical and aligned. Atoms of one solid are all in registry with atoms of the opposite solid. If the lattice constant of one of the solids is slightly increased, the resulting surface mismatch is accommodated by misfit edge dislocations. If instead one of the solids is slightly rotated, producing a twist boundary, the mismatch is accommodated by misfit screw dislocations. Dislocations between mismatched lattices figure prominently in Ch. 6 and it is interesting to consider what is the stress field $\boldsymbol{\sigma}$ that creates and moves the misfit dislocations. The stress field required to force two slightly dissimilar lattices to be commensurate would constitute a large amount of elastic energy. This is the stress field $\boldsymbol{\sigma}_o$ in which it is energetically favorable to introduce dislocations. The $1/r$ stress fields created by the dislocations reduce the otherwise large stress and lower the system energy. The total stress, $\boldsymbol{\sigma}$, that drives a dislocation is the stress field needed to drive the dislocations out, $\boldsymbol{\sigma}_o$, combined with the stress from other dislocation segments, image forces from free boundaries, and any additional applied stress.

2.3 Dislocation mediated sliding mechanism of Hurtado and Kim

Hurtado and Kim revisited single-asperity sliding from a lattice dislocation viewpoint.[27,28] They considered commensurate contacts. If lattice dislocations can be accommodated at the interface, then the rise in stress at the edge discussed in Sec. 2.1 can nucleate a dislocation. Hurtado and Kim use a nucleation criterion that implies that the traction of the pinned-surfaces must reach a sufficient value at a distance d^* (a material parameter) from the edge. Due to the dominating $1/\sqrt{d^*}$ singularity,[29] this nucleation criterion leads to an average

traction through the contact at the time of nucleation that decreases with contact radius, $\tau_{fric} \sim (a/d^*)^{-1/2}$ where $\tau_{fric} \equiv F_x/\pi a^2$. The analysis predicts that τ_{fric} would transition to a constant at both small contact radius[27,29] ($a < d^*$) and very large contact radius[28] (when τ_{fric} drops to $\tau_{Peierls}$). The reason for the saturation at small contact radius is that no dislocation can fit in the contact; the surfaces are effectively rigid on that length scale and the full contact slides at the friction stress τ_{fric}. The reason for the saturation for large contact radius is that there will be many dislocations in the contact which, to move, requires a traction equal to $\tau_{Peierls}$ to be applied.

2.4 Models of dislocations

2.4.1 Frenkel-Kontorova model

The Frenkel-Kontorova (FK) model is a simple 1D model that exhibits an analog to dislocations in 3D crystals.[30] N particles are linked in a line by N linear springs of stiffness k and equilibrium spacing b'. There are periodic boundary conditions so that the last and first spring are also connected and initially sit at the equilibrium spacing. A sinusoidal force f is applied so that at position x the force is $f(x) = f_{max} sin(2\pi x/b)$ where f_{max} is a constant. A technical aside is that Nb'/b must be a whole number so that the force field is continuous across the periodic boundary.

If N is sufficiently large and b and b' are only slightly different, then kinks form in the system, analogous to the dislocations in 3D crystals. The characteristic width of a static kink is given by[30] $b_{core} = b\sqrt{kb/(\pi f_{max})}$. Analysis is simpler when $b_{core} \gg b$ and the system reduces to the discrete form of the Sine-Gordon equation.[30] Then the atomic displacements within the kink are $(2b/\pi)\tan^{-1}(\exp(-x/b_{core}))$.[30] The Peierls force required to move a kink decreases with b_{core} as $(b_{core}/b)^2 exp(-\pi^2 b_{core}/b)$. If there are two well-separated kinks in the chain, the force between them falls exponentially with separation.[25]

The FK model is also useful for analogies with structural superlubricity. When

b_{core} becomes sufficiently large (*i.e.* f_{max} becomes sufficiently small), the Aubry transition occurs and there is perfectly frictionless sliding of the infinite chain.[30] That is, the ground state energy is invariant to mean translations of the particles. Near the transition at the critical force f^c_{max} the Peierls force scales as a power-law[31,32] of $(f_{max} - f^c_{max})$. If N is not infinite or one of the springs is removed to create free ends, no frictionless sliding occurs.[30]

2.4.2 Peierls model of the dislocation core

The Peierls-Nabarro (PN) model is a foundational model of a dislocation core in a 3D solid discussed in standard textbooks (*c.f.* Ref. 23). It is somewhat similar to the FK model of a kink.[25] In the PN model, the particles may be analogous to atoms of a crystalline surface and the sinusoidal force may be considered to be the corrugation of the opposing crystalline surface. Then the nearest-neighbor spring interactions between the atoms are replaced by interactions of 3D linear elasticity. That is, a bond stretched Δb at x' corresponds to a strain $\Delta b/b$ which, from linear elasticity in this geometry, produces a stress $\sigma_{xy}(x) = (G/\pi(1-\nu))(\Delta b/(x-x'))$ at position x. The amplitude of the corrugation is assumed to be related to the shear modulus by $f_{max} = Gb/(2\pi h)$ where h is the vertical separation of the atomic planes.

The PN model produces predictions that are widely used for qualitative analysis of dislocations.[25] The atomic displacements within the dislocation are $b/2 - (b/2\pi)tan^{-1}(x/b_{core})$ and $b_{core} = h/(2-2\nu)$. The Peierls stress to move the dislocation is $(2G/(1-\nu))exp(-4\pi b_{core}/b)$. Unsurprisingly, the force in the PN model between two dislocations separated by a large distance r_0 agrees with the continuum elastic analysis; that is, the force falls as $1/r_0$.

2.4.3 The Γ-surface (Generalized stacking fault energy)

The dislocation core width and the configuration of atoms within the core are determined by the atomic interactions. Most materials do not have a sinusoidal force law as used in the Peierls-Nabarro model, and it is useful to consider what the effective force law is and

what determines it.

An approximation for the effective force law comes from the Γ-surface or generalized stacking fault energy.[33] To define the Γ-surface, the perfect crystal lattice is divided into top and bottom halves by a cutting plane. Both lattice-halves of atomic nuclei are held rigid. The top half is displaced laterally quasi-statically, while allowing the normal displacement to relax to match the applied external pressure. The energy (divided by interfacial area) as a function of lateral displacement through the unit cell is the Γ-surface. The Γ-surface is therefore periodic with the surface unit cell and has minima near any stable stacking fault configurations. In general the Γ-surface will have dependence on normal pressure, $\Gamma(x, y, p)$, and may be Taylor expanded in p.

Using the Γ-surface to determine the force law implies several assumptions. In some materials b_{core} is not large compared to the Burgers vector b, so lattice distortions are not small and may be out-of-plane. But using the Γ-surface implies that at any place in the dislocation core the atoms approximate the rigid translated lattice configuration. Moreover, "going up and over atoms" may locally raise the normal pressure, requiring use of a Γ-surface of a different pressure. If these corrections can be ignored, then the magnitude of the maximum slope of the Γ-surface along the sliding path can be used as f_{max}/b^2 in the Peierls-Nabarro model.

2.5 Commensurability and sliding of flat crystalline surfaces

The commensurability of two crystalline surfaces affects the friction between them during sliding. Commensurate surfaces are those that systematically share a common periodicity.[18] This is illustrated simply with the FK model of two lattices (of lattice constants b and b') sliding relative to one another when the spring constant k is infinite. In this case, the FK chain slides rigidly and, if $b' = b$, then the sinusoidal force contributes to all atoms coherently during sliding. If the ratio b'/b is a rational number, then the sinusoidal force will contribute

coherently on the length scale of the common period of b and b'. Therefore when b'/b is a rational number, the system is called commensurate. If however b'/b is irrational, then all phases of the sinusoidal force will be sampled equally as the system becomes large, and the force systematically cancels. Such a system is incommensurate.

The same distinction is true for sliding of the 2D interface between 3D crystals. A contact between two lattices is commensurate if the atoms of one surface all sample the same forces at the same time during rigid sliding. More generally, if the two surfaces share a common periodicity in the sliding direction, then periodically-tiled regions of the surface contribute coherently and the contact is commensurate. In contacts larger than the common period, the static friction force F_s grows linearly with the contact area $F_s \propto A$. Only if the sampled sliding paths show no systematic periodicities, so that all phases are sampled uniformly, is the contact incommensurate. Each atom contributes incoherently and the friction does not rise as quickly with area. The static friction is found to go as $F_s \propto A^\gamma$ where $0 < \gamma < 1.0$ depending on contact shape.[16] Simulations in Ch. 6 find that only the upper bound for static friction decreases with power-law scaling, whereas dramatic drops at special sizes can show friction coefficients many decades smaller.

2.6 Superlubricity

The term superlubricity was coined by Hirano and Shinjo in 1991.[34,35] In that work they found very low friction in simple computational models of sliding flat, rigid, incommensurate crystalline latices. They simulated with small systems ($L \sim 100$) with periodic boundary conditions and no free edges. The assumption of rigidity was reduced by allowing the surface atoms to deform slightly while holding rigid the second layer of atoms below the surface. As long as the elastic compliance was not too great, no instabilities occurred during sliding. This indicates that kinetic friction can go to zero as the sliding velocity goes to zero.[18] A related observation is that the ground state showed evidence of being invariant to relative

translations of the two solids in certain directions or in all directions.[34] This is in analogy to the Aubry transition of the FK model. If the rigidity was reduced even further, frictionless sliding was lost in all directions.

Superlubricity has been investigated in more detail since then. The term structural lubricity is used to describe low static friction whereas superlubricity may also refer to low kinetic friction.[18] Studies of the size effects started with a focus on the rigid limit.[36] Experiments also showed promising indications that the phenomenon could be realized with nano- and micro-scale surfaces (*c.f.* Refs. 12, 16, 37).

Many complications can arise in real systems that destroy the low friction. Sliding flakes of graphite can deform out-of-the-plane and pin at their edges .[38] Torques will tend to twist the contact to commensurate configurations .[39] Loose contaminant atoms can pin the surfaces.[9] Finally, elastic distortions can allow the surface to lock together. The role of this mechanism in incommensurate 3D solids is the subject of Ch. 6.

2.7 Surface topography of rough surfaces

Many surfaces are well-described as random and self-affine fractal.[40–42] That is, scaling the geometry in lateral and normal directions by different factors creates a surface with the same statistical properties as the original surface. One reason that this property of surfaces is common is that many physical processes like brittle fracture or particle deposition can naturally produce self-affine scaling.[43,44] Self-affine surfaces have a root-mean-square (rms) change in height dh that scales as a power law of the rms change in lateral position, x_0. That is, $dh \sim (x_0)^H$. H, called the Hurst exponent, is frequently measured to be between 0.5 and 0.9 for solid surfaces.[42] The power spectrum of the height follows a power law $C(q) \equiv \langle |\tilde{h}(\boldsymbol{q})|^2 \rangle \sim q^{-2-2H}$ where $\tilde{h}(\boldsymbol{q})$ is the Fourier transform of the height. In real systems the scaling only holds between two limiting wavenumbers, q_{min} and q_{max}. In continuum simulations, it is common[45] to have the spectrum exactly follow that scaling, then go to a

constant at wavenumbers below q_{min} and go to zero above q_{max}. It is also common to have random phases for each Fourier component drawn from a uniform distribution.

2.8 Rough surface contact mechanics

2.8.1 Independent-asperity theories of continuum elastic rough contact

The Greenwood-Williamson model laid the groundwork for a range of independent asperity models. "Independent" means that the asperities do not interact elastically. In the Greenwood-Williamson model, each asperity is approximated as Hertzian, and uses the normal load *vs* displacement of a spherical contact.[6,22] To describe the topography, the model takes as input a sphere radius R and an initial distribution of asperity heights above the surface. The model may then be used to predict the contact area, displacement, and gap between the surfaces as a function of load. Of interest is the relationship between contact area and load for Gaussian-shaped distributions of height. If the surface $h(\boldsymbol{x})$ has rms slope $h'_{rms} \equiv \sqrt{\langle |\nabla h(\boldsymbol{x})|^2 \rangle}$, then the approximate relation for contact area at low contact area is shown[46] to be $AE' = \kappa F_z / h'_{rms}$ with dimensionless proportionality constant $\kappa = \sqrt{2\pi} \approx 2.5$.

2.8.2 Continuum elastic rough contact including interactions

Simple statements can be made about rough contact that do not assume independent asperities, or even bother identifying what the asperities are. In an isotropic, linear elastic, continuum description we recall that there is a mapping from contact between two rough elastic solids to a simpler problem: contact between one rough-rigid and one flat-compliant solid. The mapping may be done if the roughness is small, and the mapping preserves the gap and the contact modulus. The only salient variables then are the normal load F_z, contact area A, a modulus like the contact modulus E', and the geometry of the roughness.[7] The quantity F_z/AE' is dimensionless and so must depend on the roughness in a dimensionless way. For a linear treatment of randomly rough surfaces, the simple statistical

quantity with the allowed properties is the rms slope, h'_{rms}. Random rough surfaces at low contact area therefore may be expected to follow $AE' = \kappa F_z/h'_{rms}$ with some dimensionless proportionality constant κ. This is found in the Greenwood-Williamson model as well as in several extensions to it.[5,47,48] Note that the strain needed to conform to the rough surface is approximately equal to the local surface slope, h'_{rms}, so it is natural that the mean normal pressure F_z/A is proportional to h'_{rms}.

Another useful relation for contact theory is the elastic energy to deform the surface of a solid. If the elastic surface is deformed an amount $u(\boldsymbol{x})$, the elastic energy is given by $U_{el} = \frac{EA_0}{4(1-\nu^2)} \int d^2q q C(q)$.[45] Here the power spectrum is the Fourier transform of the height auto-correlation function, $C(q) = \frac{1}{(2\pi)^2} \int d^2x \langle u(\boldsymbol{x}) u(\boldsymbol{0}) \rangle e^{-i\boldsymbol{q}\cdot\boldsymbol{x}}$. More recent theories of rough contact made progress building on these relations.

2.8.3 Persson's scaling theory of rough contact

Persson developed a theory that includes elastic interactions approximately.[48–50] A brief account may be given as follows.

At first, only the zero spatial-frequency (the mean height) of the topography is considered. The distribution of pressure on the surface is a delta function at the mean pressure. Then, additional low spatial-frequency topography is considered. The surface spectrum is taken to be zero at wavenumbers above some low value q_0. q_0 may be called the magnification, since smaller features are not included. If each component of the spectrum has random phase, the height distribution is approximately Gaussian. Being long wavelength, the surface remains in full contact, and, being linear, the pressure distribution is also a Gaussian centered at the mean pressure. The spreading of the delta function constitutes the Green's function solution to a differential equation for how the pressure changes with increasing magnification, q_0. The differential equation is the one-dimensional diffusion equation where magnification takes the role of time. Then, since negative pressures are not

allowed in repulsive contact, a boundary condition is applied to the diffusion equation that the distribution of pressures be zero at the origin, $p = 0$.

For self-affine surfaces, this method gives area proportional to load with proportionality constant $\kappa = \sqrt{8/\pi} \approx 1.6$. Extensions to the theory approximately account for adhesion, predict surface separation, and predict the spatial distribution of pressure.

Chapter 3

Green's function molecular dynamics

Contact and friction between solids can depend on atomic-scale features, large-scale elastic deformations, and multi-scale surface topography. This often requires that large systems be considered, but large systems can be prohibitively time-consuming to simulate directly. This chapter describes how we met this challenge by further developing the method of Green's function molecular dynamics simulation[19,51,51] (GFMD). After an introduction, Sec. 3.2 describes GFMD for the case of atomic pair potentials. Sec. 3.3 explains the extension to many-body potentials. Sec. 3.4 describes procedures to solve for the Green's function from the dynamical matrix. Secs. 3.5-3.7 discuss implementation and testing of the method with emphasis on contact mechanics problems. The last section makes connection with the Green's function of continuum elasticity, important for later chapters.

3.1 Introduction

A large number of interfacial problems are challenging to simulate using brute force methods. The response depends on details of atomic interactions at the interface, and also on long-range elastic deformations of the bulk. This situation arises in studies of contact and friction, in scanning probe experiments[1,52] or between atomically rough surfaces,[42,53] and in fracture of brittle[54] or ductile[55] materials. The elastic response of the supporting solid can also appreciably influence chemi- and physisorption processes at crystal surfaces, including stress corrosion[56] and thin film growth.[57]

There has been great recent interest in accelerating simulations by treating each spatial region with the modeling method that most efficiently captures material response.[54–56,58–61]

An explicit atomistic treatment is essential at the interface where gradients in stress, strain and chemical composition may be large. Long-range elastic deformations in the bulk extend to depths that are comparable to the length scale of variations along the interface L, but the strains at these depths may be small enough to treat with models that assume slow variations and/or linear response.

A variety of methods for approximating the response of the substrate have been proposed and many are reviewed and contrasted in Refs. 58 and 60. Most treat the interface atomistically and transition to a finite element description for the bulk. In general this introduces ghost forces near the interface or leads to a model with no underlying Hamiltonian.[58,61] There is an alternative approach that avoids both problems. An atomistic description is retained throughout the system, but atomic interactions in the substrate are treated in the harmonic approximation. The linear response of the substrate can then be efficiently calculated using Green's function methods.

3.1.1 Previous work

Traditionally, Green's function techniques have been used to describe the elastic response of the infinite or semi-infinite bulk to inclusions such as point, line or planar defects by invoking the Dyson equation.[62–65] Recent extensions of this approach have included a full nonlinear atomistic description of the defect coupled to a harmonic lattice[66] that smoothly connected to a continuum description at large distances.[67–69] Green's function techniques have also been employed to solve boundary value problems in continuum elasticity.[70–72] An atomistic system can be coupled to a continuum boundary,[69,73] but the strain field will only match exactly for long wavelength deformations. Recently, Campaña and Müser[19] showed that a Green's function approach can be used for the solution of atomic-scale contact problems. In their work, the surface Green's function is evaluated from a fluctuation-dissipation theorem. Assuming that the underlying potential is harmonic, the mean response is not affected by

these fluctuations. A similar method was used to find the dynamic Green's function in complex geometries by Cai et al.[74] Most applications of the Green's function approach to contact problems[19,53,75–77] have used the analytic solution[78] for simple cubic lattices, or the isotropic continuum Green's function.[42,79] An implementation of the code has been ported to the widely used molecular dynamics package LAMMPS.[51,80,81]

There are two difficulties with the Green's function approach as it has been implemented for contact problems. One is that the formulation does not include all the atomic forces near the interface between explicit and harmonic regions. The neglected forces vanish in the special case of nearest-neighbor interactions at zero pressure, which has been considered in most past work. In other cases, these forces must be included or the coupled system does not satisfy Newton's third law. Neglecting them creates problems similar to ghost forces in other methods[58] and creates artificial surface relaxation at the elastic/explicit interface. The second difficulty is that calculating the Green's function with the fluctuation dissipation theorem can require significant computation. All L^3 atoms in the substrate must be included and sampling long wavelength modes correctly requires times that are at least of order L.[82] Thus, while the Green's function only needs to be calculated once, it may require more computational effort than calculations using it.

3.1.2 Rigorous GFMD

In this chapter we describe an approach that includes all interatomic forces near the interface and allows rapid calculation of the elastic Green's function for an arbitrary interaction. Fourier transforming the equations of motion in the plane of the substrate decouples the equations for each in-plane wavevector $\vec{q}$.[83] The remaining coupling between atomic planes of the substrate is effectively one-dimensional and can be solved for any crystalline solid without the need of separate molecular dynamics simulations and fluctuation-dissipation analysis. Prescriptions for solving the equations using a transfer matrix formulation[83,84]

and a renormalization transformation[85,86] are described. Full dynamical equations are developed for a number of crystals and interactions, and then implemented for static problems. The static Green's function can be precomputed in a time that is $O(L^2 \ln L)$ and thus represents a negligible fraction of the total computation time for contact problems. The only approximation intrinsic to this construction is linear response sufficiently far below the surface.

To demonstrate that the resulting approach provides seamless boundary conditions for interfacial calculations we apply the method to three cases in Sec. 3.7. The first is relaxation of the spacing between atomic planes near a free surface. Full atomistic results are reproduced by our method, but previous formulations do not include the forces that produce surface relaxation.[19,51] We next consider Hertzian contact between a rigid sphere and elastic substrate and show that a few planes of explicit atoms on the Green's function layer allow the anharmonic corrections to Hertz theory to be captured. Our last example is contact of a randomly-rough, stepped surface with a flat substrate. A few planes of explicit atoms allows both anharmonic effects and subsurface plasticity to be captured up to relatively high contact areas.

3.2 Elastic surface Green's functions

We start from the total energy $E(\{\vec{r}_{i\alpha}\})$ of the crystal as a function of the positions of all atoms $\vec{r}_{i\alpha}$. The energy may have arbitrary form and could be replaced by the free energy to model the response at finite temperature. Atoms are then partitioned into three types (see Fig. 3.1): Substrate atoms, boundary atoms and explicit atoms. The explicit atoms may be anything that interacts with the boundary atoms, including a continuation of the crystal, adsorbed atoms, or atoms from an opposing surface. The goal of the Green's function formulation is to absorb the linear response of the substrate atoms into an effective interaction between boundary atoms. This reduces the total number of degrees of freedom

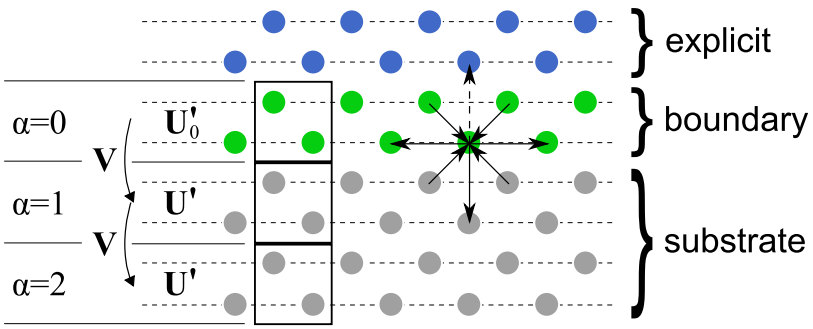

Figure 3.1: Side view of a face-centered cubic (fcc) crystal with a (100) surface showing the layer structure for second-nearest neighbor interactions. The top atoms are treated explicitly. In this case they represent a continuation of the crystal. The boundary layer ($\alpha = 0$) is thick enough to prevent direct interactions between explicit and substrate atoms. The effect on boundary atoms from the elastic response of substrate atoms is captured using the Green's function. The force-constant matrix $\mathbf{D}$ has diagonal components $\mathbf{U'_0}$ and $\mathbf{U'}$ within the layers and off-diagonal components $\mathbf{V}$ coupling adjacent layers. Layers are labeled by the index α and unit cells in each layer (square boxes) by the index i. Arrows show the atoms that produce a force on one atom in the boundary layer. Only the atoms in the boundary and substrate (solid arrows) contribute to the net elastic force $\vec{f}_{i0}$. As a result, there is a net force that would be balanced by the force from explicit atoms (dashed arrows) if the explicit atoms continued the fcc crystal.

to those of the boundary and explicit atoms.

The width of the boundary region must be greater than the range of interactions so that there are no direct interactions between explicit and substrate atoms. The boundary layer is constructed so it satisfies this condition and contains an integer number of primitive unit cells along its width. The substrate is then divided into layers of the same width, so that all atoms are accounted for and each layer only interacts with adjacent layers. In the following, Greek indices α, β, ... identify layers, with the boundary layer at $\alpha = 0$ (see Fig. 3.1). Latin indices i, j, ... will number unit cells within each of these layers.

The total potential energy is divided into terms that involve interactions between explicit atoms, $E_{\rm ee}$, between explicit and boundary atoms, $E_{\rm eb}$, and between boundary and

substrate or boundary atoms, $E_{\rm bs}$:

$$E_{\rm tot} = E_{\rm ee} + E_{\rm eb} + E_{\rm bs} \ . \tag{3.1}$$

The first two terms are treated exactly, while $E_{\rm bs}$ is treated in the usual harmonic approximation.[66,87] The energy $E_{\rm bs}$ is expanded in terms of displacements about a reference configuration. This is usually the ground state, but could be a crystal under a uniform strain that most closely approximates the loaded crystal. For example, under high contact pressures, there will be a mean compressive strain that extends throughout the substrate.

We will denote the set of displacements from equilibrium for the n_c atoms in unit cell i in layer α by the $3n_c$ dimensional vector $\vec{u}_{i\alpha}$. The harmonic approximation for $E_{\rm bs}$ can then be written as:

$$E_{\rm bs} = E_0 - \sum_{i\alpha} \vec{f}_{i\alpha} \cdot \vec{u}_{i\alpha} + \frac{1}{2} \sum_{i\alpha j\beta} \vec{u}_{i\alpha} \mathbf{D}_{i\alpha j\beta} \vec{u}_{j\alpha} + \mathcal{O}(u^3), \tag{3.2}$$

where E_0 is the energy of the reference state, $\vec{f}_{i\alpha}$ is a $3n_c$ dimensional vector giving the force on atoms in the $i\alpha$ unit cell, and $\mathbf{D}_{i\alpha j\beta}$ is the $3n_c \times 3n_c$ force-constant matrix:

$$\mathbf{D}_{i\alpha j\beta} \equiv \left. \frac{\partial^2 E_{\rm bs}}{\partial \vec{u}_{i\alpha} \partial \vec{u}_{j\beta}} \right|_{\vec{u}_{i\alpha}=0, \vec{u}_{j\beta}=0} \ . \tag{3.3}$$

Since we expand about a static solution, the total force

$$\vec{f}_{i\alpha} \equiv - \left. \frac{\partial E_{\rm bs}}{\partial \vec{u}_{i\alpha}} \right|_{\vec{u}_{i\alpha}=0} \tag{3.4}$$

must vanish for all substrate atoms ($\alpha > 0$). For boundary atoms, $\vec{f}_{i0}$ is generally not zero because it only includes the boundary and substrate interactions. These are indicated by solid arrows in Fig. 3.1, and the forces coming from explicit atoms are indicated by dashed arrows. In this figure, the explicit atoms continue the ideal crystal and exert a force that is equal and opposite $\vec{f}^{\,\rm exp}_{i0} = -\vec{f}_{i0}$. If the crystal is terminated at the boundary layer, the

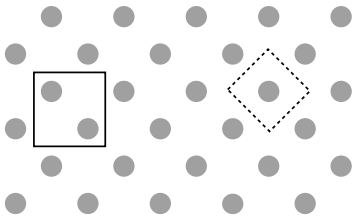

Figure 3.2: Similar to Fig. 3.1, but top view of atoms at top of boundary layer. Periodicity in this plane is used to decouple the response at different wavevectors in the first Brillouin zone of the crystal. The solid and dashed lines show the conventional and primitive unit cells for the surface.

unbalanced forces give rise to the well-known phenomena of surface relaxation.[88] Previous applications of Green's functions to contact mechanics[19] did not include $\vec{f}_{i0}$. However they generally focused on nearest-neighbor interactions and crystals at zero pressure. For this very special case $\vec{f}_{i0}$ vanishes and there is no surface relaxation. In almost all other cases the forces must be included.

The dynamical equation for the boundary and substrate atoms can now be written as:

$$\mathbf{m}\frac{\partial^2 \vec{u}_{i\alpha}}{\partial t^2} + \sum_{j\beta} \mathbf{D}_{i\alpha j\beta}\vec{u}_{j\beta} = \delta_{0\alpha}(\vec{f}_{i0} + \vec{f}^{\,\mathrm{exp}}_{i0}) \tag{3.5}$$

where $\mathbf{m}$ is a diagonal matrix whose elements equal the mass associated with each degree of freedom in the unit cell, the forces are only nonzero for the boundary layer, and $\vec{f}^{\,\mathrm{exp}}_{i0}$ is the force from explicit atoms. Note that even if explicit crystalline atoms are present on top of the boundary layer, the forces $\vec{f}_{i\alpha}$ and $f^{\mathrm{exp}}_{i\alpha}$ do not vanish individually and hence we need to consider both explicitly.

The dynamical equation is simplified by transforming into reciprocal space within the plane of the layers and remaining in real space in the perpendicular direction. Because the crystal retains translational symmetry within the plane (Fig. 3.2), the equations for each two-dimensional wavevector $\vec{q}$ in the first Brillouin zone (BZ) are decoupled. We denote the

set of two dimensional lattice vectors that connect the unit cells within the boundary layer by $\vec{R}_{i0}$. The unit cells in all other layers are then located at $\vec{R}_{i\alpha} = \vec{R}_{i0} + \alpha\vec{c}$ where $\vec{c}$ is the basis vector connecting unit cells in adjacent layers. The Fourier transforms in space and time are defined as:

$$\vec{u}_\alpha(\vec{q},\omega) = \sum_j \int_{-\infty}^{\infty} dt \vec{u}_{j\alpha}(t) e^{-i\vec{q}\cdot\vec{R}_{j0}+i\omega t}, \tag{3.6}$$

$$\vec{u}_{j\alpha}(t) = \int_{\mathrm{BZ}} \frac{d^2q}{A_{\mathrm{BZ}}} \int_{-\infty}^{\infty} \frac{d\omega}{2\pi} \vec{u}_\alpha(\vec{q},\omega) e^{i\vec{q}\cdot\vec{R}_{j0}-i\omega t}, \tag{3.7}$$

where the sum in the first equation is over all unit cells in the boundary layer. The integral in the second equation runs over all wavevectors in the two-dimensional first BZ of the surface and $A_{\mathrm{BZ}} = \int_{\mathrm{BZ}} d^2q$ is the BZ area.

Translational symmetry in the substrate guarantees that $\mathbf{D}_{i\alpha j\beta}$ only depends on relative positions $R_{i0} - R_{j0}$ and $\beta - \alpha$. The Fourier transform is:

$$\mathbf{D}_{\beta-\alpha}(\vec{q}) = \sum_k \mathbf{D}_{j\alpha k\beta} e^{-i\vec{q}\cdot(\vec{R}_{j0}-\vec{R}_{k0})}, \tag{3.8}$$

and must vanish for $|\beta - \alpha| > 1$ because interactions do not extend beyond adjacent layers. The convolution theorem can be used to write the Fourier transform of the dynamical equation (Eq. (3.5)) as:

$$\sum_\beta \left(-\mathbf{m}\omega^2\delta_{\alpha\beta} + \mathbf{D}_{\alpha\beta}(\vec{q})\right) \vec{u}_\beta(\vec{q},\omega) = \delta_{\alpha 0}\vec{f}_{\mathrm{tot}}(\vec{q},\omega) \tag{3.9}$$

where $\vec{f}_{\mathrm{tot}}$ includes both internal and explicit forces and only acts on the boundary layer.

In the following we assume that the substrate terminates at layer $\alpha = N$. Within the substrate, $\mathbf{D}$ only depends on $\beta-\alpha$ and only couples adjacent layers. Let $\mathbf{U}'(\vec{q}) = \mathbf{D}_{\alpha\alpha}(\vec{q})$ be the force-constant matrix that couples within each layer and $\mathbf{V}_\alpha(\vec{q}) = \mathbf{D}_{\alpha(\alpha+1)}(\vec{q})$ the matrix coupling to the nearest layer beneath. Then $\mathbf{V}_\alpha^\dagger(\vec{q})$ is the matrix coupling to the

nearest layer above (see Fig. 3.1), where † denotes the Hermitian conjugate. The force-constant matrix has a tridiagonal form that facilitates solution:

$$\mathbf{D} = \begin{pmatrix} \mathbf{U}_0' & \mathbf{V} & 0 & \cdots & 0 & 0 \\ \mathbf{V}^\dagger & \mathbf{U}' & \mathbf{V} & \cdots & 0 & 0 \\ 0 & \mathbf{V}^\dagger & \mathbf{U}' & \cdots & 0 & 0 \\ \vdots & \vdots & \vdots & \ddots & \vdots & \vdots \\ 0 & 0 & 0 & \cdots & \mathbf{U}' & \mathbf{V} \\ 0 & 0 & 0 & \cdots & \mathbf{V}^\dagger & \mathbf{U}_N' \end{pmatrix} . \tag{3.10}$$

As discussed below, the diagonal term for the final layer, $\mathbf{U}_N'$, depends on the boundary conditions imposed on the bottom of the substrate. The term $\mathbf{U}_0'$ differs from $\mathbf{U}'$ because the diagonal elements of $\mathbf{D}_{i\alpha i\alpha}$ include terms from nearest neighbors in all layers. This can easily be seen by considering the case of a pair potential coupling two atoms, $\phi(\vec{r}_i - \vec{r}_j)$. The second derivative of this part of the total energy will contain terms diagonal in i. Since the top layer has fewer neighbors included in the harmonic approximation, the diagonal terms will be reduced. Specific examples are provided in the Appendix of Ref. 51.

The displacements throughout the substrate are linear functions of the forces applied to the boundary layer:

$$\vec{u}_\beta(\vec{q},\omega) = \mathbf{G}_{\beta 0}\vec{f}_{\rm tot}(\vec{q},\omega) \tag{3.11}$$

Here the Green's function $\mathbf{G}$ satisfies the equation

$$\sum_\beta \left(-\mathbf{m}\omega^2\delta_{\alpha,\beta} + \mathbf{D}_{\alpha\beta}(\vec{q})\right)\mathbf{G}_{\beta\gamma}(\vec{q},\omega) = \delta_{\alpha\gamma}\mathbf{I} \tag{3.12}$$

where $\mathbf{I}$ is a $3n_c \times 3n_c$ identity matrix.

We only need to calculate $\mathbf{G}_{00}$, since $E_{\rm eb}$ only involves displacements of the boundary layer. It is convenient to express everything in terms of these displacements, which can

then be used to calculate the forces from explicit atoms as well as the substrate force. Defining the surface stiffness matrix $\mathbf{\Phi} = \mathbf{G}_{00}^{-1}$ we have

$$\vec{f}_{\rm tot}(\vec{q},\omega) = \mathbf{\Phi}(\vec{q},\omega)\vec{u}_0(\vec{q},\omega). \tag{3.13}$$

Equation (3.13) resembles Hooke's law, and the coefficients $\mathbf{\Phi}$ can be regarded as renormalized spring constants that govern the response of the elastic half space.[19] Note that even though the atomistic interaction within the bulk may be short ranged, the real space coefficients $\mathbf{\Phi}$ typically couple the surface over all length scales.

3.3 Extension to many-body potentials

Applying the GFMD framework to specific potentials is described next. Many-body potentials require particular attention, and we first take the opportunity to distill the essential objectives.

Part of the Hamiltonian of the all-atom system is to be approximated, and the approximated part of the Hamiltonian corresponds to one spatial region of the all-atom system. We will refer to the approximated region as an atomic substrate. At the boundary of the substrate, a subset of atoms is chosen as the GF layer that will separate the substrate from the explicitly-simulated region. The GF layer must be thick enough to prevent direct interactions between the two domains on either side as clarified next. In the remained of Sec. 3.3, Latin indices directly number atoms in the system.

3.3.1 GF layer separates the substrate and explicit regions

A sufficiently large region of atoms must be chosen as the GF layer so that substrate atoms and explicit atoms never interact directly. That is, for a substrate atom i and an explicit atom k, the derivative of the system energy with respect to the atoms' positions (the dynamical matrix D_{ik}) must remain zero. For typical local interactions, each term of the potential energy depends only on a subset of the atomic positions within a limited

region that fits in a sphere of finite diameter d_c. This diameter is then the maximum range of interactions. When atoms i and k are separated beyond d_c, then the dynamical matrix D_{ik} is zero. Therefore the GF layer must be thick enough to prevent substrate and explicit atoms from approaching within this range. Next, we illustrate with both pair-potentials and many-body potentials.

The interaction range of pair-potentials was described in Sec. 3.2. In that case the potential energy may be written as

$$E_{pair} = \sum_j \sum_{k=j+1} V(\vec{r}_j, \vec{r}_k) \tag{3.14}$$

where the sum over j includes all atoms in the system and the sum over k includes all atoms with index greater than j. For computations of short-range interactions, $V(r)$ typically goes to zero at separations $r = |\vec{r}_j - \vec{r}_k|$ larger than a cutoff distance, r_{cut}. Thus only pairs in a sphere of diameter $d_c = r_{cut}$ interact.

A many-body example is EAM,[89,90] commonly used to model metallic bonding. In EAM there is an embedded energy term added to a pair potential term.

$$E_{tot} = E_{embedded} + E_{pair} \tag{3.15}$$

The embedded energy term is a many-body term which may be written as

$$E_{embedded} = \sum_j \mathcal{F}(\rho_j), \tag{3.16a}$$

$$\rho_j = \sum_{k \neq j} f(r_{jk}) \tag{3.16b}$$

Heuristically, the embedded energy of an atom j depends on the effective "electron density," ρ_j, at that location contributed by other atoms. The effective "electron cloud" function $f(r)$ typically drops to zero at a cutoff distance r^f_{cut}. That means that the energy term $\mathcal{F}(\rho_j)$, centered at atom j, can depend on atomic positions of atoms up to r^f_{cut} away in any direction.

The interaction range is the diameter of the corresponding sphere $d_c = 2r^f_{cut}$. This can be seen explicitly by calculating the force on an atom i from $E_{embedded}$,

$$\vec{F}_i = -\vec{\nabla}_i E_{embedded} = -\mathcal{F}'(\rho_i) \sum_{k \neq i} f'(r_{ik}) \hat{r}_{ik} - \sum_{j \neq i} \mathcal{F}'(\rho_j) f'(r_{ij}) \hat{r}_{ij} \tag{3.17}$$

We see that if atoms within a distance r^f_{cut} are called neighbors, then the force on a particle i depends on the density at its neighbor, ρ_j, which in turn depends on the positions of *atom j's neighbors*. Most neighbors of atom j are not neighbors of atom i, but they nonetheless affect ρ_j and therefore also the force on atom i. The dynamical matrix D_{ik} (the second derivative of the energy) is zero for atoms i and k separated beyond the interaction range $d_c = 2r^f_{cut}$. This is the thickness shown in the schematic in Fig. 3.3.

3.3.2 Partitioning the Hamiltonian

We separate the Hamiltonian E_{tot} into the part to be approximated, E_{bs}, and the part to be treated exactly, E_{MD}:

$$E_{tot} = E_{bs} + E_{MD} \ . \tag{3.18}$$

Here E_{MD} (respectively, E_{bs}) must include all terms of the energy that involve positions of explicit-region atoms (substrate-region atoms) and no terms involving substrate-region atoms (explicit-region atoms). Any terms involving only GF-layer-atom positions may be assigned to either E_{MD} or E_{bs}. To match the discussion near Eqn. 3.1, we may choose E_{bs} to be all those terms with no dependence on explicit-atom positions.

We illustrate with the example of EAM (Eqn. 3.15). It is useful when describing EAM to distinguish between top and bottom regions of the GF layer. Only those embedded-energy terms centered on the top-region atoms depend on explicit-region atom positions, and the rest of the GF layer may be called the bottom-region. We make use of e, t, b, and s as shorthand for explicit, top, bottom, and substrate as shown in Fig. 3.3. The terms

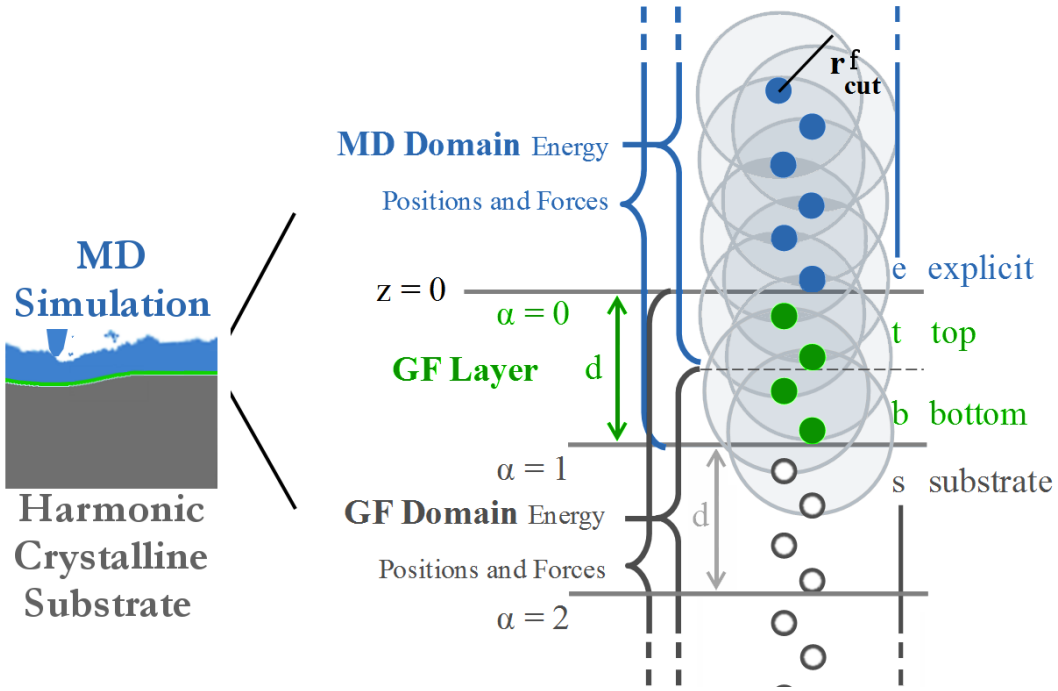

Figure 3.3: The GF layer separates the substrate (s) atoms from the explicit (e) atoms. e atoms are those that retain exact interactions while interactions between s atoms follow a harmonic approximation. s atoms are separated from e atoms by a distance of at least the interaction range, d_c, in the reference configuration. Equivalently, the GF layer must be thick enough so that the derivative of the system energy about the reference configuration with respect to e atom positions is independent of s atom positions. This sets the thickness, d, of the GF layer of atoms. The terms of the energy that are approximated are all those that are independent of explicit atom positions. The case of EAM is illustrated, where grey circles indicate the explicit effective electron density extending a distance r^f_{cut}. The interaction range between atoms is $d_c = 2r^f_{cut}$ which sets a minimum required thickness of the GF layer. Since d_c does not reach 5 atomic planes, d must be at least 4 atomic planes, as shown. For EAM, energy terms centered on the top (t) portion of the GF layer have dependence on explicit atom positions, whereas energy terms centered on the bottom (b) portion do not. In general, atoms throughout the GF layer experience forces due to both $E_{harmonic}$ and E_{MD}. Since the MD software calculates the electron density from e, t, and b atoms, the MD software has the correct electron density at e and t atoms only, as shown.

assigned to the approximated part of the Hamiltonian are

$$E_{bs} = \sum_{j=1}^{N_{tbs}} \sum_{k=j+1}^{N_{tbs}} V(|\vec{r}_j - \vec{r}_k|) + \sum_{j=1}^{N_{bs}} \mathcal{F}_j \tag{3.19}$$

In Eqn. 3.19, the sums in the first term include atoms in the t, b, and s regions, of which there are N_{tbs}. The sum for the embedded energy term occurs only over the N_{bs} atoms in the bottom and substrate region, which are those terms that are independent of explicit-region atom positions.

3.3.3 Linearized dynamics

With the GF layer and E_{bs} thus defined, Eqns. 3.2-3.13, are unchanged for many-body potentials. We nevertheless repeat a few essential points to make explicit some subtleties for many-body potentials.

The GFMD method makes a harmonic approximation for E_{bs}. Given a reference configuration for GF-layer and substrate atoms $\{\vec{r}_i^{\,0}\}$, the displacement of an atom i is defined as $\vec{u}_i = \vec{r}_i - \vec{r}_i^{\,0}$. Taylor expanding E_{bs} to second order about the reference configuration gives for small displacements,

$$E_{bs} \approx E_{harmonic} \equiv E_0 + \sum_{i=1}^{N} \underbrace{\frac{\partial E_{bs}}{\partial \vec{u}_i}}_{-\vec{f}_i} \cdot \vec{u}_i + \frac{1}{2} \sum_{i=1}^{N} \sum_{j=1}^{N} \vec{u}_i^{\,T} \cdot \underbrace{\frac{\partial^2 E_{bs}}{\partial \vec{u}_i \partial \vec{u}_j}}_{D_{ij}} \cdot \vec{u}_j \tag{3.20}$$

Note that the sums occur over all N_{tbs} particles that affect the to-be-approximated energy E_{bs}. The reference configuration does not need to include e atoms, since E_{bs} is independent of those positions.

As pointed out before, the system retains a Hamiltonian, $H = E_{harmonic} + E_{MD}$, thereby avoiding ghost forces. Defining $\vec{f}_i$ and D_{ij} as indicated, the equations of motion for

an atom i are

$$m_i\ddot{\vec{u}}_i - \vec{f}_i + \sum_j D_{ij}\vec{u}_j = -\frac{\partial}{\partial \vec{u}_i}E_{MD} \equiv \vec{f}_i^{MD} \quad . \tag{3.21}$$

where the right hand side of the equation is the force from the explicit atoms and is only nonzero for atoms in the GF layer. Eq. 3.21 represents a large system of coupled, linear equations for atoms in the substrate and GF layer which are to be solved for the displacements of GF layer atoms.

As indicated in Sec. 3.2, if the surface Green's function solution can be found, then integrating against the applied forces $\vec{f}_i^{MD}$ immediately produces the corresponding displacements $\vec{u}_i$ of the GF layer atoms. For crystalline systems, the integration is a convolution which can be accomplished quickly as a multiplication in Fourier space. Efficient methods of determining the Green's function of crystalline systems from the stiffness matrices will be described in Sec. 3.4.

We lastly point out that more stiffness matrices are required for many-body potentials than for pair-potentials. Notationally, D_{ij} is called V_{ij} when atom j is one layer below i, or U_{ij} when i and j are in the same layer. Recall that, for efficient calculation of the GF, each substrate layer is thick enough so that (in the reference configuration) interactions do not occur with atoms beyond the nearest layer. But when referring to specific lattices, it can be useful to sub-divide the GF layer into thinner layers, called sub-layers. Then we can refer to the stiffness D of interactions 0, 1, or 2 sub-layers apart as $\tilde{U}$, $\tilde{V}$, or $\tilde{W}$.

For pair-potentials, the value of D_{ij} is determined usually just by the relative positions of atoms i and j, so many stiffness matrices are the same. For many-body potentials, the stiffness D_{ij} can change with distance to the free surface, since E_{bs} usually contains fewer terms for atoms closer to the surface, as illustrated in Fig. 3.4. D connecting two atoms in the uppermost sub-layer can be denoted $\tilde{U}_0$, where the subscript denotes the sublayer of the atom closest to the surface. If instead the two atoms are in the second

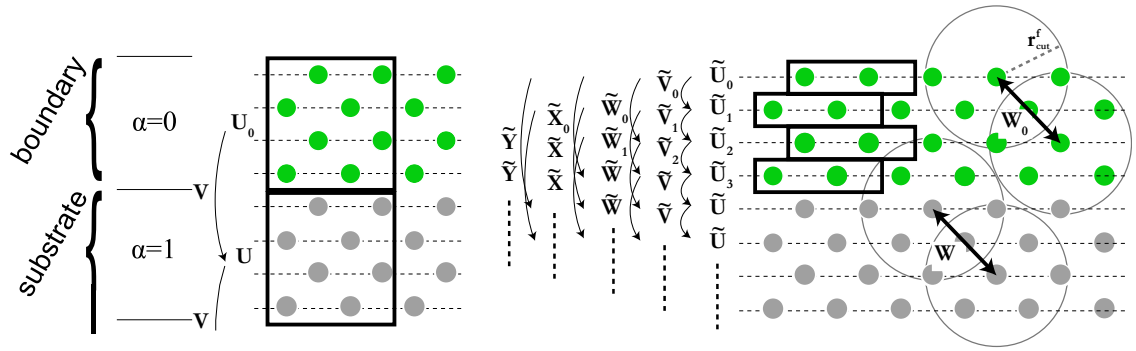

Figure 3.4: The interaction range d_c is usually long for many-body potentials, and so the stiffness matrix between many pairs of atoms is needed. Also, the stiffness matrix is associated only with the approximated part of the energy, and so the stiffness matrix contains fewer terms for top atoms in the GF layer whose many-body terms are not included in E_{bs}. Fig 3.4 shows the same example system as Fig. 3.3. Unlike in the pair-potential case, the stiffness $\tilde{W}_0$ are $\tilde{W}$ are different. This is because terms that depend on GF-layer atoms are also associated with explicit atoms which are missing from E_{bs}.

uppermost sub-layer, then $\tilde{U}_1$ is used. If atoms i and j are in the first and second sublayer respectively, the notation is $\tilde{V}_0$. For the EAM example shown in Fig. 3.3 and 3.4, there is a single-atom thickness for each sub-layer and r^f_{cut} is between a second and third sub-layer of atoms, requiring fifteen stiffness matrices.

3.4 Finding the Green's function from the dynamical matrix

One can evaluate the Green's function using a transfer matrix formulation. This approach has been previously applied to the analysis of the electronic[83] and phononic[84] structure of surfaces, and more generally to the statistical mechanics of systems with only short ranged interactions, like the Ising model.[91–93] Our derivation is most similar in form to that of Velasco and Ynduráin.[84] Unlike the force-constant matrix, the Green's function is not

sparse. We denote the individual elements by

$$\mathbf{G} = \begin{pmatrix} \mathbf{G}_{00} & \mathbf{G}_{01} & \mathbf{G}_{02} & \cdots & \mathbf{G}_{0N} \\ \mathbf{G}_{10} & \mathbf{G}_{11} & \mathbf{G}_{12} & \cdots & \mathbf{G}_{1N} \\ \mathbf{G}_{20} & \mathbf{G}_{21} & \mathbf{G}_{22} & \cdots & \mathbf{G}_{2N} \\ \vdots & \vdots & \vdots & \ddots & \vdots \\ \mathbf{G}_{N0} & \mathbf{G}_{N1} & \mathbf{G}_{N2} & \cdots & \mathbf{G}_{NN} \end{pmatrix}, \tag{3.22}$$

where we will drop the explicit reference to $\vec{q}$ and ω below.

From Eq. (3.12) we obtain generally $(N+1)^2$ equations for our finite system with $N+1$ layers. We only pick the $N+1$ equations involving the surface layer. These are

$$\mathbf{U}_0\mathbf{G}_{00} + \mathbf{V}\mathbf{G}_{10} = \mathbf{I} \tag{3.23}$$

$$\mathbf{V}^\dagger\mathbf{G}_{00} + \mathbf{U}\mathbf{G}_{10} + \mathbf{V}\mathbf{G}_{20} = \mathbf{0}$$

$$\mathbf{V}^\dagger\mathbf{G}_{10} + \mathbf{U}\mathbf{G}_{20} + \mathbf{V}\mathbf{G}_{30} = \mathbf{0}$$

$$\vdots$$

$$\mathbf{V}^\dagger\mathbf{G}_{n-1,0} + \mathbf{U}\mathbf{G}_{n,0} + \mathbf{V}\mathbf{G}_{n+1,0} = \mathbf{0} \tag{3.24}$$

$$\vdots$$

$$\mathbf{V}^\dagger\mathbf{G}_{N-1,0} + \mathbf{U}_N\mathbf{G}_{N,0} = \mathbf{0} \tag{3.25}$$

where $\mathbf{U} = \mathbf{U}' - \mathbf{m}\omega^2$. It is also straightforward to include wavevector dependent damping by adding a term of the form $i\omega\Gamma(\vec{q})$ in addition to the mass term.

Given the structure of these equations it is useful to define the transfer matrix $\mathbf{T}_n$ as

$$\mathbf{G}_{n+1,0} = \mathbf{T}_n\mathbf{G}_{n,0}. \tag{3.26}$$

The surface Green's function $\mathbf{G}_{00}$ and stiffness $\mathbf{\Phi}$ are then obtained from Eq. (3.23) as

$$\mathbf{\Phi} = \mathbf{G}_{00}^{-1} = \mathbf{U}_0 + \mathbf{V}\mathbf{T}_0. \tag{3.27}$$

Combining Eqs. (3.24), (3.25) and (3.26) yields

$$\mathbf{V}\mathbf{T}_n\mathbf{T}_{n-1} + \mathbf{U}\mathbf{T}_{n-1} + \mathbf{V}^\dagger = 0 \tag{3.28}$$

and

$$\mathbf{U}_N\mathbf{T}_{N-1} + \mathbf{V}^\dagger = 0. \tag{3.29}$$

For physically relevant solutions the displacements produced by static surface forces (i.e. at $\omega = 0$) must decrease or remain constant with increasing depth. This implies that the eigenvalues of $\mathbf{T}_n$ have magnitude between 0 and 1. If the eigenvalues are less than one, the deformation decays exponentially with distance from the surface and the result is insensitive to the depth of the system. The analytic solution to the continuum Green's function for a semi-infinite plane[20] gives an exponential decay with length of order $1/|\vec{q}|$ and we find that the lattice Green's function is consistent with this scaling for small $|\vec{q}|d_{\text{nn}}$ where d_{nn} is the nearest neighbor spacing. As a result, the surface stiffness matrix is sensitive to boundary conditions for small wavevectors: $|\vec{q}| \sim 1/Nd_{\text{nn}}$.

One interesting case is that of free boundary conditions. In this case, one allowed solution is uniform translation of the entire system, i.e. $\mathbf{T} = \mathbf{I}$ for $\vec{q} = 0$. Translational invariance requires that no force is produced by a uniform translation of the crystal and this imposes an acoustic sum rule on the components of $\mathbf{D}$.[66,87] It is straightforward to show that Eq. (3.28) is consistent with this sum rule for $\mathbf{T}_n = \mathbf{I}$. The surface stiffness matrix for uniform translation of all atoms vanishes for this case because from Eq. (3.27) we get $\mathbf{\Phi}(\mathbf{\Gamma}) = \mathbf{U}_0(\mathbf{\Gamma}) + \mathbf{V}(\mathbf{\Gamma})$ which is precisely the acoustic sum rule at the surface.

To maintain a finite stiffness, one normally considers systems with a rigid boundary

condition applied at the bottom of the substrate. This corresponds to $\mathbf{U}_N = \mathbf{U}$. In essence, this equality implies that there is a contribution from neighbors below layer N but that their displacement is set to zero. The acoustic sum rule is violated because these neighbors impose a frame of reference. For the rigid boundary condition we expect a constant, uniform force will produce a constant uniform strain. Then $\mathbf{T}_0 \approx \mathbf{I}(1-1/N)$ and the surface stiffness $\mathbf{\Phi}(\mathbf{\Gamma})$ is finite, but goes to zero as $1/N$ with increasing system depth N.

The fact that the termination at layer N is important for small $\vec{q}$ means that we can not in general assume that $\mathbf{T}_n$ is independent of n. We solve the equations using a continued fraction approach based on the relation

$$\mathbf{V}\mathbf{T}_{n-1} = -\mathbf{V}(\mathbf{U} + \mathbf{V}\mathbf{T}_n)^{-1}\mathbf{V}^\dagger. \tag{3.30}$$

The continued fraction has the form:

$$\mathbf{\Phi} = \mathbf{U}_0 - \mathbf{V}\cfrac{1}{\mathbf{U} - \mathbf{V}\cfrac{1}{\mathbf{U} - \mathbf{V}\cfrac{1}{\mathbf{U} - \mathbf{V}\cfrac{1}{\mathbf{U} - \ldots}\mathbf{V}^\dagger}\mathbf{V}^\dagger}\mathbf{V}^\dagger}\mathbf{V}^\dagger \tag{3.31}$$

For large q the bottom boundary is unimportant and the continued fraction converges after a few iterations. For small q, the continued fraction is terminated after N terms using Eq. (3.29). In the examples below we focus on static solutions $\omega = 0$. For dynamic solutions a small imaginary part is added to the frequency to obtain the retarded Green's function.[94]

The above method of finding $\mathbf{\Phi}$ takes time of order N for small q. Since the Green's function can be precomputed, this does not represent a significant computational barrier. However there is an alternative approach based on decimation that is only of order $\log N$. Related approaches have been used for real-space renormalization calculations of electronic

structure.[85,86]

Equations (3.23) to (3.25) only couple nearest neighbor elements of $\mathbf{G}$. The equations for odd n can be used to express $\mathbf{G}_{2n+1,0}$ in terms of $\mathbf{G}_{2n+2,0}$ and $\mathbf{G}_{2n,0}$. Substituting the result into the equations for even n, one obtains equations of the same form as Eqs. (3.23) to (3.25), but with renormalized $\mathbf{U}^{(2)}$ and $\mathbf{V}^{(2)}$:

$$\mathbf{U}_0^{(2)}\mathbf{G}_{00} + \mathbf{V}^{(2)}\mathbf{G}_{20} = \mathbf{I} \tag{3.32}$$

$$(\mathbf{V}^{(2)})^\dagger\mathbf{G}_{2n-2,0} + \mathbf{U}^{(2)}\mathbf{G}_{2n,0} + \mathbf{V}^{(2)}\mathbf{G}_{2n+2,0} = \mathbf{0} \tag{3.33}$$

$$(\mathbf{V}^{(2)})^\dagger\mathbf{G}_{N-2,0} + \mathbf{U}_N^{(2)}\mathbf{G}_{N,0} = \mathbf{0}. \tag{3.34}$$

The procedure can then be repeated with the renormalized equations. The general recursion expressions for the renormalized matrices at iteration m are:

$$\mathbf{U}^{(m+1)} = \mathbf{U}^{(m)} - (\mathbf{V}^\dagger\mathbf{U}^{-1}\mathbf{V})^{(m)} - (\mathbf{V}\mathbf{U}^{-1}\mathbf{V}^\dagger)^{(m)} \tag{3.35}$$

$$\mathbf{V}^{(m+1)} = -(\mathbf{V}\mathbf{U}^{-1}\mathbf{V})^{(m)} \tag{3.36}$$

$$\mathbf{U}_0^{(m+1)} = \mathbf{U}_0^{(m)} - (\mathbf{V}\mathbf{U}^{-1}\mathbf{V}^\dagger)^{(m)} \tag{3.37}$$

$$\mathbf{U}_N^{(m+1)} = \mathbf{U}_N^{(m)} - (\mathbf{V}^\dagger\mathbf{U}^{-1}\mathbf{V})^{(m)} \quad . \tag{3.38}$$

The greatest efficiency is achieved when $N = 2^M$. The equations are then iterated M times to produce two linear equations containing only $\mathbf{G}_{00}$ and $\mathbf{G}_{N0}$:

$$\mathbf{U}_0^{(M)}\mathbf{G}_{00} + \mathbf{V}^{(M)}\mathbf{G}_{N0} = \mathbf{I} \tag{3.39}$$

$$(\mathbf{V}^{(M)})^\dagger\mathbf{G}_{00} + \mathbf{U}_N^{(M)}\mathbf{G}_{N0} = \mathbf{0}. \tag{3.40}$$

This yields

$$\mathbf{\Phi} = \mathbf{U}_0^{(M)} - \mathbf{V}^{(M)}(\mathbf{U}_N^{(M)})^{-1}(\mathbf{V}^{(M)})^\dagger \tag{3.41}$$

For large wavevectors, the renormalized $\mathbf{V}^{(m)}$ goes rapidly to zero as m increases and $\mathbf{U}_0^{(m)}$

goes to a constant.[85] The surface stiffness matrix $\mathbf{\Phi}$ is equal to the renormalized $\mathbf{U}_0^{(m)}$. We numerically checked that transfer matrix and renormalization group calculations give identical results.

3.5 Natural implementation in MD

The GFMD method calculates the forces based on the Hamiltonian

$$E_{MD}(\{\vec{r}\}) + E_{harmonic}(\{\vec{r}\}). \tag{3.42}$$

The energy and forces associated with E_{MD} are calculated by the MD software, while the energy and forces of $E_{harmonic}$ are calculated by the GF software. The natural way to implement the scheme is described next.

Rather than load the entire atomic geometry into the MD software, only atoms of the explicit region and GF layer are loaded. The idea is that the MD software performs mostly its normal operation on this smaller system, and the GF software is responsible for adding forces on the GF layer to reach the full Hamiltonian. The substrate atoms need not be followed in the software at all because their effect is captured by the Green's function. The following will describe the details of this division of the software operation for the example of the EAM potential.

GF-layer atoms are subject to forces from both parts of the Hamiltonian, E_{MD} and $E_{harmonic}$. For the EAM potential, the force on an atom i is

$$\begin{aligned}\vec{F}_i &= -\vec{\nabla}_i(E_{MD} + E_{harmonic}) \\ &= \underbrace{-\vec{\nabla}_i \sum_{j\in e} \sum_{k=j+1} V(\vec{r}_j, \vec{r}_k) - \vec{\nabla}_i \sum_{j\in e,t} \mathcal{F}(\rho_j)}_{\text{MD software}} + \underbrace{\vec{f}_i - \sum_{j\in s,b,t} D_{ij}\cdot\vec{u}_j}_{\text{GF software}}\end{aligned} \tag{3.43}$$

It is the responsibility of the MD software to calculate the terms associated with E_{MD}, as normal. The restriction on the pair potential sum ($j \in e$) means that only pair-interactions

involving an explicit atom are included. The embedded energy term (the sum of $\mathcal{F}(\rho_j)$ with the restriction $j \in e, t$) requires the system's "electron density" ρ at e and t atoms only. This is available to the MD software because e, t, and b atoms are loaded in the MD software as shown in Fig. 3.3. However, the MD software would normally include all loaded atoms, including b atoms, in the embedded energy sum. So the MD software must be modified to exclude the many-body terms centered on b atoms from the embedded energy sum. In summary, the MD software produces the forces due to E_{MD}.

The GF software calculates the third and fourth terms of Eqn. 3.43, associated with $E_{harmonic}$. Again, the restrictions on the sum come from the fact that $E_{harmonic}$ is an expansion in all atomic displacements of $E_{bs} = \sum_{i \in s,b} \mathcal{F}(\rho_j)$. This term is the force on atom i given displacements of atoms indexed with j. It is calculated immediately from Eq. 3.13.

3.6 Stringent testing method

Conceptually, each GFMD simulation refers to an underlying full-MD system. A stringent test of the code involves comparing a simulated GFMD system with its full-MD counterpart. This confirms that no terms were neglected in the derivation and that the code was implemented correctly.

We use both GFMD and all-atom MD to simulate a crystal. An example system used for testing is shown in Fig. 3.5. We choose M atoms of the crystal which are in the GF layer in the GFMD system. These are called probe atoms. We prescribe displacements to each probe atom, in different directions and of different magnitudes, and the $3M$-element displacement vector is called $\vec{u}$. Then we minimize the system energy while holding the probe atoms fixed. The system relaxes so that there is zero force on all but the fixed atoms. The $3M$-element force vector may be called $\vec{f}$, and the total system energy is E.

If $|\vec{u}|$ is very small, the system response is linear. That is, expansion Eqn. 3.20 is a good approximation, since probe atom displacements are small and other atom dis-

placements are linear in the probe atom displacements. We then vary the magnitude of the vector $\vec{u}$ to ensure that the two systems show the same linear response.

The GFMD system energy $E_{harmonic} + E_{MD}$ should match the all-atom energy E_{tot} to harmonic order in the applied atomic displacements (Eqn. 3.20). The upper plots of Fig. 3.6 show that, as expected, the error in the energy falls as $|\vec{u}|^3$. The bottom plots of Fig. 3.6 show that the error in the forces is correspondingly quadratic in the displacements. All data shows a linear error of below 10^{-7}, corresponding approximately to floating point rounding.

Note the sensitivity of the test: even a 0.01% error in the value of D_{ij} calculated in Eq. 3.21 would add a linear term with magnitude 10^{-4} to the force error. Also, as discussed in Sec. 3.1.1 and Sec. 3.7, surface relaxation causes atomic positions to deviate from the uniform lattice in the uppermost crystal layers. Plots like Fig. 3.6 easily detect small nonlinearities due to surface relaxation forces, and for these tests of the code, the GF layer is chosen to be a few layers below the surface of the crystal (as in Fig. 3.3 and Fig. 3.5). This way all GF atoms initially sit at their reference configuration.

Automated testing using different system sizes and interaction types can be used to confirm correct implementation of the code. The runtimes for all-atom and GFMD calculations are compared in Fig. 3.7. As expected, the CPU time per time step scales as L^3 for all-atom and only as $L^2 lnL$ for GFMD. We commonly use cubic systems with $L = 1000$, where the CPU time is reduced by a factor of 100 for each time step.

3.7 Application to static contact mechanics

To show that the Green's function method provides seamless boundary conditions we present results for three cases. The first is surface relaxation at a flat crystal/vacuum interface, where the unbalanced forces $\vec{f}_{i0}$ are important. The second is Hertzian contact of a rigid sphere and a flat elastic substrate. In the final example the sphere is replaced by a randomly

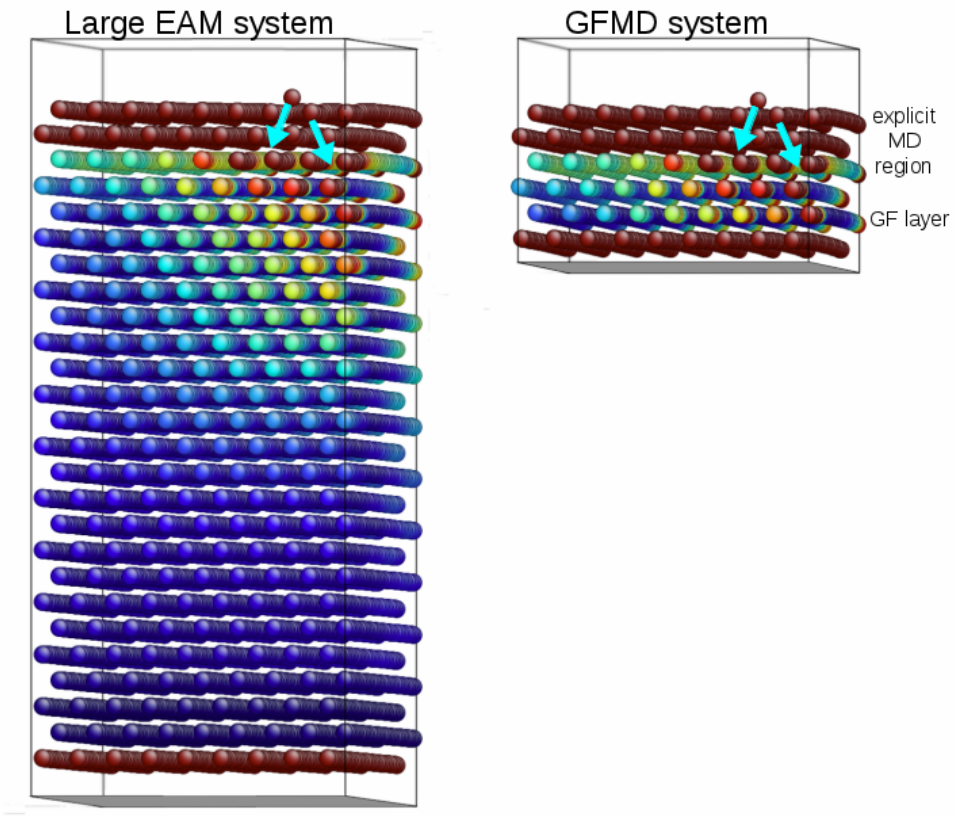

Figure 3.5: An fcc crystal of 13-unit-cell thickness is simulated using both all-atom MD and GFMD. The free surface is (001). The bottom plane of atoms is held fixed in the large EAM system, and this affects the response of the elastic GF layer in the GFMD system. There are periodic boundary conditions in the plane of the surface and interactions are an EAM potential for Au.[95] In the case shown, the GFMD system includes two atomic planes near the surface and an adsorbed atom that are simulated explicitly. To test the code, we prescribe a displacement to arbitrary atoms in both simulations, as indicated by arrows. The same stresses, represented by color, are reproduced by the much smaller GFMD system in much less time.

Figure 3.6: Energy errors (top) and force errors (bottom) made by the harmonic approximation as a function of displacement. Shown are (a) results for the (100) surface on an fcc solid interacting with a Lennard-Jones potential, (b) results for the (100) surface of an fcc solid interacting with an EAM potential, and (c) results for the (111) surface of a crystal in the diamond structure interacting with an Abell-Tersoff-Brenner-type potential.[96] The error in the energy is $\sim |\vec{u}|^3$ and the error in the force is quadratic.

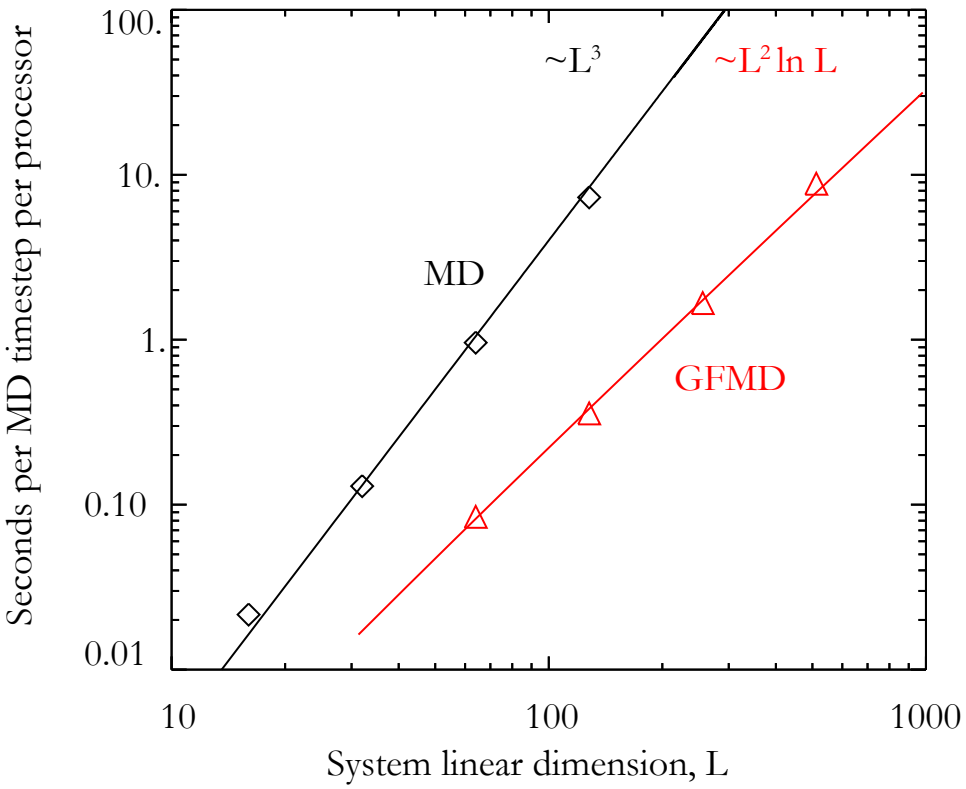

Figure 3.7: Computation time for MD and GFMD scales approximately as L^3 and $L^2 \ln L$ respectively. The acceleration is approximately 100-fold for $L = 1000$. Note that this figure shows wall time *per MD time step*. The number of time steps required to converge is usually much higher for the MD system because there are more degrees of freedom. In the GFMD system, those degrees of freedom of the substrate are slaved to be at a zero-force configuration, and need not even be calculated.

rough surface, which enhances plastic deformation in the crystal.

Results for different crystals and interactions are presented. The simplest is the (100) surface of a face-centered cubic (fcc) crystal with nearest-neighbor harmonic interactions with spring constant k. This system is called nn-fcc below.

The second system, called 2n-fcc, is also the (100) fcc surface but with second-nearest neighbor interactions. Particles interact with a Lennard-Jones potential

$$V(r) = 4\epsilon \left[\left(\frac{\sigma}{r}\right)^{12} - \left(\frac{\sigma}{r}\right)^{6} \right] \tag{3.44}$$

for $r < r_1 = 1.35\sigma$. The potential and force are then smoothly brought to zero at $r_2 = 1.8\sigma$ using a third-order spline.[97] The value of r_2 is chosen so that the potential extends only to second-nearest neighbors in the zero pressure ground state of the fcc structure.

The third case, called sc, is the (100) surface of a simple cubic solid with the same spring constant k between first and second neighbors. This solid has also been used by Campaña and Müser in their work on the contact of rough surfaces.[19,75–77] We checked that the transfer matrix and renormalization formulations give surface stiffness matrix coefficients that are identical to the analytic result of Saito[78] for the sc system.

As a first example, we consider surface relaxation at a flat crystal/vacuum interface. Terminating the crystal generally leads to nonzero internal forces on atoms that lie on the ideal lattice sites. These are described by $\vec{f}_{i0}$ in the Green's function method. One consequence is that the spacing between atomic planes deviates from the bulk value and varies as a function of the depth below the interface. For a flat surface, the forces are the same on all unit cells so we only need to consider the $\vec{q} = 0$ contribution.

Figure 3.8 shows the deviation from the bulk spacing between atomic planes as a function of depth for the 2n-fcc system. Results for 0, 2, 4 and 8 atomic planes of explicit atoms on top of the boundary layer are all equivalent. (Note that there are 2 atomic planes per boundary and substrate layer.) This confirms that the Green's function provides a

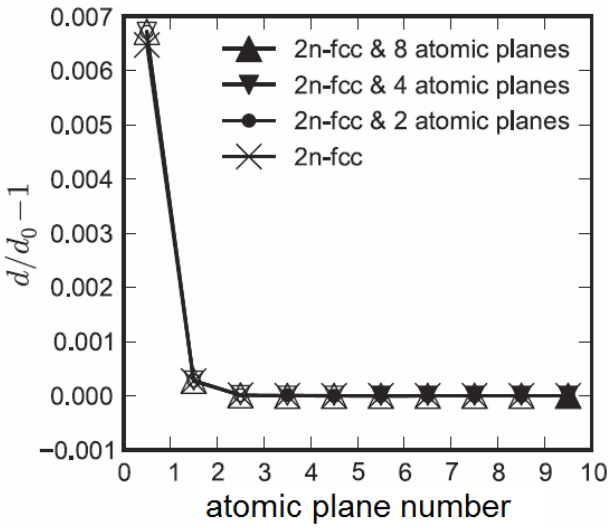

Figure 3.8: Fractional change in spacing of atomic planes d from bulk value d_0 as a function of depth below a free (100) surface of an fcc crystal. Results from the Green's function with 0, 2, 4, and 8 atomic planes (0, 1, 2 and 4 unit cells) are equivalent. The surface layer is 0 and the separation is plotted at the midpoint between layers. Open symbols show the spacing within the explicit crystal and between explicit and substrate layers. Full symbols denote spacing within the substrate.

seamless boundary condition for the explicit region. Note that in some systems surface relaxation leads to a different periodicity of the surface and bulk layers. To capture this relaxation, one must include layers of explicit atoms above the Green's function boundary layer.

The previous Green's function implementation of Campañá et al.[19] did not include $\vec{f}_{i0}$ and thus did not capture surface relaxation. We found that excluding $\vec{f}_{i0}$ had several effects. One was that it led to nonuniform spacing between atomic planes of explicit atoms placed on top of the boundary layer. This variation is effectively a form of surface relaxation due to an effective discontinuity in the forces between surfaces. It also represents a violation of Newton's third law because boundary atoms feel a force from explicit atoms, but the counterforce is missing. When the explicit atoms were from an opposing surface, we found that the change in spacing of atomic planes led to changes in the force on the second layer

that could be important for adhesive contact.

Our second example is Hertzian contact[20] of a rigid spherical indenter with radius R and an elastic substrate with contact modulus E^*. (Note that E^* is called E' elsewhere in the thesis.) Continuum theory[20,98] predicts contact occurs in a circle of contact radius a. Both a and the peak pressure p_0 in the center of the contact rise as the cube root of the normal load N:

$$\frac{a}{R} = \frac{\pi}{2}\frac{p_0}{E^*} = \left(\frac{3N}{4E^*R^2}\right)^{1/3} \tag{3.45}$$

These analytic predictions are compared to different atomistic models in Fig. 3.9.

All atomistic models have substrates with a square array of 256×256 surface atoms and a depth of 256 atomic planes. Different numbers of atomic planes are treated explicitly and the number of atomic planes in the boundary and substrate layers depends on the interaction range. Here and in all following simulations we move the indenter and then relax the positions of the substrate atoms assuming a rigid boundary at the bottom of the substrate. The sphere is featureless and interacts with an atom at position $\vec{r}_i$ via the potential $V_{\text{rigid}}(\vec{r}_i) = V(|\vec{r}_i - \vec{r}_0| - R)$ where $\vec{r}_0$ is the center of the sphere and R its radius. The potential V is the Lennard-Jones potential of Eq. (3.44), but cutoff at its minimum and with ϵ increased by a factor of 100 to approximate a hard-sphere interaction.

The contact modulus E^* is analytically known for the isotropic continuum case, where $E^* = 2\mu(1+\nu)/(1-\nu^2)$, μ is the shear modulus and ν Poisson's number (see the Appendix of Ref. 51). In the results below $\nu = 0$. The 2n-sc substrate is isotropic with $E^* = \frac{8}{3}k/A_a$ where A_a is the surface area occupied by a single atom. The nn-fcc and 2n-fcc cases are anisotropic, and in this case the contact modulus generally depends on orientation and indenter geometry.[99,100] There is no simple analytic relation and we will use Hertz theory to fit effective values of E^*.

Fig. 3.9(a) shows the variation of p_0 with load for all atomistic systems. We first

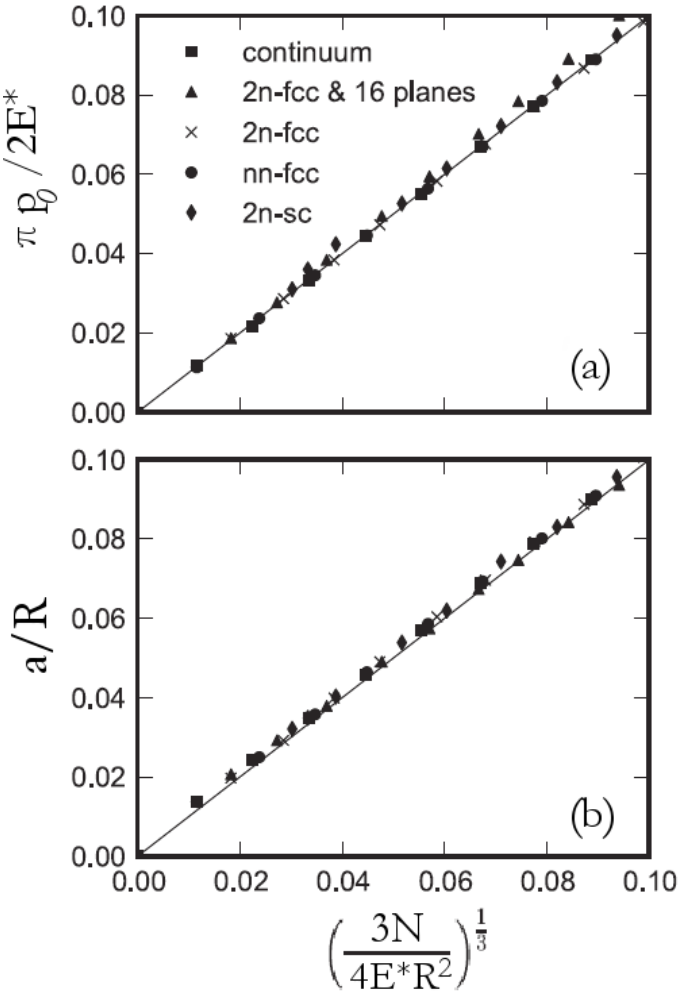

Figure 3.9: Contact of a rigid spherical indenter with radius $R = 100\sigma$ on an elastic substrate. Shown is (a) the peak pressure p_0 and (b) contact radius a as a function of load N normalized by the elastic contact modulus E^*. We compare calculations for (100) surfaces of the fcc lattice with nearest neighbor (nn) and second-nearest neighbor (2n) interactions to calculations of a simple cubic (100) surface and continuum calculations. The effective size of the substrate is a cubic block with 256 atoms in each lateral direction and periodicity parallel to the surface. The values for the effective contact modulus E^* for the anisotropic nn-fcc and 2n-fcc cases are fit to the peak pressure shown in panel (a).

discuss results where the entire substrate is treated with the Green's function method so that the elastic response is linear. Data for each system were divided by the value of E^* that optimizes the fit to the solid line showing the prediction of continuum theory. For the cases where E^* is known, the fit value is within about 2% of the analytical expression. Some deviation is expected from the discrete geometry and finite-compliance interface potential. For the continuum Green's function the fit yields $E^* = 2.02\mu$ compared to the analytic $E^* = 2\mu$. For the 2n-sc solid we obtain $E^* = 2.73k/A_a$ as compared to the analytic $E^* \approx 2.67k/A_a$. For the nn-fcc and 2n-fcc substrate, the fits give $E^* = 1.4k/A_a$ and $E^* = 70.4\epsilon/\sigma^3$, respectively. While we have no prediction to compare to, these numbers are of the order of the relevant elastic moduli.

Fig. 3.9(b) compares the load-radius relationship for different models to continuum theory using the value of E^* obtained from fitting p_0 above. Contact was defined by a repulsive interaction between atoms and indenter. The contact radius was then obtained by equating πa^2 to the number of contacting atoms times the surface area per atom. While a/R rises with the slope predicted by continuum theory, there is an offset corresponding to an increase in contact area. An even larger offset is observed in previous simulations of atomic scale contact.[1,11,101,102] The deviations are minimized in our work by using a featureless indenter and making the interaction closer to a hard wall repulsion by increasing ϵ by two orders of magnitude. The same limit was achieved in Ref. 102 by increasing the density of atoms on the indenter.

The peak strain at the interface is of order a/R and one may expect nonlinear behavior at the largest values of $\sim 10\%$ in Fig. 3.9. The Green's function approach allows this to be studied while only treating a small number of explicit atoms. Fig. 3.9 shows that including 16 layers of explicit atoms does not change the contact area on the scale of the figure, but does increase the peak pressure. The full pressure distribution for different numbers of atomic planes at several loads is shown in Fig. 3.10 for $R = 100\sigma$ and $R =$

1000σ. In all cases, the pure Green's function results follow the analytic solution for elastic substrates (solid line). When explicit atomic planes are included, there are deviations from Hertz theory. The pressure needed to deform the central regions is higher for the explicit solution because Lennard-Jones bonds become stiffer as they are compressed. As expected from Hertz theory, the deviations increase with a/R which sets the peak strain. Increasing R from $100a$ to $1000a$ reduces the deviations at a fixed value of a. Deviations are very small for a/R less than 2%, which is consistent with direct evaluations of anharmonic effects.

Note that the number of layers needed to capture nonlinear effects grows with a/R. A single pair of layers has little effect, while 8 layers is sufficient for a/R up to about 0.09 (Fig. 3.10(a)). All atom simulations are consistent with the 16 layer results for $a/R = 0.12$ and one may expect plastic deformation at larger a/R for most materials. In the Hertz solution, strains decay over scales of order a and the peak shear strain is at a depth of about $a/3$.[20] Including explicit layers to greater depths should allow the system to capture nucleation of defects and other nonlinear effects.

The next test considers the case of contact with a rigid, randomly rough surface, which has been extensively investigated using similar techniques.[19,42,53,75–77] Many experimental surfaces are found to have roughness on all scales that can be described as a self-affine fractal. The root-mean squared (rms) change in height dh over a lateral distance ℓ scales as $dh \propto \ell^H$ where H is called the Hurst or roughness exponent. We generate a self-affine surface with $H = 0.8$ on a 1024×1024 grid using Voss' random midpoint algorithm.[103] This surface is Fourier filtered to remove roughness on all wavelengths below 16 grid spacings. We then use bicubic splines to interpolate the discrete positions to a continuous surface with height $h(x, y)$. The final surface has a root mean square slope of $h'_0 = \sqrt{|\nabla h|^2} = 0.09$.

The rough surface is pushed against a 2n-fcc solid with 256×256 surface atoms and different numbers of explicit layers. Atoms at position $\vec{r} = (x, y, z)$ interact with the

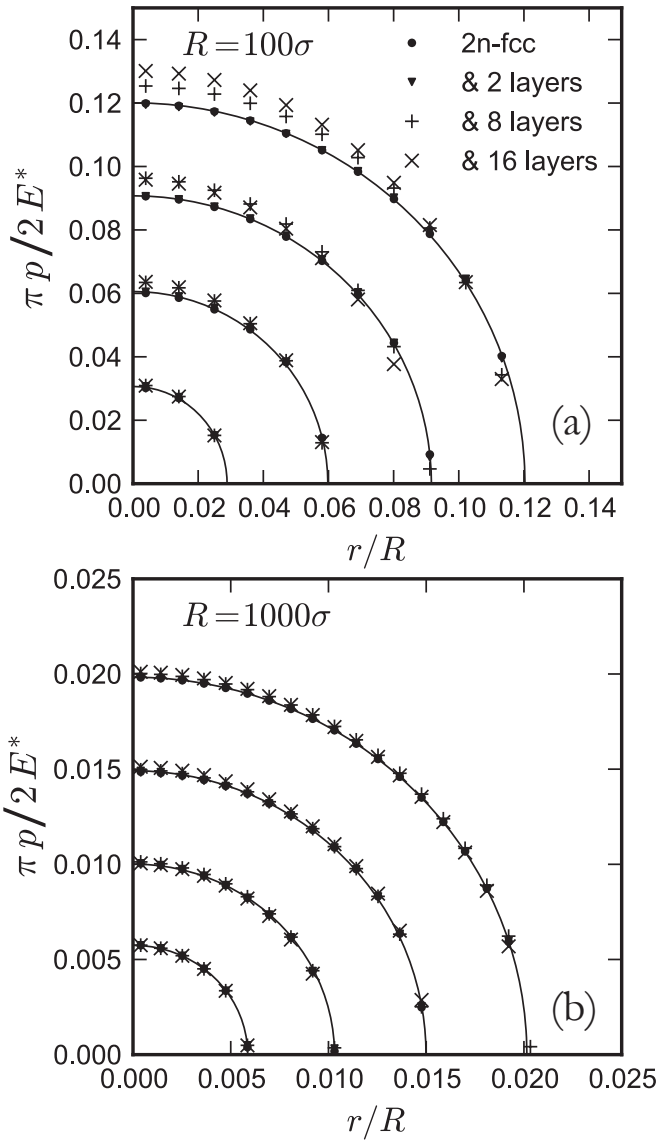

Figure 3.10: Pressure as a function of distance from the tip center along a row of atoms in the (110) direction for rigid spherical indenters with radius (a) $R = 100\sigma$ or (b) $R = 1000\sigma$ on an elastic substrate.

surface via the potential $V_{\text{rigid}}(x, y, z) = V(z - h(x, y))$, where $V(z)$ has the same functional form as the interaction used for the rigid sphere but only depends on the height difference. The area of contact A is determined by multiplying the area per atom by the number of atoms in the top layer of the crystal that feel a repulsion from the rough surface.

Previous numerical and analytic work has found a linear relationship between load and contact area of the form

$$\frac{N}{h_0' E^* A_0} = \frac{1}{\kappa} \frac{A}{A_0} \tag{3.46}$$

with $\kappa \approx 2$.[7,77,104] Fig. 3.11 compares this prediction (solid line) to results for 2n-fcc surfaces with different numbers of layers of explicit atoms. At small loads, results for all numbers of explicit atoms lie close to the solid line. The purely elastic calculation where the entire elastic solid is described by the Green's function follows the solid line all the way to 10% contact area. When two explicit layers are included, the area rises less rapidly as the load increases. This reflects anharmonicity in the explicit layers, where the Lennard-Jones potential stiffens as bond lengths shrink under the applied pressure. Note that results with 4 and 8 explicit layers are nearly indistinguishable, implying that anharmonicity is largely confined to the outer layers. A small number of explicit layers is sufficient in this case because the effective radius a of local contacting regions for this rough surface is only of order 4σ. This allows the Green's function method to reproduce the full nonlinear response of the atomistic system at a small fraction of the computational cost.

The rough surface just considered is artificial because it has no atomic structure. As a final example we consider a rough rigid surface made of discrete atoms on a crystalline lattice. The layered structure leads to steps or terraces that focus stress and lead to dislocation nucleation.

The stepped surface is created from an fcc crystal with a (100) surface and the same lattice spacing as the substrate. A smooth randomly rough surface with rms slope

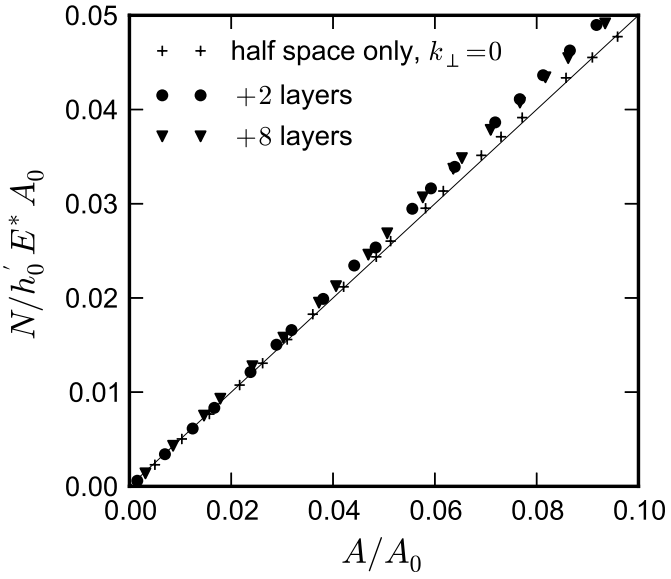

Figure 3.11: Contact of a rigid rough surface on a crystalline fcc (100) surface. The periodicity of the rough surface is 256 nearest neighbor distances d_0 in both directions with a nominal surface area of $A_0 = 256d_0 \times 256d_0$. The solid interacts via a pair potential that extends to second neighbors as described in the text. Shown are the load N normalized by the root mean square slope $h_0' = \sqrt{|\nabla h|^2}$ of the rough surface and the contact modulus E^* as a function of area. The effective size of the substrate is a cubic block with 256 atoms in each lateral direction. We compare the results of a simulation with only a harmonic half space, a system with two explicit atomic planes that interact via the pair potential on top of the half space, and a system with eight additional layers. The anharmonicity of the explicit interatomic interactions leads to a stiffening and a slightly smaller contact area at larger loads. The solid line has slope $1/\kappa = 1/2$.

$h_0' = 0.03$ and $H = 0.5$ was created using the procedure described above. Then all atoms of the lattice with heights below the surface were removed. The elastic substrate is like the nn-fcc case described above. However, since ideal springs would not allow plasticity, neighbors interact with a Lennard-Jones potential that is splined to zero force between 1.2σ and 1.25σ. All systems had 256×256 surface atoms and 256 atomic planes. Two atomic planes make up a unit cell and the spacing of atomic planes d_0 is the nearest neighbor spacing $d_{\rm nn}$ divided by $\sqrt{2}$. To identify plastic deformation, we detect atoms whose environment deviates from the crystal using common neighbor analysis (CNA).[105,106]

Figure 3.12(a) plots the depth of the deepest plastic atom $D_{\rm pl}$ normalized by the spacing of atomic planes d_0. Fully atomistic calculations of the entire volume are used as a benchmark. They are compared to calculations where the top 16 atomic planes (8 substrate layers) are treated explicitly and the remaining atoms are replaced by the Green's function. Note that the Green's function and all atom calculations give nearly identical results until plasticity reaches the depth of the boundary layer. Dislocations can not propagate into the boundary layer, but their motion is not affected by the boundary layer when there are a couple of explicit layers separating them. Arrest of dislocations at the boundary is unavoidable in most continuum/atomistic coupling schemes,[107] with the notable exception of the coupled atomistic and discrete dislocation method.[108] Projections showing the geometry of the dislocations generated in the full and 16 layer calculations are compared in Fig. 3.12(b). The structure is fully captured for the load corresponding to point "1" in Fig. 3.12(b). At point "2", the deepest plastic atom has nearly reached the boundary layer. The largest dislocation loop is slightly suppressed in the 16 layer system, but the remaining dislocations are not affected. At point "3", the dislocations have clearly penetrated past the boundary layer and this can not be captured by the Green's function. Note that this load is comparable to the highest load in Fig. 3.11 and the contact area is close to 16%. We have found that global measures, such as plots of contact area vs. load

are much less sensitive to the number of explicit layers than the dislocation depth.

3.8 Simulations using GF of continuum elasticity

This section connects the GFMD simulation method with the solution of partial differential equations of continuum elasticity. This provides a reference for later chapters.

Many physical systems are described by linear differential equations where an inhomogeneous term represents an external influence on the system. Consider the linear partial differential equation for isotropic continuum elasticity

$$(\lambda + \mu)\nabla(\nabla \cdot \boldsymbol{u}) + \mu\nabla^2\boldsymbol{u} = -\boldsymbol{f} \tag{3.47}$$

This is the Navier equation for solids where $\boldsymbol{u}$ is the displacement field, λ and μ are Lamé constants, and $\boldsymbol{f}$ is the applied force density per volume. (*C.f.* Ref. 26 for background on continuum elasticity.) The problem of interest is to find $\boldsymbol{u}$ in the domain D given boundary conditions that constrain the solution at the boundaries ∂D.

It is common in mathematics to solve this problem with the aide of the Green's function solution. For an introduction to continuum Green's functions, see for example Ref. 109. The Green's function G is the solution to Eq. 3.47 that satisfies the boundary conditions when the inhomogeneous term is replaced by a Dirac delta function. That is,

$$(\lambda + \mu)\nabla(\nabla \cdot G) + \mu\nabla^2 G = -\boldsymbol{\delta}(\boldsymbol{x}) \tag{3.48}$$

which is written compactly by using the identity matrix multiplied by the delta function, $\boldsymbol{\delta}(\boldsymbol{x}) = \mathbb{1}\delta(\boldsymbol{x})$. If the Green's function is known or can be calculated, then the solution $\boldsymbol{u}$ for general inhomogeneous term $\boldsymbol{f}$ can be found immediately by integrating over the domain.

$$\boldsymbol{u} = \int_D G(\boldsymbol{x}, \boldsymbol{x}') \cdot \boldsymbol{f}(\boldsymbol{x}')d\boldsymbol{x}' \tag{3.49}$$

This provides a straight-forward procedure to solve Eq. 3.47, which must be done many

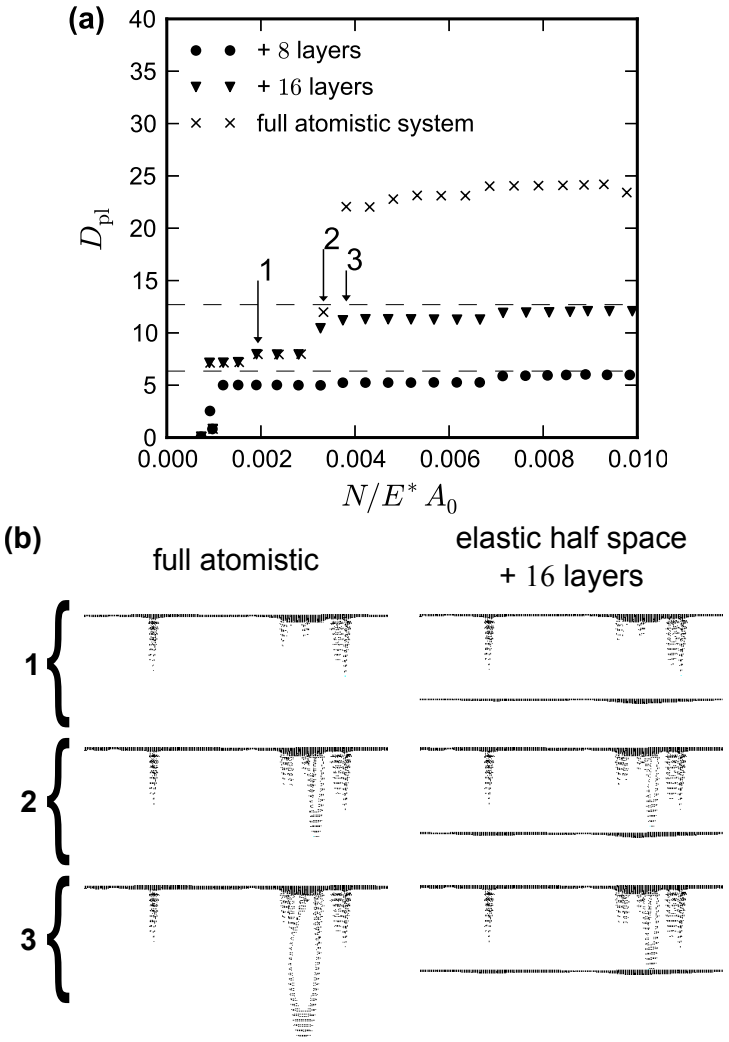

Figure 3.12: (a) Load dependence of the depth $D_{\rm pl}$ of the deepest plastically deformed atom divided by the layer spacing d_0 as determined from a common neighbor analysis (CNA). The Green's function results with 16 atomic planes of explicit atoms follow the all atom calculation until plasticity reaches the Green's function layer. (b) Snapshots showing the projections of the atoms that have displaced plastically as determined from a CNA. The CNA shows dislocation loops are emitted from the surface. Snapshots shown by 1, 2 and 3 correspond to the loads marked 1, 2 and 3 in panel (a) and are recorded at 8, 15, and 16% contact area, respectively. Dislocations in the full atomistic and reduced system behave identically until the deepest dislocation loop hits the elastic boundary where it cannot propagate.

times in a simulation in which the forcing varies.

If the boundary conditions are at infinity, then the system is translationally invariant. G depends only on the difference between the locations, $G(\boldsymbol{x}, \boldsymbol{x}') = G(\boldsymbol{x} - \boldsymbol{x}')$ and Eq. 3.49 is a convolution. Owing to the convolution theorem, the convolution becomes a simple multiplication in Fourier space. The primary cost is performing the Fourier transforms. In a simulation in which the fields are discretized, the convolution may leverage the efficiency of the fast Fourier transform (FFT), and the displacement field is therefore calculated in time $\mathcal{O}(n \ln n)$ where n is the number of elements in the discretized field.

3.8.1 Contact mechanics and surface GF

Of special interest in contact mechanics is the static surface displacement of a 3D elastic half-space under an indenter.[20] To connect this situation with Eq. 3.47, we choose axes $\boldsymbol{r} \to (x, y, z)$ and the domain D to coincide with the half-space $z \leq 0$ with a boundary ∂D at the initial surface position $z = 0$. In a typical contact mechanics problem, boundary conditions specify that the traction $\boldsymbol{\tau}(x, y)$ at the surface is non-zero only at points (x, y) within contacting regions. The interesting part in contact mechanics is that the effective forcing is therefore usually not known *a priori*, as it depends on the displacement field itself and where contact occurs. This often means solving the equation numerically with many iterations of the traction, which can be done with the aide of the surface GF.

The surface GF is the surface displacement $\boldsymbol{u}(x, y, 0)$ from a point loading at the origin on the surface, $\boldsymbol{\tau}(x, y) = \mathbb{1}\delta(x)\delta(y)$. When the boundary conditions specify zero displacement far from the contact, the solution is given by Boussinesq and Cerruti,[20]

$$G_s(x, y) \to \frac{1}{4\pi\mu} \begin{pmatrix} \frac{b}{r} + \frac{2\nu x^2}{r^3} & \frac{2\nu xy}{r^3} & \frac{(2\nu-1)x}{r^2} \\ \frac{2\nu xy}{r^3} & \frac{b}{r} + \frac{2\nu y^2}{r^3} & \frac{(2\nu-1)y}{r^2} \\ \frac{(1-2\nu)x}{r^2} & \frac{(1-2\nu)y}{r^2} & \frac{b}{r} \end{pmatrix} \tag{3.50}$$

where $r = \sqrt{x^2 + y^2}$, $b = (\lambda+2G)/(\lambda+G) = 2(1-\nu)$ and ν is the Poisson ratio. The forcing comes only from the surface $z = 0$, and the convolution to obtain the surface displacement need only occur over x and y.

$$\boldsymbol{u}(x, y) = \int G_s(x - x', y - y') \cdot \boldsymbol{\tau}(x', y')dx'dy' \tag{3.51}$$

Again, for discretized problems, the fast Fourier transform can be used and the surface displacement is calculated in time $\mathcal{O}(n_b \ln n_b)$ where n_b is the number of elements in the discretized field at the surface, $z = 0$. If L is the characteristic system width, then the number of elements is $n_b \sim L^2$. This represents a dramatic reduction in computation time compared to a method that explicitly calculates all bulk displacements, the number of which scale as L^3.

3.8.2 Discretizing Boussinesq-Cerruti in Fourier space

The convolution in Eq. 3.51 occurs as a multiplication in Fourier space. The 2D horizontal Fourier transform of a function $f(\boldsymbol{x}, z)$ can be defined as

$$\tilde{f}(\boldsymbol{q}, z) = \int_{-\infty}^{\infty} f(\boldsymbol{x}, z) exp[-i\boldsymbol{q} \cdot \boldsymbol{x}]d\boldsymbol{x} \tag{3.52}$$

with $\boldsymbol{q} \to (q_x, q_y)$ and $\boldsymbol{x} \to (x, y)$. Transforming Eq. 3.51 gives the displacements in Fourier space as

$$\boldsymbol{u}(\boldsymbol{q}) = \tilde{G}_s(\boldsymbol{q})\boldsymbol{\tau}(\boldsymbol{q}). \tag{3.53}$$

It is natural to consider the analytic form of $\tilde{G}_s(\boldsymbol{q})$. This is derived in Ref. 70 as

$$\tilde{G}_s(q_x, q_y) \to \frac{1}{2\mu q^3} \begin{pmatrix} 2q^2 - 2q_x^2\nu & -2q_xq_y\nu & iq_xq(1-2\nu) \\ -2q_xq_y\nu & 2q^2 - 2q_y^2\nu & iq_yq(1-2\nu) \\ -iq_xq(1-2\nu) & -iq_yq(1-2\nu) & q^2(2-2\nu) \end{pmatrix} \tag{3.54}$$

in the (x, y, z) basis. Here $q = \sqrt{q_x^2 + q_y^2}$.

Note that the GF has a singularity at $q = 0$ (the Γ point). This is the infinite compliance of a semi-infinite half space; a finite average pressure on an infinitely deep, infinitely wide, linear elastic substrate produces infinite displacement. In reality, the stiffness would not be zero but a small finite value set by the depth of the sample. There are several ways to deal with zero stiffness at $q = 0$, but the mean motion of the surface is often not of interest. A simple solution is to set the stiffness at $q = 0$ to one half the value at $q = 2\pi/L$.

It is useful to note the formal scaling of the Green's function. From Eq. 3.50, $G_s \sim 1/r$ and from Eq. 3.54, $\tilde{G_s} \sim 1/q$. The inverse surface Green's function $\tilde{\Phi} = (\tilde{G_s})^{-1}$ satisfies $\boldsymbol{\tau}(\boldsymbol{q}) = \tilde{\Phi}(\boldsymbol{q}) \cdot \boldsymbol{u}(\boldsymbol{q})$. Therefore, $\tilde{\Phi}(\boldsymbol{q}) \sim q$ and $\Phi(\boldsymbol{r}) \sim -r^{-3}$.

3.8.3 Discretizing Boussinesq-Cerruti in real space

A simulation that uses the Green's function of Eq. 3.54 produces slight artificial flattening at the edges of the simulation box. This is because the Fourier transform implies that the fields—including the forcing— are periodic with period of the system size. To avoid effects from the periodic images of the forcing, contact must only occur in a region much smaller than the system size, typically only in a square of side $L/5$.

An alternative approach to avoid periodic image effects (taken from Ref. 110) is to directly use the original analytic real-space GF of Boussinesq and Cerruti, Eq. 3.50. The analytic $\sim 1/r$ solution is sampled on a grid of size $L \times L$ centered at the origin to produce a discrete field. This can then be used as the real-space convolution kernel of Eq. 3.51.

There is an issue in that there is infinite displacement at the origin $r = 0$ in Eq. 3.50 which is due to the fact that force is applied to a single point. The infinity becomes regularized if the force is distributed across a small, finite area. Li and Berger and Li and Pohrt (Ref. 111 and Ref. 112) provide the analytic solution of displacement from a square patch of traction; the solution becomes the Boussinesq-Cerruti solution when the

square size goes to zero but remains finite otherwise. We choose the size of the square traction patch to be the grid cell size. By sampling the Li-Berger solution, we have the exact analytic displacement at points on an $L \times L$ grid centered on an applied pressure at the origin. This is used as the GF in Ch. 6 and Ch. 7.[1]

Note that the $L \times L$-square grid captures the displacement up to distances $L/2$ away from the applied pressure in both $+x$ and $-x$ directions. The response is *not* captured up to distances L away. If contacting objects on the surface are separated by more than $L/2$ in x or y, they do not have the correct interaction. We therefore ensure that all contact occurs only in a square region of side $L/2$, so that all forces and displacements follow the intended Li-Berger solution. As described in Ref. 110, this method entirely excludes the effects of periodic image forces, but requires sacrificing three quarters of the simulated surface area.

3.9 Conclusions

An approach for coupling an explicit atomistic region to a substrate described with a Green's function was developed and tested. The entire system is described by a single Hamiltonian and the only approximation is to neglect anharmonic terms in the substrate. Many other atomistic/coupling schemes introduce ghost forces or can not be described by a single Hamiltonian.[58,61] Previous applications of the Green's function approach have also neglected some forces near the elastic/explicit boundary leading to violations of Newton's third law and ghost forces when interactions extend beyond nearest layers. Our work also demonstrates the extension of the GF method to many-body interactions, creating the opportunity to accelerate a wider range of simulations.

Efficient methods for calculating the Green's function given the interatomic potential were described. Fourier transforming in the plane of the substrate reduces the prob-

[1] The discrete Fourier transform of the Li-Berger solution is then used as $\tilde{G}$ in Eq. 3.53.

lem to a one-dimensional coupling between layers for each in-plane wavevector $\vec{q}$. These equations can be solved using a transfer matrix approach[83,84] or a renormalization group method[85,86] with computational effort that scales as $1/|\vec{q}|$ or $-\ln|\vec{q}|$, respectively. This is order L^2 faster than a previous fluctuation-dissipation formulation for obtaining the Green's function.[19] We have considered only static applications, but present equations for the full dynamic problem with arbitrary masses and damping.

Three tests of the method were discussed. The first is surface relaxation, which reflects the loss of neighbors at a free surface. The Green's function approach accurately reproduced explicit atomistic simulations. The previous Green's function implementation was only accurate for nearest neighbor interactions at zero pressure where relaxation vanishes. The second test was Hertzian contact by a rigid sphere. With no explicit atoms, the elastic Green's function reproduced the analytic response for an elastic continuum. Adding only 8 to 16 atomic planes of explicit atoms allowed anharmonic corrections to Hertz theory to be captured with a relatively modest increase in computer time. The final example was contact with a randomly rough surface with atomic steps that nucleated subsurface dislocations. The Green's function method captured the full response including contact area and dislocation distribution until the dislocations came very close to the elastic layer.

There are several ways in which the current approach can be extended. Periodic changes in elemental composition of the crystal as encountered in nanolaminates can be included straightforwardly by allowing the force-constant matrix to vary spatially. Another extension is to evaluate both the full force and the harmonic approximation for atoms at the elastic/explicit interface. The deviation can be used to estimate errors and determine whether to terminate the calculation or add additional layers of explicit atoms. This addition could be done adaptively on the fly. A third is to include finite temperature. The static elastic response can still be described by a Green's function that must be modified if the temperature is high enough to produce anharmonic effects. The success of recent ex-

tensions of the quasicontinuum method[113,114] suggests that the most important changes in the Green's function can be captured by using the thermally expanded lattice to determine the force-constant matrix.

Chapter 4

Stiffness of contacts between rough surfaces

The presence of roughness on a wide range of length scales has profound effects on contact and friction between experimental surfaces. Under a broad range of conditions,[6,7,41,77,115,116] the area of intimate contact between rough surfaces A_c is orders of magnitude smaller than the apparent surface area A_0. As discussed below, this provides the most common explanation for Amontons' laws that friction is proportional to load and independent of A_0. Because A_c is small, the interfacial region is very compliant. In applications from jet engine mounts to microelectromechanical systems, the interfacial compliance can significantly reduce the stiffness of joints formed by pressing two components together.[115,117]

In this chapter, we examine the effect of surface roughness on the normal and transverse stiffness of contacts between elastic solids using molecular dynamics (MD) and continuum calculations. The results provide a numerical test of recent continuum theories[118,119] and their applicability to real solids. The contact area and normal stiffness approach continuum predictions rapidly as system size increases. Continuum theory also captures the internal deformations in the solid under lateral forces, but the total transverse stiffness may be greatly reduced by atomic-scale displacements between contacting atoms on the opposing surfaces. This makes transverse stiffness a sensitive probe of the forces underlying friction and may help to explain unexpectedly small experimental values.[120]

The topography of many surfaces can be described as a self-affine fractal.[5,6] Over a wide range of lengths, the root mean squared (rms) change in height dh over a lateral distance ℓ scales as a power law: $dh \sim \ell^H$, where the roughness or Hurst exponent H is typically between 0.5 and 0.9. Greenwood and Williamson (GW) considered the peaks of

rough landscapes as independent asperities and found that A_c rose linearly with normal load F_N for non-adhesive surfaces.[6] This explains Amontons's laws if there is a constant shear stress at the interface. A linear scaling of area with load is also obtained from Persson's scaling theory, which includes elastic coupling between contacts approximately.[121,122]

Dimensional analysis implies that the linear relation between load and area must have the form

$$A_c E' = \kappa F_N / \sqrt{\langle |\nabla h|^2 \rangle}. \tag{4.1}$$

where a modulus like the contact modulus E' is the only dimensional quantity characterizing the elastic response, and the rms slope the only dimensionless quantity characterizing the roughness. Numerical solutions of the continuum equations[7,77] show that κ is near 2. Results for different H and Poisson ratio ν lie between the analytic predictions of GW, $\sqrt{2\pi} \sim 2.5$, and Persson, $\sqrt{8/\pi} \sim 1.6$. One advantage of Persson's model is that, as in numerical results, A_c/F_N is constant over a much larger range of loads than GW.[46] Another is that it captures[119] the power law scaling of correlations in contact and stress that was found in numerical studies.[50,76]

The normal stiffness is related to the change in average surface separation u with load. Experiments[123,124] and calculations[116,118,125] show an exponential rise in load with decreasing u, $F_N = cA_0E' \exp[-u/\gamma h_{\rm rms}]$, where $h_{\rm rms}$ is the rms variation in surface height and γ a constant of order 1. Differentiating leads to an expression for the normal interfacial stiffness:

$$k_N^I = -dF_N/du = F_N/\gamma h_{\rm rms}. \tag{4.2}$$

For self-affine surfaces, this interfacial stiffness decreases as $h_{\rm rms}^{-1} \sim L^{-H}$ with increasing system size L. Our simulations test this scaling and show that γ is nearly constant. They also examine the connection between this normal stiffness and the transverse stiffness k_T^I at forces lower than the static friction.[21]

4.1 Computational model

We consider non-adhesive contact of a rigid rough solid and a flat elastic substrate. This can be mapped to contact of two rough, elastic solids in continuum theories.[6,121] The mapping is only approximate for atomic systems,[1,126] but reduces the parameter space. Since thermal fluctuations are usually ignored in continuum theory, we consider the zero temperature limit.

In our MD simulations, substrate atoms separated by r interact with a Lennard-Jones (LJ) potential: $U_{LJ} = 4\epsilon[(\sigma/r)^{12} - (\sigma/r)^6]$, where ϵ and σ are the bonding energy and diameter. To speed calculations, the potential and force are interpolated smoothly to zero at $r_c = 1.8\sigma$ and energy minimization is used to find stable states.[127] Single-asperity simulations[1] yield an effective contact modulus $E' = 64\epsilon/\sigma^3$. The substrate is face-centered-cubic and forms a cube of edge L with a (100) top surface. Periodic boundary conditions are applied in the plane of the top surface and bottom is held fixed. Continuum calculations used the same substrate dimensions but obtained the displacements using a Green's function (GF) for an isotropic, continuous medium with Poisson ratio $\nu = 0$ or 0.35.

The rigid surface contained atoms on a square or triangular grid. The nearest-neighbor spacing d' was chosen to prevent commensurate locking with the substrate.[10,128] The interaction between substrate and rigid atoms is a LJ potential with length σ' truncated at the energy minimum, $2^{1/6}\sigma'$. This produces the purely repulsive interactions assumed in Persson's theory. Rigid atoms are displaced vertically to coincide with a self-affine fractal surface of the desired H. Surfaces with roughness on wavelengths from $l_{min} = 5.9\sigma$ to $l_{max} = L$ were generated as in Ref. 50. The rms slope $\sqrt{|\langle\nabla h|^2\rangle} = 0.1$ for the results shown. Consistent results were obtained for slopes from 0.05 to 0.15. Slopes of 0.2 or greater led to plastic deformation in MD simulations. Large slopes also led to plasticity in previous continuum calculations.[116]

4.2 Results

In all cases studied, A_c rises linearly with F_N. Moreover, the value of κ approaches previous continuum results as system size increases.[7,77] The stress and contact correlation functions from the MD calculations also show the same power law scaling with wave vector found in continuum calculations and Persson's theory.[76,119]

Figure 4.1 shows the variation of F_N with interfacial separation u for several L and $H = 0.5$ and 0.8. In all cases, F_N rises exponentially over a range of loads that corresponds to fractional contact areas between 1 and 10%. Statistics are too poor at lower areas and nonlinear corrections to Eq. 4.1 are seen at larger areas.[7] The linear fits to all results have the same slope, corresponding to $\gamma = 0.48$, and best fit values for all H and L studied differ by less than 10% from this value. GF results were at the higher end of this range and showed no change as ν increased from 0 to 0.35. Earlier continuum calculations,[116] elastic atomic calculations[125] and experiments[124] were consistent with $\gamma \approx 0.4$. This represents a compelling success of Persson's approach, and raises the question of whether γ may have a unique value in the thermodynamic, isotropic limit.

The normal stiffness from Eq. 4.2 includes a component from the increase in contact area with load as well as the change in force at fixed area. There is also an atomic-scale compliance k^{Ia} associated with changes in the separation between contacting atoms on opposing surfaces that is generally neglected in continuum theory. To isolate the stiffness associated with deformation within the substrate at fixed contact area k^{Is}, we applied constraints directly to the substrate atoms that contacted at a given load. The normal and lateral stiffness were then obtained from the linear change in force produced by small, uniform normal or transverse displacements of these contacting atoms. The contribution from the bulk response was subtracted so that the stiffness reflects the change in surface separation u or transverse surface translation, u_T. This approach is straightforward to

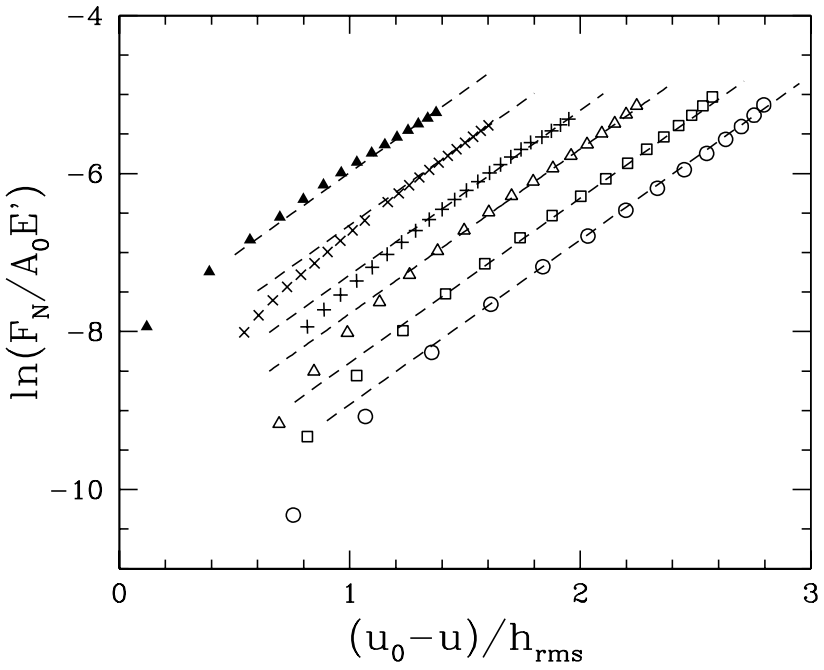

Figure 4.1: Logarithm of load as a function of $(u_0 - u)/h_{\rm rms}$, and linear fits corresponding to $\gamma = 0.48$. The separation at first contact, u_0, is shifted slightly to prevent overlap. Atomistic results are for $H = 0.5$ with $L = 378.4\sigma$ (circles), 189.2σ (squares), and 94.6σ (triangles) and for $H = 0.8$ with $L = 189.2\sigma$ (crosses) and 94.6σ (pluses). Filled triangles are for a GFMD simulation with $L = 128d$ and $\nu = 0$.

implement in experiments and was found to be consistent with direct averaging of atomic separations.

Figure 4.2(a) shows the scaled normal interfacial stiffness $k_N^{Is} h_{\rm rms}/A_0 E'$ as a function of the dimensionless load F_N/A_0E' used to identify the contacting atoms that are displaced. Once again, results for all systems show the same behavior, and the stiffness rises linearly with load as predicted by Eq. 4.2. The points lie slightly above the dashed line corresponding to $\gamma = 0.48$ due to small deviations from the analytic form of Eq. 4.2. One might expect k_N^{Is} to be substantially less than the total stiffness because it does not include the stiffness from increases in contact area. However, the two stiffnesses are nearly the same because newly contacting regions carry the smallest forces.

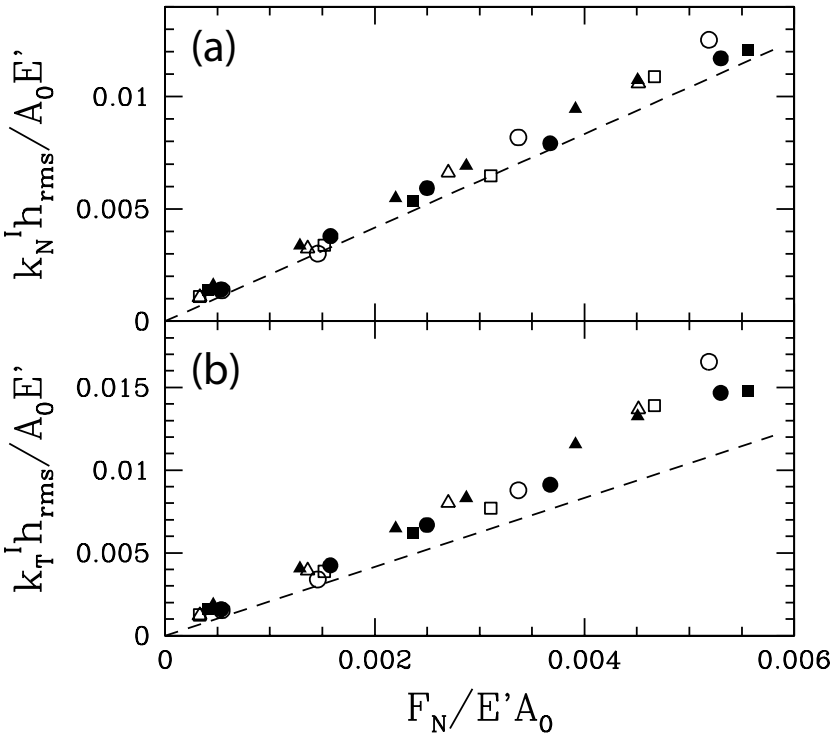

Figure 4.2: The scaled (a) normal stiffness and (b) transverse stiffness as a function of F_N/A_0E'. Results are for $H = 0.5$ (open symbols) and $H = 0.8$ (filled symbols) with $L = 189.2\sigma$ (circles), $L = 94.6\sigma$ (squares) or $L = 47.3\sigma$ (triangles). Dashed lines have slope $1/\gamma$ with $\gamma = 0.48$.

The incremental response of an ideal elastic solid does not depend on any preexisting deformation. This implies that we should obtain the same stiffness by displacing the same set of atoms on the initial undeformed surface. Direct evaluation of the stiffness in this way gave slightly lower values than Fig. 4.2, with the difference increasing from the numerical uncertainty to about 15% with increasing F_N. This provides an estimate of the contribution that anharmonic effects may make to the stiffness of real materials at the rms slope used here.

The above results imply that the stiffness of elastic solids at fixed contact area is uniquely determined by the distribution of contacting points and not the surface roughness

or load distribution. This conclusion may seem at odds with Eq. 4.2, since the contact area has no independent connection to load or surface roughness. The resolution is that variations in load and roughness cancel. If the response is linear, one can scale $h_{\rm rms}$ and F_N by the same factor and the contact area will be unchanged. Indeed one can combine Eqs. 4.1 and 4.2 to eliminate F_N:

$$k_N^* \equiv \frac{k_N^I}{A_0 E'} \frac{h_{\rm rms}}{\sqrt{\langle |\nabla h|^2 \rangle}} = \frac{1}{\kappa\gamma} \frac{A_c}{A_0}. \tag{4.3}$$

For a self-affine surface, the ratio $h_{\rm rms}/\sqrt{|\nabla h|^2} \propto (l_{\rm max}/l_{\rm min})^H l_{\rm min}$ depends only on the small and large scale cutoffs in roughness.

Figure 4.3(a) shows the scaled stiffness k_N^* vs area. The results were obtained by displacing atoms from their positions on the initial flat surface to eliminate anharmonic effects. Results for all systems collapse onto a common straight line, providing clear evidence for the direct connection between stiffness and contacting area. The slope is near unity as expected from the separate values of κ and γ.

All of our atomic simulations show $k_T^{Is}/k_N^{Is} \geq 1$. This is surprising given that Mindlin[21] and recent work[53] predict $k_T^I/k_N^I = 2(1-\nu)/(2-\nu) \leq 1$. However, this work assumed isotropic elasticity and the predicted ratio of unity is consistent with our GF results for an isotropic solid with $\nu = 0$. One measure of the anisotropy of the LJ crystal is that the ratio $c_{44}/E' \approx 0.57$, while it is $(1-\nu)/2 \leq 1/2$ for an isotropic solid. The higher shear modulus is consistent with a higher transverse stiffness than expected. In general, the total elastic energy stored in the interface is $\Sigma_q \vec{f}(-\vec{q}) \overleftrightarrow{G}(\vec{q}) \vec{f}(\vec{q})/2$ where G is the Green's function matrix relating displacements to forces f.[19] The stiffness ratio can be obtained by averaging the diagonal components of $qG(\vec{q})$ corresponding to normal and transverse displacements over $\hat{q}$ and assuming the same power spectrum describes the respective forces. This ratio agrees with Mindlin's result for isotropic systems, and captures

changes with crystal anisotropy.

As noted above, k_N^{Is} and k_T^{Is} reflect the stiffness associated with deformation inside the substrate at constant A_c, and there are additional interfacial stiffnesses k_N^{Ia} and k_T^{Ia} associated with the relative motion of atoms on opposing surfaces. The substrate and atomic compliances add in series, so the total interfacial stiffness $k_J^{It} = [1/k_J^{Is} + k_J^{Ia}]^{-1}$ for $J = N$ or T. As in previous studies of single-asperity contacts,[1,10,128] we find atomic-scale deformations have almost no effect on the total normal stiffness of multiasperity contacts, but qualitatively change the transverse stiffness.

The value of k_N^{Ia} is large because the repulsive forces on all contact atoms add coherently to prevent interpenetration. One can estimate $k_N^{Ia} \sim A_c E'/\sigma$, assuming that the interfacial atoms act like a piece of the substrate with area A_c and height equal to the lattice spacing $\sim \sigma$. This is larger than k_N^{Is} by a factor of order $h_{\rm rms}/\sigma\sqrt{\langle|\nabla h|^2\rangle} \gg 1$, explaining why the total normal stiffness (Fig. 4.1) is consistent with the stiffness from compression of the elastic substrate alone (Fig. 4.2).

In contrast, the contributions to transverse stiffness from different atoms rarely add coherently. There is a direct analogy to friction forces in single-asperity contacts,[1,10,128] where the resistance to lateral sliding rises sublinearly with the area unless the surfaces share a common periodicity. In Fig. 4.3(b) the total transverse interfacial stiffness is 2 orders of magnitude lower than k_T^{Is}. Results for different H are nearly the same, but the stiffness changes significantly with the lattice spacing d' and surface structure (square vs triangular). The transverse stiffness is also affected by l_{min}, L, and the interfacial potential.

Our k_T^{Ia} results for a wide range of parameters fall into two categories. The stiffness adds coherently in special cases, such as for commensurate surfaces with the same lattice structure. As for the normal stiffness, the contribution from k_T^{Ia} is proportional to A_c and becomes irrelevant as system size L increases. For the more usual case where the different periodicity of the surfaces prevents coherent locking, k_T^{Ia} grows sublinearly with A_c and

dominates the total stiffness at large L and A_c. Data for the cases in Fig. 4.3(b) satisfy $k_T^{Ia} = cA_c^{1/2}E'$, where E' is included to make c dimensionless and there are statistical fluctuations about the fit as new asperities contact. The value of c was independent of L and H, but larger for the square lattice than the triangular lattice. The substrate stiffness $k_T^{Is} \propto L^H A_c$ [Eq. 4.3] grows more rapidly with L and A_c and thus becomes irrelevant in large systems.

Two aspects of the above results should be noted. The first is that the scaling $k_T^{Ia} \propto A_c^{1/2}$ is consistent with our observation that different connected patches contact at random lateral registries because they could not displace laterally to optimize their position. Scaling theories predict that substrate stiffness prevents relative lateral displacements for L less than a correlation length that is estimated to be comparable to the size of macroscopic samples.[129] The second point is that the same arguments predict that the friction force scales as $A_c^{1/2}$ and this is not usually found in experiments. This suggests that another mechanism, such as debris or plasticity, may be important to both interfacial stiffness and friction in experimental samples. Further studies of interfacial stiffness may thus provide valuable information about friction mechanisms as well as explain the low ratio of transverse to normal stiffness frequently observed in friction.[120]

4.3 Conclusion

In conclusion, atomic scale simulations were used to study contact between surfaces with roughness on a wide range of scales. The results for area and normal stiffness are consistent with Persson's continuum theory down to relatively small scales, even though the solid is not continuous or perfectly elastic. The area and internal stiffnesses of systems with a range of H, L and ν show the linear scaling predicted in Eqs. 4.1 - 4.3 with nearly constant values of κ and γ. The internal stiffnesses were shown to depend only on the geometry of the contacting region. Atomic-scale displacements between contacting atoms have little effect

on the normal stiffness, but can change the lateral stiffness by orders of magnitude. This sensitivity makes transverse stiffness a promising probe of the atomic-scale interactions that underlie friction.

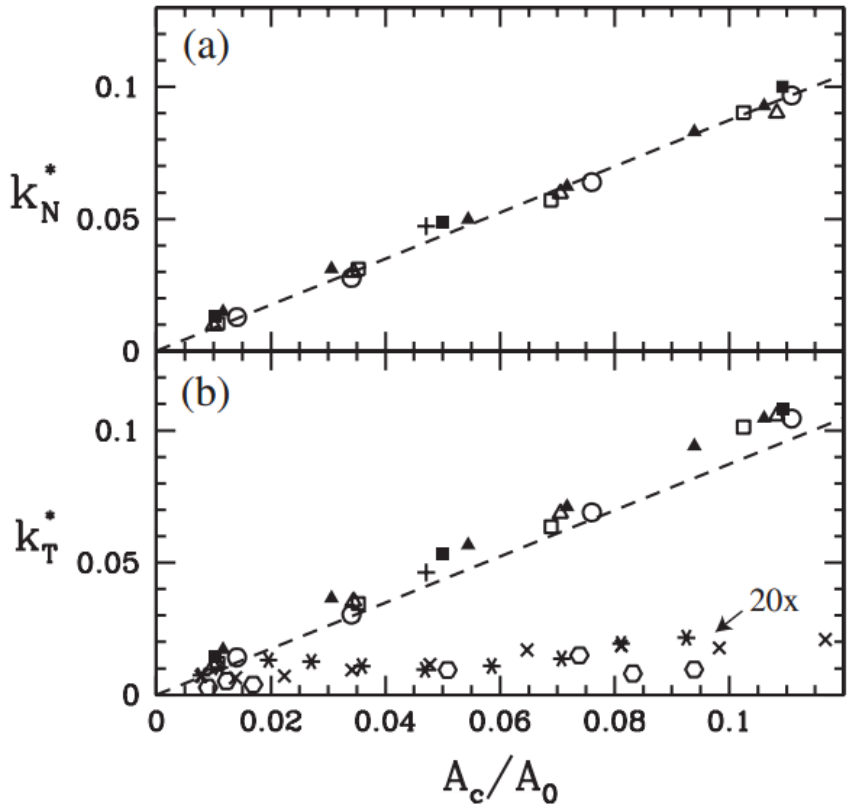

Figure 4.3: The scaled (a) normal stiffness and (b) transverse stiffness as a function of A_c/A_0. Results are for $H = 0.5$ (open symbols) and $H = 0.8$ (filled symbols) with $L = 189.2\sigma$ (circles), $L = 94.6\sigma$ (squares) or $L = 47.3\sigma$ (triangles). Pluses show GFMD results for $\nu = 0$. Total transverse stiffness k_T^{It}, multiplied by 20 to make it visible, is shown for $L = 189.2\sigma$ and rigid surfaces with a square lattice, $d' = 0.37\sigma$, and $H = 0.5$ (cross) or $H = 0.8$ (hexagons), or a triangular lattice with $d' = 2^{1/6}\sigma$ and $H = 0.8$ (*). Dashed lines have slope 0.87.

Chapter 5

Normal contact of rough crystalline solids

Microscopic roughness on solid surfaces determines a wide variety of technologically important properties of contacting objects. The fact that contact area is only a small fraction of surface area in a broad range of conditions is a key insight into correct explanations of friction, electrical contact, thermal contact, leaking of seals, and interface stiffness. These surface properties can be especially important in micro- and nano-scale devices, where, at the same time, precise engineering may enable the surface geometry to be controlled. Correspondingly, there has been sustained interest in quantitative predictions about the statistical properties of rough contact.

Most previous work assumes that each contacting object consists of a continuum elastic material with a surface that is sharply-defined and smooth on the smallest length scales. Theoretical modeling, notably by Persson,[48,49] has made great progress in developing predictions for the amount of contact area, stiffness, and pressure distribution in rough contacts. Systematic numerical studies with isotropic linear elasticity support the central results, showing deviations almost always less than 50% from predictions.[45]

One troubling aspect of continuum predictions is that the root-mean-squared (rms) slope sets the contact area, and the dominant contribution to the measured rms slope of rough surfaces usually comes from the smallest resolved scale. Of course, solids are not continua but are composed of discrete atoms. If one resolves surface topography all the way to atomic length scales, definitions of the rms slope become ambiguous. Our lack of understanding of how these continuum parameters map onto a real-world solid hinders the application of continuum theories.

In this work we use molecular dynamics simulations (MD) to directly simulate normal contact between rough solids on the atomic scale. MD provides a natural framework to consider atomic-scale features that continuum treatments typically neglect. The atomic steps found at the surface of crystalline solids are a striking example known to present problems for continuum treatments.[1,126] The MD simulations can also test the common assumptions of using linear elasticity and low-friction, hard-wall interactions across the interface.

Previous indications about the validity of large-scale continuum results for atomic solids are mentioned in work by Almqvuist *et. al.*[130] though atomic solids were not the main focus. Large simulations conducted in two dimensions found that stepped surfaces caused significant deviations from continuum expectations.[126]

In this work, we conduct large three-dimensional investigations of atomic rough contact which are now possible thanks in part to fast, rigorous methods such as the Green's function molecular dynamics (GFMD) method.[19,51] We study bent, elastic solids with quasi-hard-wall interactions to mimic the continuum description. We then include more realistic atomic-scale features at the interface, such as atomic-scale compliance at the interface or atomic surface steps. Finally, to probe effects beyond linear elastic response, a lattice of Lennard-Jones (LJ) atoms is used as the substrate.

We find that many of the large-scale properties can be explained with continuum theory, while there are large deviations at small scales. We suggest definitions of the surface slope and contact area of these atomic systems and we find that the expected linear relationship between normal load and contact area holds. The contact area is modified only up to 50% from the continuum case for elastic substrates. Atomic surface steps rearrange the surface pressure up to length scales associated with the step spacing, which may be considerably larger than the atomic length scale. In addition, edges produce regions of very high pressure.

When the substrate is composed of LJ atoms, we choose surface roughness parameters to produce elastic or slightly elasto-plastic behavior. Even the lowest-roughness surfaces produce plasticity, but the contact properties remain nearly the same as the purely elastic case. More plasticity occurs under higher-roughness surfaces, especially at step edges, and the contact area can be increased several times above the result for elastic surfaces. Stepped surfaces are more effective at creating plasticity than bent surfaces and correspondingly they obtain larger contact area at the same load despite having the same continuum-level roughness description. This constitutes an example of atomic-scale features controlling the macroscopic properties of normal contact.

5.1 Continuum description

Many rough surfaces are approximately described as statistically self-affine fractal over a large range of length scales.[40,131] That is, the average change in surface height dh scales as a power law of lateral distance, $dh = \langle |h(\mathbf{x} + \mathbf{dx}) - h(\mathbf{x})| \rangle \propto dx^H$, where H is called the Hurst exponent,[103] and $\mathbf{x}$ and $\mathbf{dx}$ are two-dimensional vectors in the plane of the surface. H is found to have values between 0.5 and 0.8 for many measured surfaces.[132] The self-affine scaling holds over a range of length scales $L_{max} > dx > L_{min}$, where L_{max} cannot be larger than the system size and L_{min} cannot be smaller than the scale of atoms that form the surface.

Many models of rough contact (*c.f.* Ref. 48 for a partial review) predict an approximately linear increase in contact area A with load F up to moderate fractional contact area. While some of the models are quite sophisticated, the relationship between contact area and load might be guessed from dimensional analysis. A dimensionless quantity may be constructed by dividing F/A by a modulus like the contact modulus E' (as in Hertzian contact, Eqn. 2.2). If the surface geometry introduces no additional length scales, then the ratio may only be equal to a dimensionless constant whose value may depend on the surface

geometry. For a statistically random surface, assuming linear elastic response, a natural dimensionless quantity to characterize the roughness is the rms slope $h'_{rms} \equiv \sqrt{\langle |\nabla h|^2 \rangle}$. Here, $\langle ... \rangle$ refers to averaging over the surface. Dimensional analysis therefore suggests that at low contact area,

$$AE' = \kappa F / h'_{rms} \tag{5.1}$$

which is supported by the findings of analytic models[7,48] and numerical work.[7] Numerical work has found κ to have values in the range of $1.5 - 3.0$ at these contact areas for different roughness parameters.[7,45]

The fact that area is proportional to load implies that the mean contact pressure, $\langle p \rangle \equiv F/A$, is independent of load. Not only the mean pressure, but the full distribution of pressures on the surface, $P(p)$, is of considerable importance in tribology. For example, regions of high pressure may produce plastic yielding (*c.f.* Sec. 5.3.2) or can be the dominant regions contributing to friction (*c.f.* Ch. 6). The continuum theory of Persson leads to a distribution function $P(p/\langle p \rangle)$ whose form is independent of load and that goes to zero at both low and high pressures.[133]

Also of technological interest is the mechanical stiffness of the rough contact. The small contact area leads to a low interfacial stiffness which can often be lower than the bulk stiffness and therefore dominate the response. Ch. 4 discussed that in linear systems, the normal stiffness is the derivative of normal load with respect to the mean surface separation u, *i.e.* $k_N^I = -dF/du$. Continuum work[42,116,118] (see Fig. 4.2) shows that normal stiffness increases linearly with load,

$$k_N^I = F/\gamma h_{rms} \tag{5.2}$$

where F is the load and h_{rms} is the rms surface height. Integrating this relation, one finds

that the load falls exponentially with surface separation

$$F = cA_0E'exp[-u/\gamma h_{rms}] \tag{5.3}$$

where A_0 is the apparent area and γ is a dimensionless constant found to have value of about 0.5.

Continuum contact theories typically implicitly assume that surfaces are mathematically smooth below length scale L_{min}. It is not clear how to apply continuum theory when L_{min} is on the scale of atoms or when there are other features below the scale of L_{min} such as atomic steps. In fact, inserting sharp atomic steps in a linear elastic description produces infinite stress at the step edges, as described in Ch. 2. The theories also assume that there is no friction in the contact during loading, but in real systems, atomic geometry can cause the surfaces to pin together and produce high friction. Other typical assumptions include small root-mean-squared (rms) surface slope, linear elastic response, hard-wall repulsion, and continuously-varying stress fields.

5.2 Simulation methods

We use molecular dynamics simulations[81] (MD) to simulate rough contact between atomic solids. In most cases we consider a rigid rough upper solid and a compliant flat substrate. Choosing to work in this limit reduces the parameter space for this study, and this limit can be mapped to the general case of two rough elastic solids in the small-rms-slope, linear-elastic case. Cases that include roughness on the substrate are described at the end of the chapter and follow the same trends.

Each solid consists of a face-centered cubic (fcc) atomic lattice of nearest-neighbor spacing a_0. The lattices are both oriented with the (001) surface in the contact ($x-y$) plane. The lattices are also both rotated 45 degrees about the z-axis so that the [110] direction is along the x-axis and surface atoms form a square x-y grid. Since the rough upper solid

is rigid, only the surface atoms of the upper solid need to be included in the simulation. The surface roughness on the solids is generated using the Voss midpoint displacement algorithm.[40] This algorithm produces a random surface $h(\mathbf{x})$ with self-affine scaling between the system size, L, and the grid size, a_0. We then impose the small-wavelength cutoff to the scaling by removing the Fourier components of the surface that are above a specified wavenumber, $2\pi/L_{min}$.

This rough surface $h(\mathbf{x})$ is then used as a template to create roughness on an atomic crystal by one of two methods. The first method (Fig. 5.1(a)) consists in vertically displacing atoms on the rigid surface to follow $h(\boldsymbol{x})$, producing an atomic surface that resembles a bent lattice. The bent surface is close to the surface assumed in continuum theory, but artificial. In the second method (Fig. 5.1(b)) all atoms in the rigid crystal remain on lattice sites. Any atoms below the surface $h(\boldsymbol{x})$ are removed, leaving behind atomic steps of height $a_0/\sqrt{2}$ on the surface of the block.

The substrate surface has dimensions $L \times L = 1024a_0 \times 1024a_0$. Separate studies with $L = 2048a_0$ gave equivalent results. Lateral boundary conditions are periodic to avoid edge effects. To capture the stress field that extends far from the surface into the bulk, the substrate has a depth of 970 atomic planes (485 fcc cells). The bottom atomic plane is held rigid.

We consider two substrate materials, referred to as fcc LJ and fcc elastic, that have different interatomic interactions. For fcc LJ, atoms within the substrate lattice interact with a standard 6-12 Lennard-Jones (LJ) pair potential, $V(r, \epsilon, \sigma) = 4\epsilon((\sigma/r)^{12} - (\sigma/r)^6)$, with energy and length scales ϵ and σ. To speed calculations, the pair potential is taken to be zero at distances greater than $r = 1.25\sigma$. This is done smoothly in a standard way[81] – by interpolating the force using a spline between its value and slope at $r = 1.2\sigma$ to zero force and zero slope at $r = 1.25\sigma$. The top 16 atomic planes are simulated explicitly in MD, whereas the deeper parts of the lattice are replaced with their linear response using the Green's

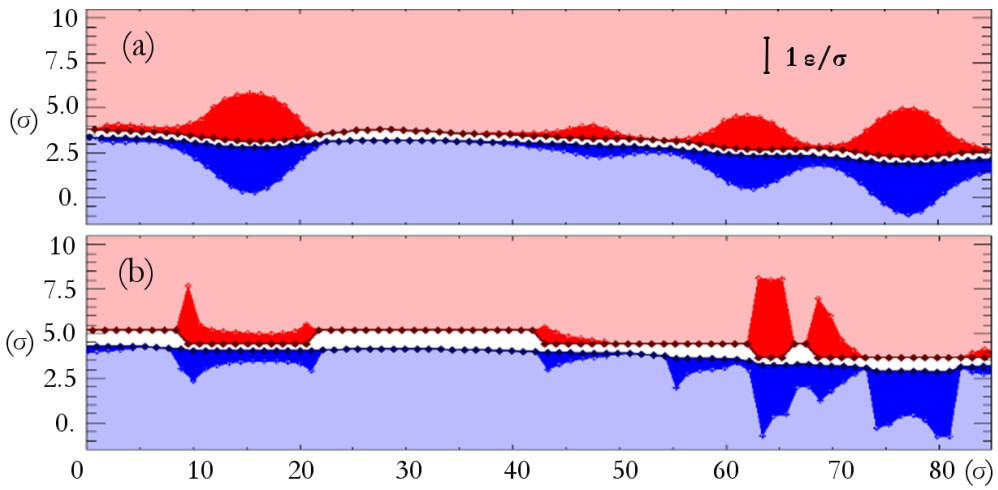

Figure 5.1: A slice through a small region of simulated 3D rough contact is shown for two geometries at the same normal load. Atoms are circles and the normal pressure at the atomic scale is shown by shading by a distance proportional to the atomic force. The upper solid is held rigid (red) and the substrate (blue) is fcc elastic and initially flat. In (a) the bent upper atomic lattice closely approximates the continuum picture with the height of atoms equal to the continuum $h(\boldsymbol{x})$. The shading shows that the pressure is distributed very differently than in (b) where removing atoms below $h(\boldsymbol{x})$ produces atomic surface steps. In (b), step edges produce sharp fluctuations of the pressure. Since the simulation is 3D, the pressure has fluctuations perpendicular to the cross section plane as well. The apparent violation of Newton's third law in (b) at positions from 72 to 82 σ is due to a step edge of the upper solid that is not visible, because it is clipped out by the cross-section viewing plane. The atoms directly above (shown) feel no force, since the substrate atoms are pushed down by atoms that are outside the viewing slice. These sharp fluctuations are an atomistic effect that leads to increased plastic rearrangement, as discussed in Sec. 5.3.2.

function approach. The simulation thus retains atomic fidelity in high strain regions near the surface while reducing the computational load in regions far from the surface. Notably, the explicit MD layers near the surface allow the nucleation of dislocations to relieve stress (Fig. 3.12). Simulations with 8 atomic planes gave nearly identical results for surfaces with $h'_{rms} < 0.4$. The fcc elastic case is simply obtained by removing all explicit MD layers. The response of the substrate is then a harmonic approximation to the LJ interactions. The material has the same stiffness as fcc LJ but is completely elastic with no anharmonic or plastic response.

We also consider two wall interactions. In the baseline case, called LJ repulsive, atoms of opposing solids interact with the standard LJ potential that is cut at the minimum, $r_{cut} = 2^{1/6}\sigma$, producing a purely repulsive interaction. This wall potential can lead to strong friction between the surfaces. The reason is illustrated using the iso-potential surface of a line of atoms along the surface in Fig. 5.2. An atom sliding past the surface can become pinned in the sharp indentations between atoms, referred to as the atomic corrugation. To further connect with continuum calculations that assume hard-wall repulsion and no friction, a stiffer and less corrugated potential can be used. For this the LJ radius is expanded by 2σ and the range of interactions is halved using the potential $V(r - 2\sigma, \epsilon, \sigma/2)$ cut at the minimum, $r_{cut} = (2+2^{-5/6})\sigma$. This interaction is four times as stiff and importantly creates less friction between the surfaces because there is less atomic corrugation (Fig. 5.2). For shorthand, we will refer to this as the quasi-hard-wall potential. The simulation properties that are to be contrasted are summarized in Table 5.1.

Quasi-static loading is applied by lowering the rigid upper surface by small increments and minimizing the system energy with each increment. The load and the contact area increase with successive displacement steps, and the upper solid is allowed to translate in the lateral directions to maintain zero net force.

An effective contact modulus, $E' \approx 68\epsilon/\sigma^3$, of the substrate lattice is found using a

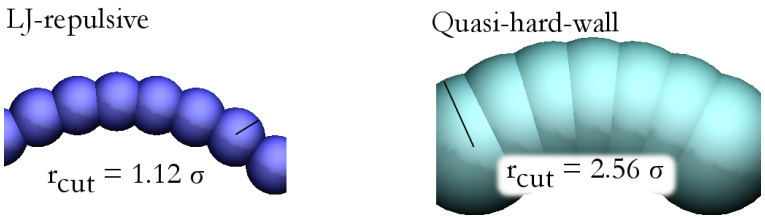

Figure 5.2: Potential iso-surface ($V = 0^+$) of a bent chain of atoms using two wall potentials (LJ repulsive and quasi-hard-wall) to illustrate atomic corrugation. Although the chain is smoothly bent, an atom sliding along the surface experiences structure associated with the large slopes of the isosurface for the LJ repulsive case.[42]

	"Baseline"	"Altered"
Atomic surface character	Bent	Stepped
Material	fcc LJ	fcc elastic
Interfacial atomic interaction	LJ repulsive	Quasi-hard-wall

Table 5.1: Summary of the investigated material properties. The previous chapter (Ch. 4) focused on simulations with the properties labeled "baseline." In this chapter, each of the three material properties are altered to investigate the effects of the atomic features on the contact properties. All combinations of baseline and altered properties are considered. Additionally, the baseline continuum topography has the following properties: $H = 0.5$, $h'_{rms} = 0.15$, $L_{min} = 6\sigma$, $L_{max} = 1024\sigma$.

large spherical indenter and by comparing the pressure with the Hertz solution as reported previously.[42] The LJ lattice has yield stress $\sigma_y = 1.64\epsilon/\sigma^3$ along the (111) slip plane in the [010] direction. The rms slope of the template h'_{rms} is varied from 0.07 to 0.40 which represents the range between purely elastic contact and fully plastic contact in previous studies.[116]

5.3 Results

A bent geometry and a stepped geometry are contrasted in Fig. 5.1. The two surfaces were created using the same continuum template and have the same large-scale shape. They are also at the same normal load. Shading shows that the pressure is distributed very differently. The presence of atomic steps redistributes the pressure on the surface, concen-

trating pressure at the step edges. Statistical distribution functions allow more quantitative assessment of the contact properties.

5.3.1 Gap function and mean surface separation

The gap function provides insight into definitions of contact area and mean surface separation. It is defined as the distribution P of normal interfacial separations u, $P(u) = \langle \delta(u(\boldsymbol{x}) - u) \rangle$ where $u(\boldsymbol{x})$ is the vertical separation at location $\boldsymbol{x}$ along the surface. A corresponding function for discrete systems can be defined as follows. A surface atom i of the upper solid has position (x_i, y_i, z_i) and the vertical distance to the nearest atom of the substrate is u_i. Then the fraction of the N surface atoms having a nearest substrate atom within a range du centered on u is $P(u)du = 1/N \sum_{i=1}^{N} \Theta(-|u_i - u| + du/2)$, where $\Theta(x) = 1$ if $x > 0$ and $\Theta(x) = 0$ otherwise. We also repeat the analysis using the true (3D) separation u_t rather than vertical separation u. The distribution $P(u_t)$ can be more relevant since, for example, pair potential forces depend on the 3D separation. (The distinction between the two distributions is a minor point since the two versions are nearly the same for low-slope surfaces and $u > 1.5a_0$.)

Fig. 5.3 shows $P(u_t)$ for stepped and bent surfaces with different repulsive interactions at applied normal pressure $F/L^2E' = 0.0059$. The distribution at large u is nearly the same for bent and stepped surfaces and for different repulsive interactions. The total fraction of substrate surface atoms near contact can be determined from the cumulative distribution function of separation, $C(u_t)$. We see that the majority of the surface is at large separations, with more than 90% beyond the interaction range. The data also show that a lateral shift between different surfaces to reach the same C is at most a few percent of the lattice spacing. For the cases shown, the substrate material is fcc elastic but changing to fcc LJ produced almost no effect for all cases within the range considered ($0.07 < h'_{rms} < 0.40$).

In Fig. 5.4 the view of the gap function is expanded to show the strong peak near

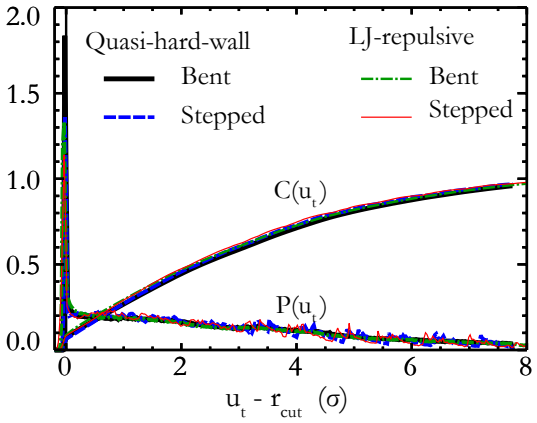

Figure 5.3: The gap function $P(u_t)$ and cumulative distribution function of separation $C(u_t)$ are plotted for stepped surfaces and bent surfaces at matched applied normal load $F/L^2E' = 0.0059$. Atomic scale changes do not affect the gap function at separations greater than a fraction of a lattice constant. The substrate material is fcc elastic. The visible small-scale oscillations in $P(u_t)$ at large u_t for stepped surfaces are due to the discrete heights of the surface steps. The continuum template surface had $h'_{rms} = 0.15$, $L_{min} = 12\sigma$, $H = 0.5$, $L = 1024\sigma$. The peaks at small gap are examined in Fig. 5.4.

the onset of repulsion that represents the change induced by contact and which grows with increasing load. There are small-scale differences between surfaces. For all surfaces the peak is centered slightly below the onset of repulsive forces at r_{cut}. The hard wall assumption of continuum theory would lead to a δ-function at r_{cut}. Here, the finite rate at which repulsion rises leads to a spread of values below r_{cut}. The peak for quasi-hard-wall interactions is roughly twice as sharp because the characteristic length of the wall interaction is $\sigma/2$ instead of σ (Sec. 5.2). Note that changing from the bent to the stepped surfaces has little effect on $P(u_t)$ at these separations. We will see in the next section that these changes at small separation lead to significant changes in pressure and contact area.

One common definition of contact is that a contacting atom experiences a repulsive force from the opposing surface. With this definition, the fractional contact area is then simply $C(r_{cut})$. There is some ambiguity with this definition, since the force is vanishingly small near r_{cut}, and in real systems it may not be possible to sharply know r_{cut}. But

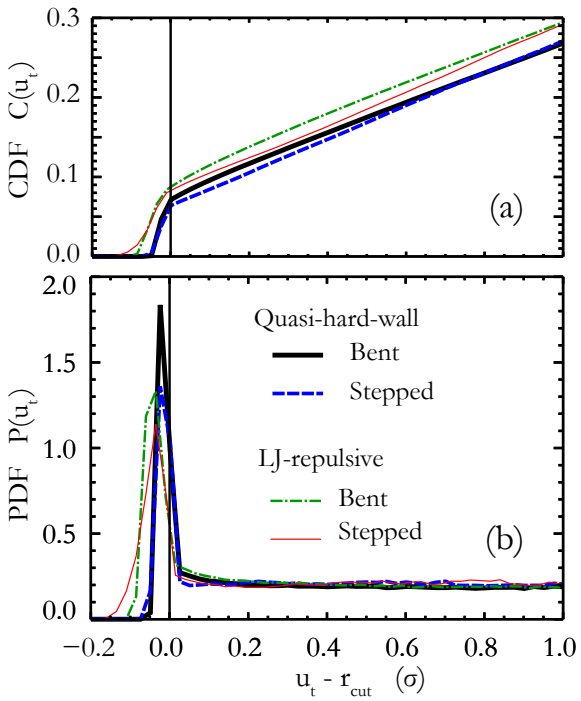

Figure 5.4: Expanded view of the plots in Fig. 5.3 at small separations. (a) Cumulative distribution function of separation $C(u_t)$ and (b) gap function $P(u_t)$. Changes in atomic geometry and atomic interaction produce only small changes in the gap function, almost all near $u_t = r_{cut}$. The area within $r < r_{cut}$ is 8.0% and 8.4% for the stepped and bent cases. Changing from a LJ-repulsive wall interaction to quasi-hard-wall decreases the area to 6.4% and 7.2% respectively.

Fig. 5.4 shows that there is a distinct peak in $P(u_t)$ at contact and that the amount of fractional contact area is insensitive to whether the full repulsive region is included or just the peak of $P(u_t)$. This is discussed further in Sec. 5.3.4. In the following sections we use $C(r_{cut})$ as a definition of fractional contact area which captures trends common to all definitions considered, as described in Sec. 5.3.4. The contact area ($C(r_{cut})$) varies between 6-9% contact area for the cases shown and will be discussed in more detail in the section on contact area, Sec. 5.3.2.

The changes in mean gap with load give the contribution of the interface to the normal compliance (Ch. 4). The mean gap is defined by $\bar{u} \equiv \int_0^\infty duuP(u)$. Given the lack of sensitivity of $P(u)$ in Fig. 5.3 to the parameters in Table 5.1, we expect the normal interfacial stiffness also to be insensitive. Fig. 5.5 shows the variation of the mean separation with load for different atomic systems. Over 8 orders of magnitude in force, the mean separation is the same for all cases to within a fraction ($\sim 10\%$) of the rms height h_{rms}. Moreover, the small shift is nearly constant so it has little effect on the derivative which gives the stiffness. At very small loads there is only a single contact. At larger loads there is a statistical distribution of contacts from the rough surface, and the mean separation follows Eqn. 5.3. All cases investigated follow the slope of the line corresponding to $\gamma = 0.45$, which is the result found earlier for bent elastic systems in Ch. 4.[42]

5.3.2 Measures of area and plasticity

Continuum simulations predict proportionality between load and area for both elastic and elastoplastic contact.[116] Fig. 5.6(a) shows that this holds in atomic systems as well, for bent and stepped surfaces with elastic or LJ interactions. All four cases have the same continuum template. The area-vs-load data are similar for all four cases, with the stepped geometry on an fcc LJ solid producing the most contact area at a given load.

The stepped geometry on an fcc LJ solid is also the case that produces the most

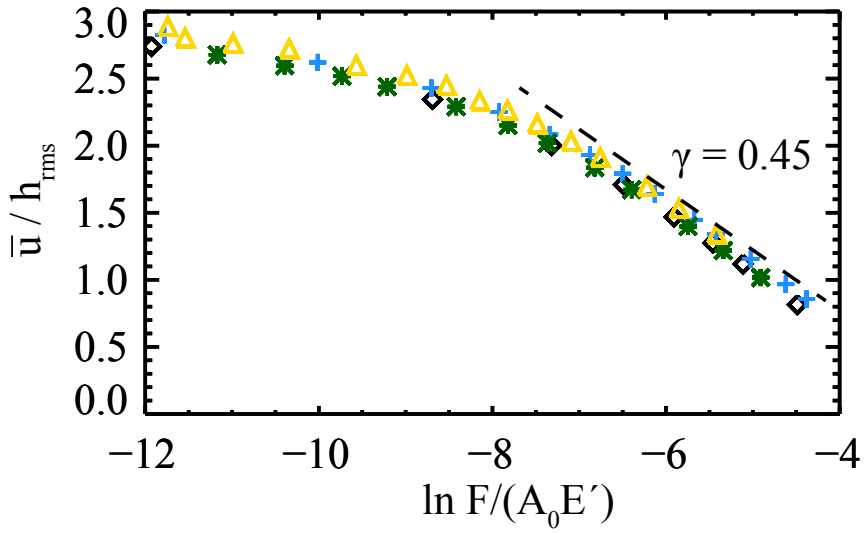

Figure 5.5: Shown is the load dependence of the surface separation. Surfaces are elastic bent (black diamonds), elastic stepped (blue crosses), LJ bent (green asterix), and LJ stepped (yellow diamonds). The surfaces were formed from a continuum template with $h'_{rms} = 0.3$ and $L_{min} = 6\sigma$.

plasticity, as seen in Fig. 5.6(b). The plotted measure of plasticity is the number of changes to the list of neighboring atoms. Here we define neighboring atoms to be those within 1.25σ of one another. Relatively large deformations that are associated with plasticity, like the movement of a partial dislocation in the fcc lattice, cause atoms to leave the 1.25σ-shell of some atoms and enter the shell of others. This appears as insertions and deletions with respect to the original neighbor list. We found that the changes to the neighbor list agree well with a common neighbor analysis (CNA) of which subsurface atoms have left a locally fcc structure.[80] The number of changes to the neighbor list is larger than the number of atoms that participate – a subsurface atom in the fcc structure has 12 neighbors for example. This plasticity analysis based on the neighbor list has an advantage over CNA in that it allows identification of plastically-deformed atoms at the surface as well as atoms that have been displaced a complete lattice constant in the bulk. Fig. 5.6 shows that the bent surface also produces plastic rearrangements, even though no significant effect is observed on the

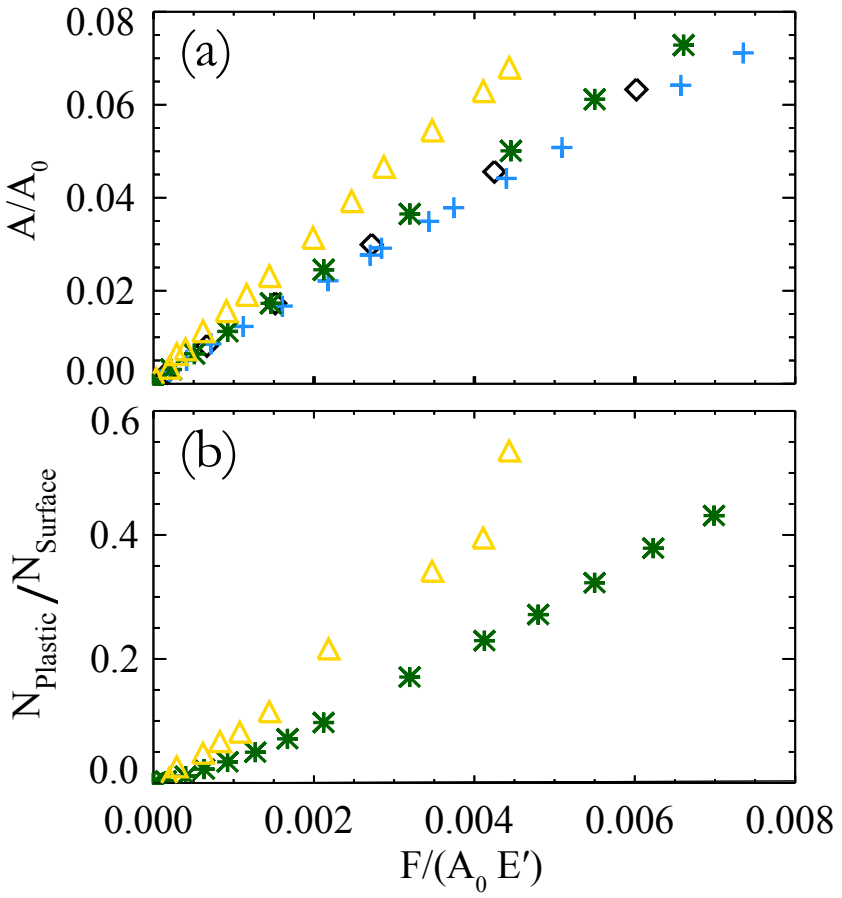

Figure 5.6: Shown is the load dependence of (a) the fraction of surface atoms in contact and (b) the measure of the plasticity based on changes to the list of neighboring atoms. Surfaces are elastic bent (black diamonds), elastic stepped (blue crosses), LJ bent (green asterix), and LJ stepped (yellow diamonds). The surfaces were formed from a continuum template with $h'_{rms} = 0.3$ and $L_{min} = 6\sigma$.

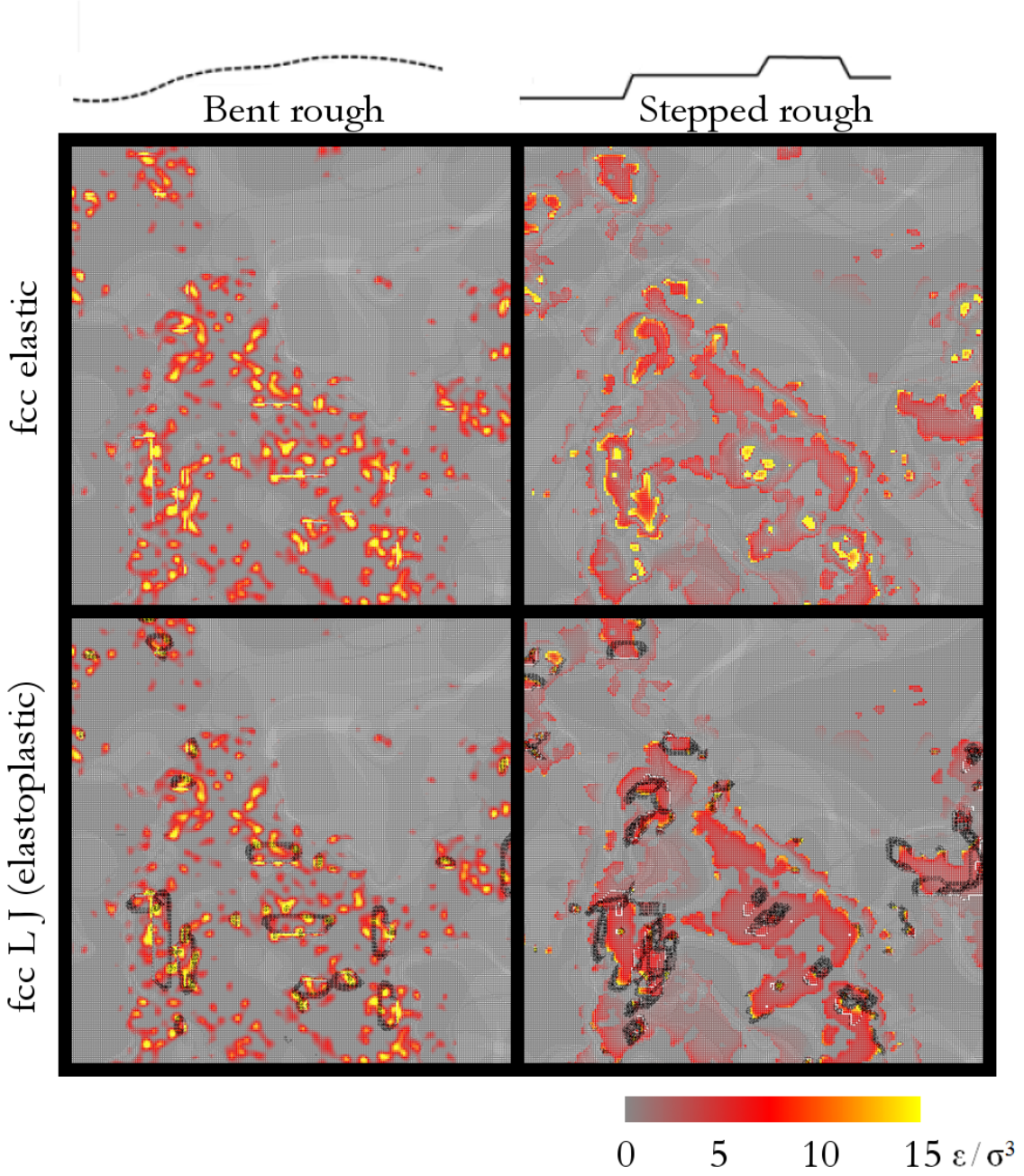

Figure 5.7: The spatial distribution of normal pressure in an $L/2 \times L/2$ region of a rough contact at $F/A_0E' \approx 4.7 \cdot 10^{-3}$. The normal force on atoms on the flat substrate is indicated by color. Atomic steps alter the pressure on small scales, producing an imprint of some of the plateaus and step edges in the pressure field. Plasticity occurs in the lower images, where there are LJ interactions in the substrate. The locations are marked in black where a subsurface atom left an fcc environment as determined by CNA. Note the increased plasticity near step edges in the lower right. The continuum template had $h'_{rms} = 0.15$, $L_{min} = 6\sigma$, $H = 0.5$, $L = 1024a_0$.

contact area. Bent surfaces with slope $h'_{rms} = 0.15$ similarly showed the onset of plasticity at $F/A_0E' \approx 0.001$. This is in line with the idea that even fairly flat surfaces at low loads inevitably produce plasticity. However, Fig. 5.6(a) (and later sections of this chapter) indicate that the many contact properties are unchanged from the purely elastic case.

Many of the plastically-deformed atoms contributing to the data in Fig. 5.6(b) are below the surface, as discussed in connection with Fig. 3.12. Another view is provided in Fig. 5.7. Shown are the same four cases as in Fig. 5.6(a) (bent and stepped, fcc elastic and fcc LJ). Step edges concentrate the stress because sharp features produce stress singularities in a linear elastic treatment. We see that the atoms at the base of a step are shadowed from contact. The four cases are at the same load. Inspection reveals that plastic yielding increases the contact area as the highest pressures regions give way and allow the surfaces to better conform. The locations of plasticity are plotted in black; these are primarily fcc {111} partial dislocation loops that nucleate from the surface where step edges have contacted.

While steps and plasticity change the distribution of pressure on small scales, the large wavelength structure is the same for all systems studied. To quantify this we show the Fourier spectrum of the normal pressure as a function of wavevector in Fig. 5.8. The dashed line shows the continuum prediction[76] that the Fourier amplitude $\tilde{p}(q)$ scales as $q^{(-1-H)/2}$ or the Fourier transform of the stress auto-correlation function $C(q)$ scales as q^{-1-H}. Atomic systems, whether bent or stepped, follow the continuum prediction for the spatial correlations at length scales above approximately L_{min}. The cross-correlation between bent and stepped pressure fields reveals that the large-wavelength components of the pressure field are nearly identical. However, at length scales between approximately L_{min} and a_0, the pressure is redistributed.

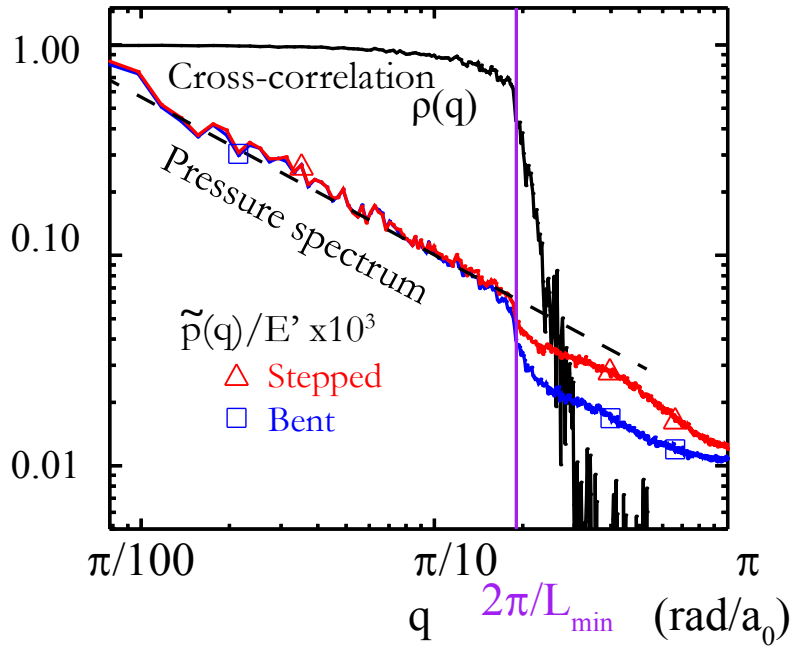

Figure 5.8: The amplitude of the Fourier transform of surface pressure, $\tilde{p}(q)$, produced by a bent surface (labeled with blue squares) and by the corresponding stepped surface (red triangles). The spectrum of surface pressure is defined as $\tilde{p}(q) = \langle|\tilde{p}_{2D}(\boldsymbol{q})|\rangle$ where the Fourier transform of the pressure is $\tilde{p}_{2D}(\boldsymbol{q}) = 1/L^2 \int d\boldsymbol{x}\ \ p(\boldsymbol{x}) \exp(-i\boldsymbol{q}\cdot\boldsymbol{x})$. Here $\langle \dots \rangle$ indicates averaging over all wavevectors $\boldsymbol{q}$ that have magnitude q and $|\dots|$ indicates the magnitude. The two spectra $\tilde{p}(q)$ have been normalized by contact modulus E', then multiplied by 1000 to lie on the same axes as the cross-correlation, ρ (solid black). The cross correlation (or squared normalized cross correlation) is defined as $\rho(q) \equiv |\langle p_1^*(\boldsymbol{q}) p_2(\boldsymbol{q})\rangle|^2 / (\langle \tilde{p}_1^*(\boldsymbol{q})\tilde{p}_1(\boldsymbol{q})\rangle \langle \tilde{p}_2^*(\boldsymbol{q})\tilde{p}_2(\boldsymbol{q})\rangle)$ where $\tilde{p}_1(\boldsymbol{q})$ and $\tilde{p}_2(\boldsymbol{q})$ denote the pressure for stepped and bent surface respectively and $*$ denotes complex conjugate. At low q, the pressure of the stepped and the bent surface have nearly identical spectra. Not only the amplitude, but the phases of the Fourier spectra are matched, as indicated by the normalized cross-correlation being near unity. The autocorrelation function, $C(q)$, follows the scaling $C(q) = |\tilde{p}^*(q)\tilde{p}(q)| \sim q^{-H-1}$ found in Ref. 76 for continuum surfaces (dashed black line). At large q the pressure fields differ for bent and stepped surfaces. The magnitude of the stepped-surface pressure is slightly increased at high q relative to the pressure of the bent surface. The distribution of the high-q pressure is entirely uncorrelated for bent and stepped, as evidenced by the cross-correlation dropping more than two orders of magnitude. This shows that the small scales of the surface pressure get redistributed by the stepped geometry. Shown is a case with elastic substrate, H=0.5, $L_{min} = 5.9\sigma$, $1024a_0 \times 1024a$, $h'_{rms} = 0.3$.

5.3.3 Local pressure probability distributions

Sec. 5.3.2 showed that the spatial distribution of pressure at long wavelengths follows continuum predictions, but that it is different at small scales. The distribution of local pressure values is plotted in Fig. 5.9. Pressure is computed here as z-force on elastic substrate atoms divided by a_0^2. Using the rigid block atoms produces similar results. Dividing by the mean pressure in the contact, $\langle p \rangle$, allows results for different normal loads to be compared. With this normalization all pressure distributions are found to be insensitive to load within the range investigated, between 2%-20% fractional contact area. The unnormalized distribution of pressure $P(p)$ can be recovered using $\langle p \rangle = F/A = \kappa^{-1} E' h'_{rms}$ and the values of κ in Fig. 5.13.

The theory of Persson predicts a universal form[7,48] for $P(p/\langle p \rangle)$ at low loads where contact area is proportional to load. The proportionality appears to hold for all surfaces investigated here and Fig. 5.9(a) shows data at typical loads within this regime. Results for the hard-wall elastic case with large L_{min} are closest to Persson's prediction of a Gaussian distribution at large $p/\langle p \rangle$. The other results for elastic surfaces are quite similar to each other and appear closer to the exponential distribution found in continuum simulations of elastic contact.[7,77] Note that the stepped surfaces are closest to the exponential form while bent surface results decay slightly more rapidly in the tail of the distribution. The longer tail for stepped elastic surfaces may reflect the pressure concentration near step edges.

For all cases, introducing plasticity causes a reduction in the tail of the distribution at high pressures. It is natural that high local pressures are likely to initiate plastic deformation and reduce the local pressure. Similar changes in $P(p/\langle p \rangle)$ were seen in continuum simulations of plastic contact.[116] The mean pressure $\langle p \rangle$ increases with rms slope and this leads to more plastic deformation and a greater suppression of the tail at large $p/\langle p \rangle$. Stepped surfaces also lead to higher local pressures and a greater suppression of the high

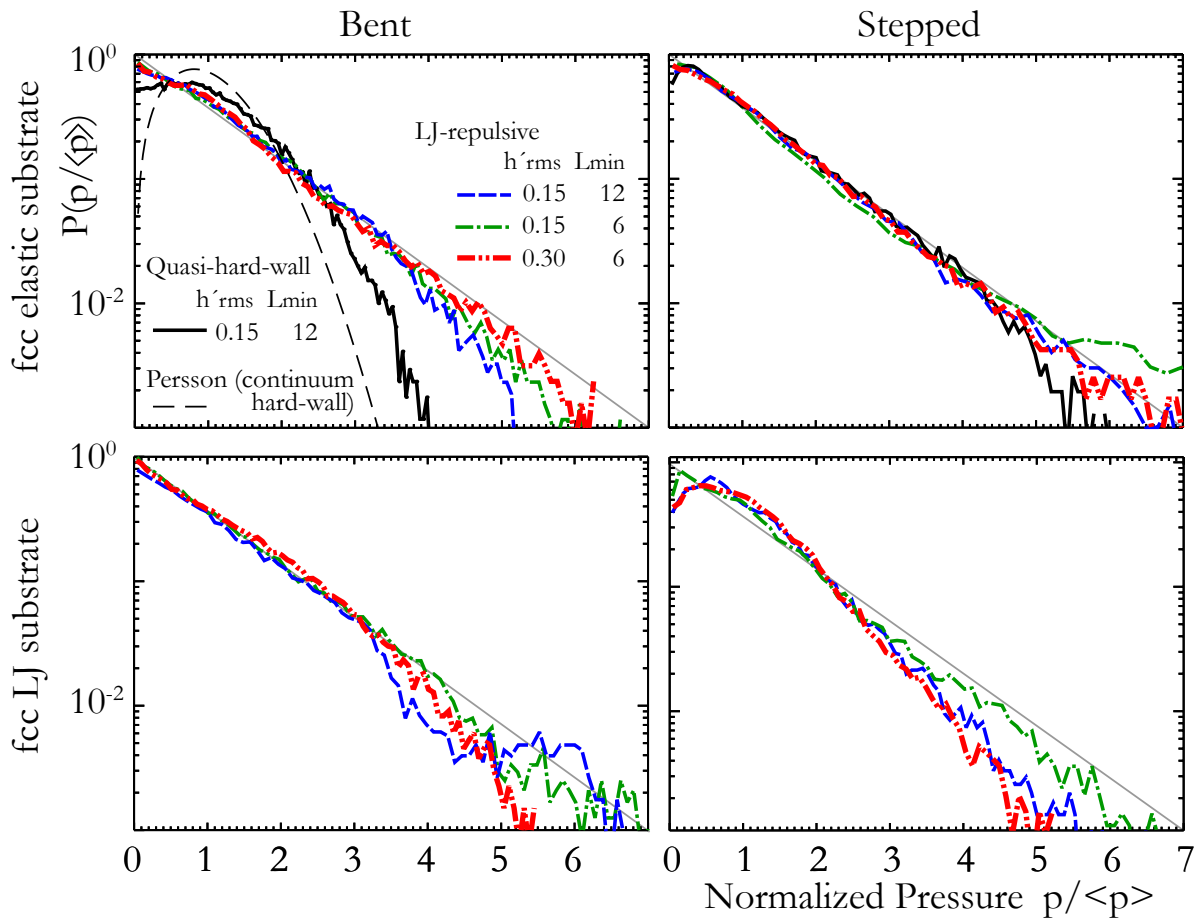

Figure 5.9: The probability distribution of normal pressure is plotted. Pressure has been normalized by the mean pressure in the contact, $\langle p \rangle = F/A$. Data in solid black in the top left are from an elastic, bent, quasi-hard-wall system that is the closest of these cases to a continuum description. Other curves represent characteristic variations of the parameters of Table 1. The universal distribution[7] from Persson theory[41,48,134] is shown as a thin dashed line. A grey diagonal guide line follows $P(p/\langle p \rangle) = exp(-p/\langle p \rangle)$. For elastic substrates (top row), the pressure is fairly well-described with a single exponential form over a large range. For LJ substrates (bottom row), the deviations at high pressures are related to anharmonic interactions and plasticity.

pressure tail. More pressure probability distributions for systems with plasticity are given in the appendix of this chapter.

5.3.4 Definitions of rms slope

A main result of this chapter is that the continuum treatment describes many qualitative aspects of contact of atomic systems, especially at large scales. Even at small scales, trends in the atomic simulation continue to follow the continuum-level trends but with different prefactors. It is therefore useful to connect with the continuum descriptions by mapping to continuum quantities (such as h'_{rms}) from the atomic systems.

For the bent fcc 100 surface, it is natural to define rms slope from a square grid of heights.

$$h'_{rms} \equiv \sqrt{\langle |\nabla h|^2 \rangle} \rightarrow \sqrt{\frac{1}{N_{sites}} \sum_{i,j} \frac{(h_{i+1,j} - h_{i,j})^2}{dx^2} + \frac{(h_{i,j+1} - h_{i,j})^2}{dx^2}}. \tag{5.4}$$

Here h_{ij} is the height of the grid site indexed i, j and the grid is aligned along the [100] and [010] directions. This matches the continuum definition for continuous surfaces in the limit of smooth height and small dx. The value of h'_{rms} for the bent surface matches the value for the original continuum template.

For the stepped surface of the ideal fcc 100 lattice, the distance between neighboring sites on the square grid is set to $dx = a_0/\sqrt{2}$, since successive (001) atomic planes of the fcc crystal are offset laterally in the [100] direction by that amount. The height $h_{i,j}$ is taken to be the height of the highest atom at that site unless all four neighboring atoms in the atomic plane above are present, in which case the lowest of those four neighbor heights is used. For the stepped surfaces, this definition nicely results in a surface h_{ij} of flat terraces and steps (as shown in the inset of Fig. 5.11).

Recall that the surface property κ is the prefactor in the proportionality between load and contact area for a given surface. From its definition in Eq. 5.1, it may be calculated

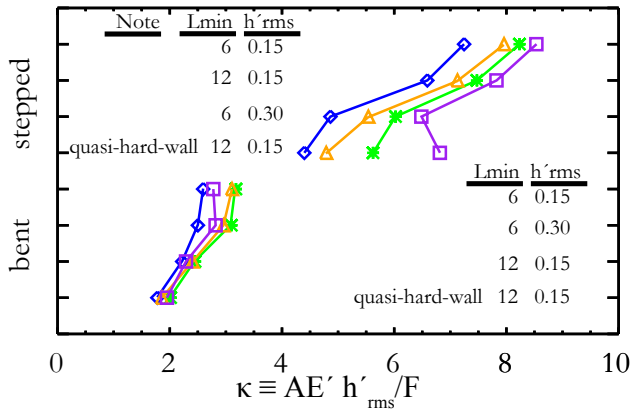

Figure 5.10: Values of κ for the indicated surfaces using Eq. 5.4 to calculate h'_{rms}. All systems are elastic. Symbols indicate different definitions of contact area as defined in the text: crosses and diamonds correspond to the number of atoms that experience a repulsive force on the substrate or rigid surface respectively; triangles and squares correspond to the exposed projected area analysis for substrate and rigid surfaces respectively.

from the simulations as $\kappa \equiv AE'h'_{rms}/F$. Fig. 5.10 shows that if Eq. 5.4 is used to define h'_{rms}, κ depends sensitively on the presence of steps and on the roughness of stepped surfaces. This is in contrast to continuum studies of a variety of bent surfaces based on real rough surface topographies and randomly-generated rough surfaces (*c.f.* Refs. 7, 45, 77) where κ always remained between 1.5 and 3.0. Recall that Fig. 5.6(b) also showed that the ratio of area to load changed less than 50% for atomic systems when the same surface was used to generate bent or stepped surfaces. As we now show, much of the deviation shown in Fig. 5.10 comes from the fact that Eq. 5.4 gives dramatically higher slopes for stepped than for bent surfaces.

Fig. 5.11 compares values of h'_{rms} from Eq. 5.4 for bent and stepped surfaces obtained from the same $h(\boldsymbol{x})$. For all cases the value for the bent surface is close to 2/3 times the square of the slope for the stepped surface. Since the slopes are less than 1.0, h'_{rms} is much larger for stepped surfaces. This scaling can be explained by rewriting the

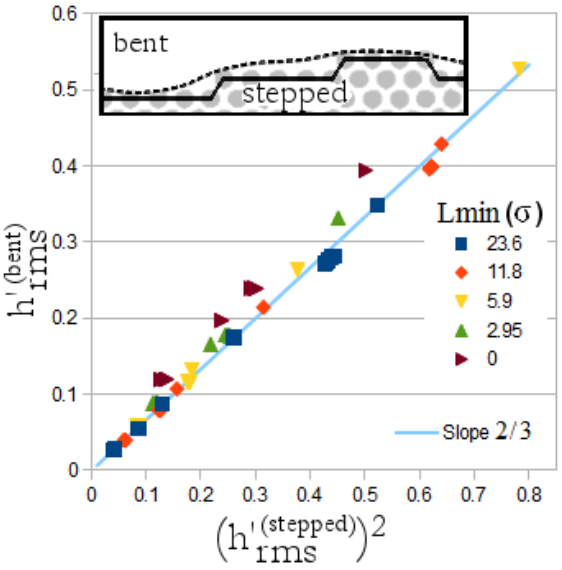

Figure 5.11: The rms slope of bent surfaces ($h'^{(bent)}_{rms}$) is plotted against the rms slope *squared* of their corresponding stepped surfaces ($h'^{(stepped)}_{rms}$). The discrete definition of rms slope is given by Eq. 5.4. Data points are several random realizations of system size $L = 512\sigma$ with $L_{max} = L$. The data show that $h'^{(stepped)}_{rms}$ can be considerably larger than $h'^{(bent)}_{rms}$. The figure also implies that, given only a stepped surface, the rms slope of the corresponding bent surface may be approximately determined. Symbols indicate different values of L_{min}; small values of L_{min} that approach the atomic length, σ, produce larger deviation from the line with slope 2/3.

sum in Eq. 5.4 as a sum over edges *between* sites of the square grid that are associated with each term. Squaring both sides of Eq. 5.4 and writing the sum as a sum over all grid edges (instead of grid sites), we have

$$(h'_{rms})^2 \to \frac{1}{N_{edges}} \sum_i \left(\frac{\Delta_z^i}{dx} \right)^2 \tag{5.5}$$

where Δ_z^i is the change in height of the grid edge indexed i. Consider the case of small slope that applies for our results. For the bent surface, the edge slope Δ_z/dx takes on real values near h'_{rms} of the cutting surface. For the stepped surface, the edge slope is almost always 0, except occasionally when it is $(a_0/\sqrt{2})/dx$. Since the surfaces follow the same initial $h(\boldsymbol{x})$, the sums of Δ_z over long distances are always within $a_0/\sqrt{2}$, but the sum of the *squares* of Δ_z will be quite different.

For the stepped surface the nonzero contributions are from edges where $h(\boldsymbol{x})$ crosses a lattice plane. If the surface height were doubled, the number of crossings would double and Eq. 5.5 would also double. For the bent surface Eq. 5.5 quadruples because all values of Δ_z/dx double. Therefore $(h'^{(stepped)}_{rms})^2 \propto (h'^{(bent)}_{rms})$ where Fig. 5.11 gives the proportionality constant as 2/3. The different scaling means that h'_{rms} of the stepped surface can be dramatically large compared to h'_{rms} of the corresponding bent surface. As a result, the value of κ for stepped elastic surfaces is not a constant near 2.0 even though the contact area to load ratio is similar to the bent case.[1]

Since bent and stepped surfaces produce similar area, one way to treat stepped surfaces is to always use the rms slope of the bent surface in Eq. 5.1, even for stepped

[1]The statements about the scaling of h'_{rms} for bent *v.s.* stepped surfaces hold when the surface $h(\boldsymbol{x})$ is sufficiently large, randomly-rough, with L_{min} a few times larger than the atomic spacing, and a slope mostly smaller than the single-step slope, 1.0. Note that if the surface were very rough, $h(\boldsymbol{x})$ could cross multiple atomic planes within lateral distance dx. For the stepped surface, the edges would have slope magnitude of 3.0, 5.0, or more. In the limit that the quantized height is small compared to the changes of $h(\boldsymbol{x})$ over distance dx, the results converge to the continuum, bent surface result. In that case doubling the surface height doubles the slopes and $h_{rms} \sim h'_{rms}$.

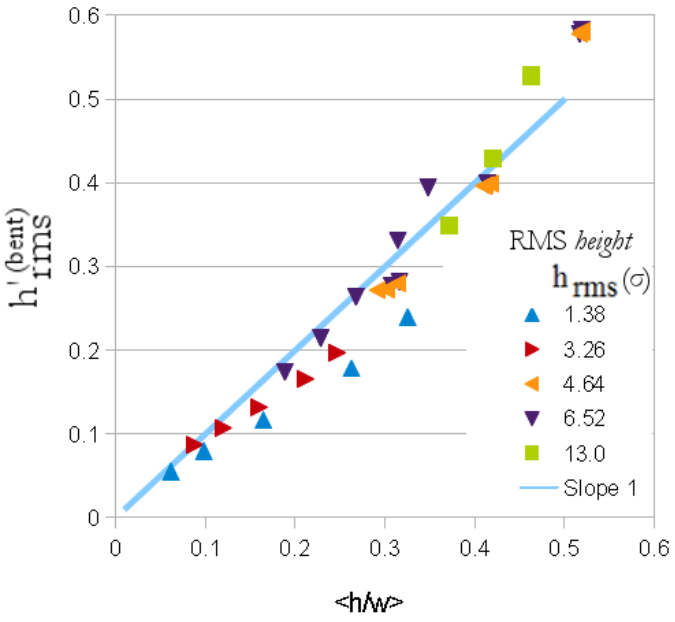

Figure 5.12: The rms slope of the bent surface ($h'^{(bent)}_{rms}$) is plotted against the mean ratio of step height to terrace width, $\langle h/w \rangle$, for the same dataset as in Fig. 5.11. $\langle h/w \rangle$ is a characteristic slope of the stepped surface. The step height is always the same in these simulations, $h = a_0/\sqrt{2}$. The value of $\langle h/w \rangle$ may be determined from an image showing surface steps and flat terraces, since w is simply the distance between steps along an arbitrary direction. The figure implies that the value of $h'^{(bent)}_{rms}$, which is useful in determining contact area as discussed in the text, may be approximately determined from the value of $\langle h/w \rangle$. Symbols indicate rms *height*, h_{rms}, which should be greater than 1.0 for these relations to hold.

surfaces. Explicitly,

$$\kappa \equiv AE' h_{rms}^{\prime(bent)}/F \tag{5.6}$$

where $h_{rms}^{\prime(bent)}$ is the same as the rms slope of the continuum template surface. The template surface is used in the calculation of κ everywhere in the chapter except for Fig. 5.10.

Fig. 5.11 provides one way to estimate $h_{rms}^{\prime(bent)}$ from the stepped surface: $h_{rms}^{\prime(bent)} \approx 2/3(h_{rms}^{\prime(stepped)})^2$. However h'_{rms} of the stepped surface is inconvenient to measure in experimental systems since it requires atomic resolution. An alternative is to identify the mean slope between steps by measuring the plateau width, w, and step height, h. This gives the slope h/w of an envelope surface that would enclose the surface step. By averaging over the surface to calculate the quantity $\langle h/w \rangle$, one approximates the slope of the original template surface, $h_{rms}^{\prime(bent)}$. Fig. 5.12 plots $\langle h/w \rangle$ of each stepped surface against the rms slope of the template $h_{rms}^{\prime(bent)}$. In the simulation w is measured by drawing a line in an arbitrary direction (since the roughness is isotropic) and recording the lateral distance w between each surface step encountered. This is another way to estimate $h_{rms}^{\prime(bent)}$ from the stepped surface for use in Eq. 5.6.

5.3.5 Definitions of contact area

We consider several definitions of contact area (indicated by symbol type in Fig. 5.13) to quantify the possible variations. The contact area definition discussed in section 5.3.2 is simply the number of atoms that experience a repulsive force times the lattice nearest neighbor distance squared, a_0^2. When the two solids differ in modulus or roughness, the estimate for contact area depends on which solid is considered. A peak on the rigid surface has positive curvature and a shorter length than the substrate that it contacts. For randomly rough solids, the rougher and more rigid solid has more positive curvature in contacting regions and therefore less contact area by these measures. This accounts for the small ($< 20\%$) increase in the contact area of the substrate atoms (diamonds) when compared to

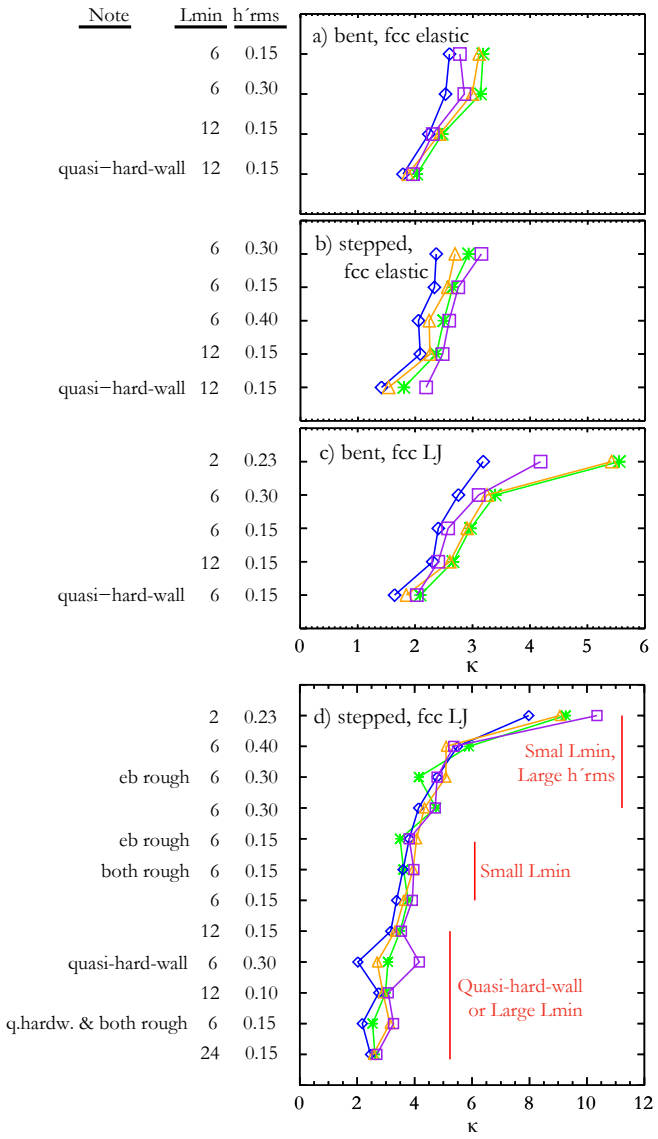

Figure 5.13: Atomic geometry leads to variability in κ, the dimensionless ratio of effective contact area and load. Different symbols correspond to different definitions of contact area which show a common trend. Triangles and squares correspond to the exposed projected area analysis for substrate and rigid surfaces respectively. Crosses and diamonds correspond to the number of atoms that experience a repulsive force on the substrate or rigid surface respectively. For stepped surfaces κ is defined here with $h_{rms}^{\prime bent}$ (which is approximately $\langle h/w \rangle$ as discussed in the text). Sub figures show results for (a) bent elastic (b) stepped elastic (c) bent Lennard-Jones (d) stepped Lennard-Jones. Data are ordered by κ, averaged over all four contact area definitions. L_{min} is in units of σ.

the rigid surface atoms (triangles) for the elastic surfaces (Fig. 5.13(a) and (b)).

The repulsive-force definition may be considered a special case of a separation-based definition of contact that uses $C(r_{cut})$ as discussed in Sec. 5.3.1. In general, contacting area in electrical contact, thermal contact, leakage of seals, and other applications would not necessarily align with the definition of onset of repulsive force. We therefore also consider the sensitivity to the separation cut off that defines contact. Fig. 5.3(b) and (c) showed that the sensitivity to the definition-of-contact range is low (*e.g.* $C(r_{cut}) \approx C(r_{cut} + 0.1\sigma)$). Moreover, the average gap between surfaces increases with L because the rms surface height rises. This means that $P(u)$ just outside of contact (*i.e.* at $u = r_{cut} + \sigma$) is lower in larger systems and $C(u)$ is even less sensitive to the definition of contact range. This provides evidence that separation-based definitions of contact area may be nearly uniquely defined in the thermodynamic limit.

A different measure of contact area is motivated by the idea that not all surface atoms contribute to the surface area equally. This occurs for example in the case of stepped surfaces or highly-plastically-deformed surfaces. Fig. 5.14 illustrates this in a simulation where both the upper and lower solid are stepped. Note that the atoms of the step edge partially eclipse the atoms of the next atomic plane in the lattice, so that they are not as exposed to the other solid. To account for this, we consider weighting each contacted atom by its projected area exposed to contact. If a test atom at (x, y) is translated in z towards the opposing surface, it will first contact an atom i if (x, y) is within atom i's exposed projected area. The exposed projected area (EPA) can be calculated during a simulation by creating a high-resolution ray-traced image of the surface, with atomic spheres of radii r_{cut} and colored if the atom carries a load. The fraction of colored pixels is the fractional contact area in the EPA definition. This definition ensures that the maximum contact area is L^2 even in highly plastically deformed systems, which is assumed in some continuum theories.

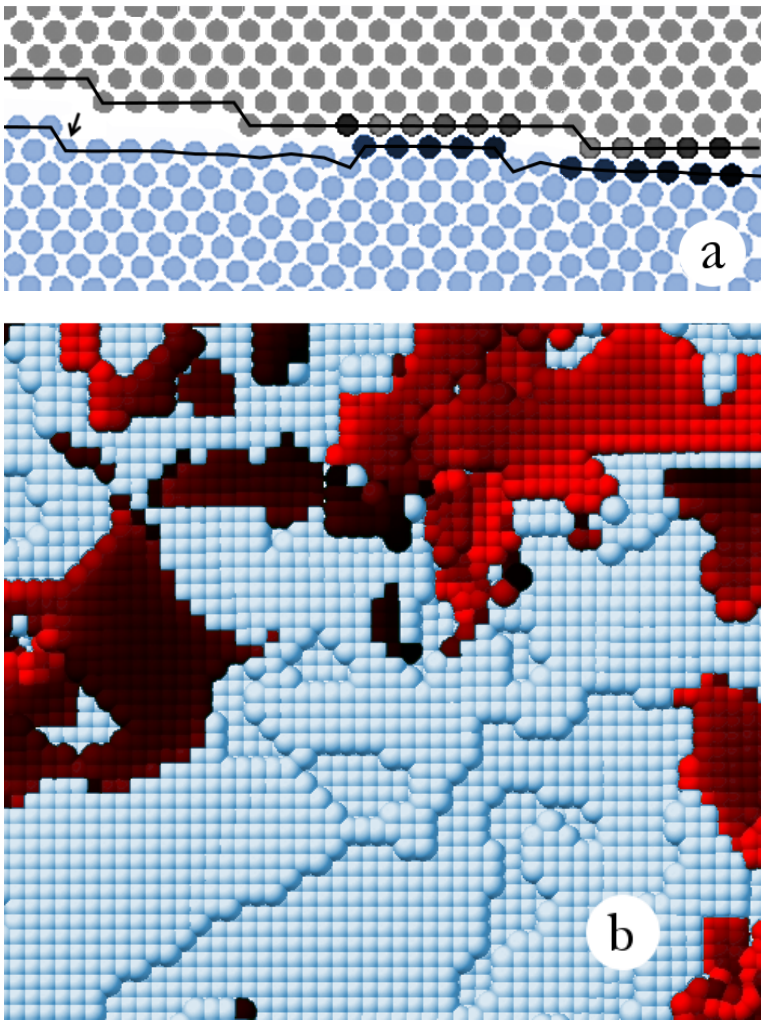

Figure 5.14: Small regions of contact between two surfaces, each with roughness parameters $h'_{rms} = 0.15$, $L_{min} = 6\sigma$, $H = 0.5$. (a) Atoms within a cross section plane of thickness $a_0/2$. A small arrow indicates an atom that is exposed, and may be considered a surface atom, but is partially eclipsed by the layer above. Especially high stresses deformed the lattices near step edges. (b) Image illustrating the EPA definition of fractional contact. The elastic substrate atoms are drawn as spheres with diameters of the interaction range, $r_{cut} = 2^{1/6}\sigma$. They are colored according to normal pressure, and the EPA fractional contact area is the fraction of colored pixels. Thus the EPA can never exceed the nominal contact area of the plane, A_0.

5.3.6 κ of atomic systems

Fig. 5.13 shows values of κ for atomic solids using Eq. 5.6, and comparing four definitions of contact area (indicated by symbol type). For elastic solids (Fig. 5.13(a) and (b)), κ is approximately constant despite large changes in the roughness parameters. κ for elastic solids remains within a range of approximately $1.5 - 3.0$. This is in contrast to the findings of a previous, two-dimensional study[126] that focused on higher slopes and found κ to have values of at least of order 10 for bent and stepped atomic surfaces. We do note a systematic increase in κ as L_{min} extends down to the atomic size and the greatest deviations from continuum theory are expected.

Fig. 5.13(c) and (d) show cases where plastic deformations occur. κ is only outside the range of elastic values for bent surfaces with $L_{min} = 2\sigma$ and stepped surfaces with $L_{min} = 2\sigma$ or $L_{min} = 6\sigma$ and $h'_{rms} > 0.3$. While sufficiently smooth surfaces have κ similar to the elastic case, rougher surfaces produce more contact area. This is because surfaces with higher h'_{rms} have higher mean pressure according to Eq. 5.1, which causes additional plastic deformation and increases κ. Continuum modeling of elasto-plastic contact[116] indicates that increases in κ of order 2.0 are expected from surfaces of $h'_{rms} \approx 0.2$ in this LJ system ($\sigma_y/E' \approx 0.02$). This is in line with the results of Fig. 5.13(c). However, the modeling in this chapter also indicates that small L_{min} is more effective at nucleating plasticity than larger L_{min}, so that the largest κ in Fig. 5.13(c) does not occur in the surface with the largest h'_{rms}. In Fig. 5.13(d) we observe that steps always increase plasticity and contact area in the LJ system above that seen for the corresponding bent surfaces. This reflects the effectiveness of the sharp changes in surface pressure under steps at nucleating plasticity. To show the generality of the simulations we have also included results for systems with roughness on both surfaces in Fig. 5.13(d). These have the same reported roughness on both surfaces, and the rms slope of the two is summed in quadrature in the calculation of

κ. The results are consistent with those where just a single surface is rough.

Fig. 5.13 also shows that for all cases the contacted EPA (squares and crosses) tracks the number of atoms that experience a repulsive force (diamonds and triangles). For elastic surfaces, the most significant deviations between the two definitions arise for stepped surfaces, since atoms at step edges are often contacted and receive large weighting in the EPA definition. The deviations become especially pronounced when r_{cut} is large (the quasi-hard-wall case), since the weighting of edge atoms increases with the interaction range. Since the EPA definition mostly follows the more standard definition based on repulsive force, while having useful properties mentioned in Sec. 5.3.5, it may be a useful definition of contact area in future studies.

5.4 Conclusion

A variety of questions arise regarding the practical application of continuum rough contact theory to atomic systems, and the simulations of this chapter provide some clarification. In general, applying continuum theory requires finding the appropriate mappings between the atomistic description and the continuum theory and also finding when those mappings break down. One specific example is the question about how to associate atomic quantities with contact area and surface slope. For the former, this chapter showed that effective definitions of contact and contact area could be identified in the atomic systems considered here. For the latter, the surface slope h'_{rms} had a natural definition for bent surfaces, but for stepped surfaces it was shown that the slope $\langle h/w \rangle$ should be used instead of the local slopes h'_{rms}, since $\langle h/w \rangle$ approximates the slope of the bent surface while the sharp steps make h'_{rms} anomalously large. Fig. 5.13 showed that using this mapping, the continuum elastic prediction of $\kappa \approx 2$ held when the roughness was not too great but began to breakdown for very rough surfaces that deform plastically.

As another example of practical application, consider the question of whether

optical microscopy provides sufficient information to determine contact properties between two randomly rough surfaces. Optical microscopy does not resolve atomic scales, but does capture larger-scale topography. For all simulations in this chapter, Eq. 5.2 holds with $\gamma \approx 0.5$ so that predicting the normal contact stiffness requires knowing h_{rms} only. The value of h_{rms} is dominated by the large-scale topography[135] for any Hurst exponent $0 < H < 1$ indicating that a low-resolution topography can be sufficient to determine normal contact stiffness.

On the other hand, optical microscopy would often be insufficient to determine the true intimate contact area. That is because, as this chapter finds, contact area of atomistic elastic contact follows Eq. 5.6 with an approximately constant κ – even when roughness extends down to atomic scales, $L_{min} = 6\sigma$. Thus contact area is approximately inversely proportional to the value of the bent surface slope h'_{rms}. The value of h'_{rms} is dominated by the smallest-scale roughness[135] for a bent surface of any Hurst exponent $0 < H < 1$. Any unresolved roughness would therefore reduce the contact area below that predicted from a low resolution image.

Atomically-stepped surfaces contribute to the roughness in a different way than does the smoothly-varying template surface $h(\boldsymbol{x})$. This is seen by the fact that κ varied significantly for elastic contacts when the microscopic rms slope of stepped surfaces was used in the calculation of κ. This is in contrast with the result for bent atomic surfaces as well as previous work on continuum surfaces[7,41,45] and indicates that the power spectrum of the surface did not alone determine contact area for stepped surfaces. We found that the effect of steps could be approximately accounted for in Eq. 5.1 by replacing the true microscopic surface slope with the slope averaged over a plateau h/w, and that $\langle h/w \rangle$ had approximately the same value as the rms slope of the bent surface h'_{rms}. This may serve as a useful example when predicting contact area of micro-structured surfaces or other surfaces with important phase correlations in the roughness.

This chapter also showed that atomic steps have significant consequences for the surface forces in elastic contact, redistributing the surface pressure spatially. Typical surfaces produce somewhat exponential-shaped probability distributions of pressure, and atomic steps produced small changes to the high-pressure tail. The changes due to steps can be important to electrical, tribological, and chemical surface properties. An example is the increased plasticity observed for stepped surfaces compared to bent surfaces for fcc LJ lattices. Atomic steps redistribute surface pressure at small scales, leading to peak pressures at step edges which are adjacent to regions of low pressure. This redistribution of pressure increases plastic yielding of the crystal and increases contact area. A bent surface, with the same continuum template but lacking the steps, was seen to produce only 50% of the contact area. These show examples in which elastic continuum predictions should not be directly applied to atomic-scale systems without knowledge of the atomic scale geometrical features.

5.5 Ch 5. Appendix: Pressure distributions of cases of Fig. 5.12

In many figures in the chapter we showed only a small subset of the simulations. As mentioned in the text, we tested other combinations of surface roughness parameters to ensure robustness of the conclusions. The values of κ for some of those surfaces are given in Fig. 5.13. In this appendix we also provide the results for the probability distribution of surface pressure for those cases. A wide variety of modifications are represented in Fig. 5.15, showing the robust general pressure distribution shape, while still showing potentially significant deviations.

We also note a few observations about the shape of the pressure distribution changing in response to the surface geometry. In Sec. 5.3.3, the bottom right of Fig. 5.9 suggests that increasing either L_{min} or h'_{rms} causes a change in the simple exponential shape stepped fcc-LJ surfaces. This may be due to leaving a regime of essentially elastic contact and pro-

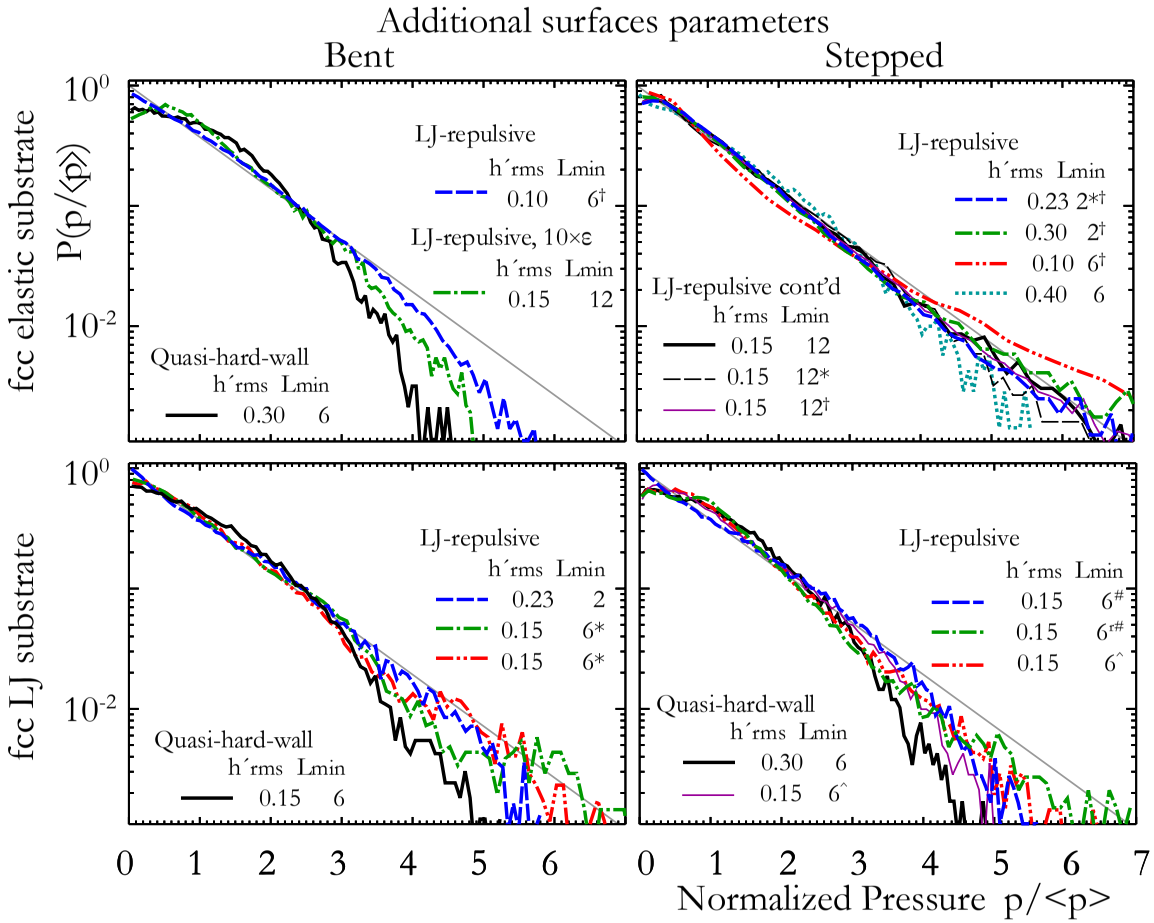

Figure 5.15: The pressure distribution shape remains similar across the wide variety of additional parameters simulated as shown. Cases with $H = 0.8$ are denoted by * and $L_{max} = 2048a_0$ by †. Cases with rigid-flat and deformable-rough are denoted by ^{r}, and cases with the labeled roughness copied onto both surfaces are denoted by $^\wedge$.

ducing a regime with additional plasticity. This is explored in more detail in Fig. 5.16. Distributions with a longer tail are plotted above and distributions with a shorter tail are plotted below. Nearly all simulations are shown to follow one of two shapes. Fig 5.16(a) follows the often-seen exponential shape from elastic contact. These are the lower h'_{rms} and lower L_{min} cases that exhibit less pressure concentration on the step edges. Fig 5.16(b) may constitute an elasto-plastic regime of stepped surfaces, due to increased pressure concentrations from step edges. In contrast, no clear change in the distribution shape was seen for bent surfaces for the roughness parameters simulated.

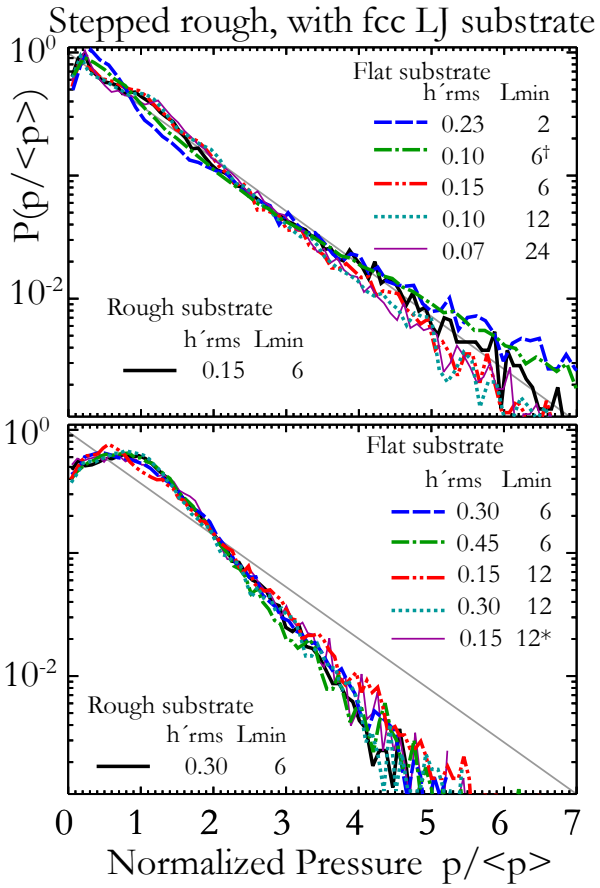

Figure 5.16: Stepped surfaces can be grouped according to the shape of the pressure distribution $P(p/\langle p\rangle)$, possibly providing an indication about whether the contact properties are elastic or elasto-plastic. Simulations with large h'_{rms} or L_{min} show a peak near the mean pressure $p = \langle p\rangle$ and a shorter tail. Simulations with little plastic deformation have a pressure distribution with a longer exponential tail. The case marked with symbol "*" has $H = 0.8$ rather than $H = 0.5$ and the case marked with symbol "†" has $L = L_{max} = 2048a_0$ rather than $1024a_0$. The data also show that the results are unchanged by allowing the rough solid to deform, while the flat solid is held rigid.

Chapter 6

Elasticity limits structural superlubricity in large contacts

Friction is omnipresent but large gaps remain in our understanding of its atomic origins and our ability to control it to reduce energy loss or improve braking. One fascinating phenomenon observed at nanometer scales is structural lubricity, a state of ultra-low friction that results from the systematic cancellation of forces across an interface between solids that have no common periodicity.[34,136,137] Experiments have observed this cancellation between identical crystalline surfaces that are rotated to become incommensurate,[12,37,136] different crystalline surfaces[16,138] and between amorphous and crystalline surfaces.[16] Superlubricity has been suggested to underlie the mechanism of solid lubrication by plates of graphite and MoS_2,[137,139] and to have the potential to lower friction in a range of applications.

Theoretical treatments of superlubricity have usually considered the limit of rigid solids illustrated in Fig. 6.1(a,c). If surfaces share no common period, then atoms sample all relative positions with equal probability in the thermodynamic limit. The resulting energy is translationally invariant and there is no friction. For finite systems the cancellation is incomplete. The frictional stress (force per unit area) scales as a power of the contact radius a for incommensurate and amorphous surfaces, approaching zero as a increases.[10,16,140]

The elastic compliance of the surfaces has the potential to dramatically alter superlubricity because atoms move to preferentially sample low energy configurations (Fig. 6.1(b,d)). If elasticity leads to multiple metastable states, there can be finite friction.[30,141,142] The one-dimensional case corresponds to the well-studied Frenkel-Kontorova chain model.[30]

The infinite chain shows a non-analytic transition from zero to finite friction with increasing compliance, but finite chains have friction associated with dislocations (solitons) at chain ends.[30] Several groups have investigated the two dimensional case of a compliant monolayer on a rigid substrate,[143–146] but there have been comparatively few studies of crystalline frictional contacts where compliant three-dimensional objects interact at a two dimensional interface. It has been suggested that dislocations at the interface could lead to friction,[147,148] but Müser found that incommensurate interfaces became unstable to interdiffusion before the friction force become finite.[149] Friction due to internal elasticity at incommensurate interfaces has only been observed for a very compliant system with just a few contacting atoms that could lock in multiple metastable states.[150]

In this chapter we study the scaling of friction with compliance and contact size for circular contacts between incommensurate or commensurate crystals. An efficient Green's function method allows us to vary the radius a from less than a nanometer to a fraction of a micrometer. The studies show that there is a transition as a exceeds the core width b_{core} of interfacial dislocations. For $a < b_{core}$ the frictional stress τ_{fric} is consistent with previous results for rigid surfaces, dropping to zero with increasing a for incommensurate surfaces and remaining constant for commensurate surfaces. For $a > b_{core}$ compliance leads to new behavior. At intermediate a/b_{core}, τ_{fric} is controlled by dislocation nucleation near the edge of the contact where there is diverging stress in continuum theory.[27] At large a/b_{core}, τ_{fric} is seen to saturate at a finite value that is related to the Peierls stress for dislocation motion. Just as for finite Frenkel-Kontorova chains, there is never true superlubricity with zero friction in finite contacts. However the Peierls stress drops exponentially to zero as b_{core} increases and the friction in large contacts may be extremely small.

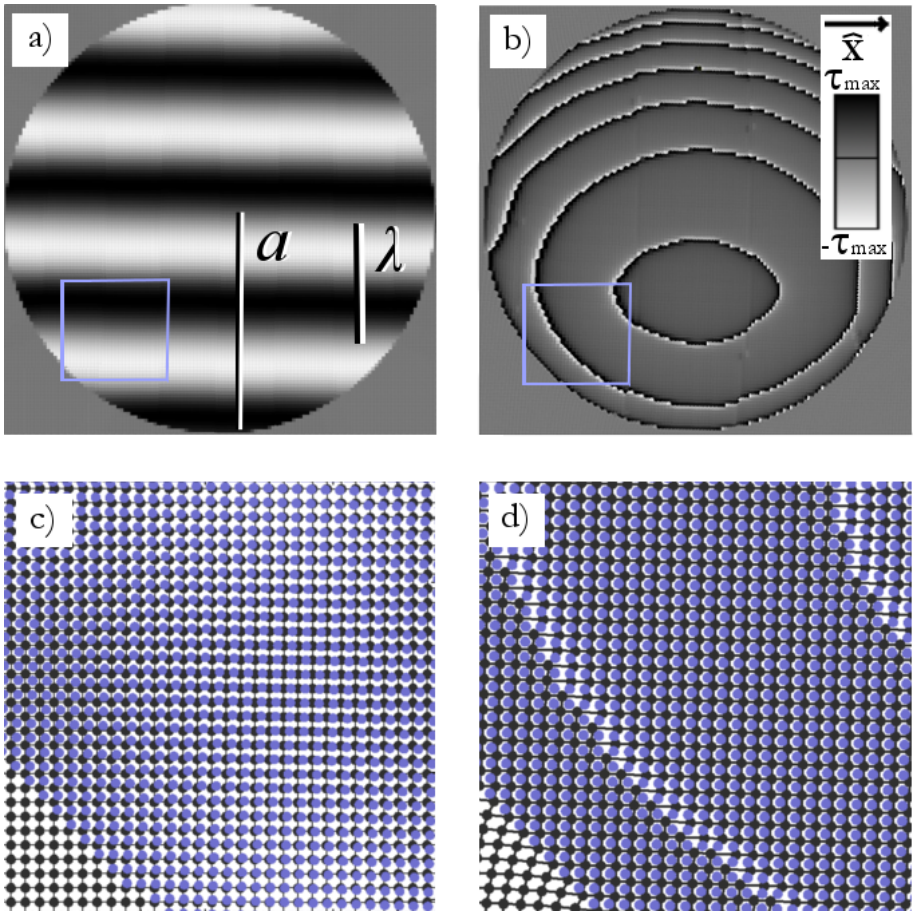

Figure 6.1: (a,b) Grey scale plot of traction in the sliding direction and (c,d) enlarged view of atomic positions (blue) and energy minima of the substrate potential (grey) for incommensurate crystals with $\theta = 0.03$radians, $\lambda \sim 33d$ and $a = 62d$. In (a,c) the substrate is effectively rigid, $G/\tau_{max} = 256$, and all atoms advance together. The traction forces alternate in sign and sum to nearly zero. In (b,d) the substrate is compliant, $G/\tau_{max} = 1$, and sliding occurs through the motion of dislocations between regions that have locked in registry. Movies are included in supplemental materials as *Fig6.1a.avi and Fig6.1b.avi.*

6.1 Computational model

We consider the simplified geometry of a circular disk interacting with a semi-infinite elastic substrate. This mimics the islands studied by Dietzel et al[16] or contact between a sphere and flat substrate. Separate simulations for the latter geometry exhibit the same behavior reported below. The disk is rigid and the substrate has shear modulus G and Poisson ratio ν. This case can be mapped to contact of two compliant objects in continuum theory.[20]

Atoms on both surfaces form a square lattice with nearest-neighbor spacing d, corresponding to (001) surfaces of fcc crystals. The nearest-neighbor direction of the substrate is rotated by an angle θ relative to that of the disk. At $\theta = 0$ the system is commensurate with all atoms in phase. Rotating the system out of alignment by an angle θ creates an incommensurate contact that is like a twist grain boundary (Fig. 6.1). Similar results were obtained with surfaces made incommensurate by changing the lattice constant.

The interaction of the substrate surface atoms with the rigid disk is represented by a simple sinusoidal force in the $x - y$ plane of the substrate like that used for the Frenkel-Kontorova chain and two dimensional Peierls-Nabarro model:[29,30]

$$\boldsymbol{f}(x, y) = \tau_{max} d^2 (\sin(2\pi x/d)\hat{\boldsymbol{x}} + \sin(2\pi y/d)\hat{\boldsymbol{y}}) \tag{6.1}$$

for $r < a$, where τ_{max} represents the maximum local frictional stress or traction. The competition between bulk deformation and interfacial slip can be characterized by a core width $b_{core} \equiv dG/\tau_{max}$. For all cases studied b_{core} equaled the distance from the center of an interfacial edge dislocation to the line where the stress drops to $\tau_{max}/2$.

The displacement of substrate atoms is calculated with a Green's function technique that describes the linear response of a semi-infinite substrate.[19,51,110] The results presented below are for the commonly studied case of an isotropic substrate with $\nu = 0.5$, but other interactions gave equivalent results.[151] The substrate is displaced quasi-statically

and the energy minimized after each step using LAMMPS.[81] The static friction is determined from the maximum force between the surfaces during sliding. Normalizing by contact area gives the macroscopic frictional stress, τ_{fric}. Results are shown for sliding at $\theta/2$ to the x axis, but other sliding directions give similar scaling.

6.2 Results

Figure 1 contrasts the behavior of rigid and compliant substrates for an incommensurate case of $\theta = 0.03$. For the stiff case, substrate atoms remain on an ideal rotated square lattice and atoms are equally likely to be above or between atoms of the disk. The force resisting sliding oscillates as the registry changes with a characteristic period $\lambda \sim d/\theta$ at small angles. The cancellation in forces for $a > \lambda$ leads to structural superlubricity.[34,136,137]

For rigid incommensurate lattices with circular contact area, the static friction stress has an upper bound that decreases as a power of a, $\tau_{fric} \sim \tau_{max}(a/d)^{-3/2}$ at large a.[10,16,140] Figure 6.2(a) shows the static friction stress of a contact with $\theta = 25^o$. When the shear modulus G is large, the friction follows the predicted rigid scaling shown by the dashed line. Elasticity is unimportant since $b_{core} = dG/\tau_{max}$ is much greater than a. Note that there are special radii where the cancellation of forces is nearly exact and the friction is anomalously small compared to the power law fit. To minimize fluctuations, these special radii are not included in Fig. 6.2(b). As an aside, it is worth providing a reminder that the friction force is smallest in small contacts since the friction stress falls more slowly than a^{-2}.

For the compliant case shown in Fig. 6.1(b,d), mis-registry becomes localized into dislocation cores. Between dislocations the surfaces lock together to effectively resist sliding. As has been observed in the simpler case of 1D systems[30] and suggested for 2D systems,[147,148] sliding occurs through dislocation motion along the interface rather than rigid translation of the entire surface. Contact produces an initial network of misfit dis-

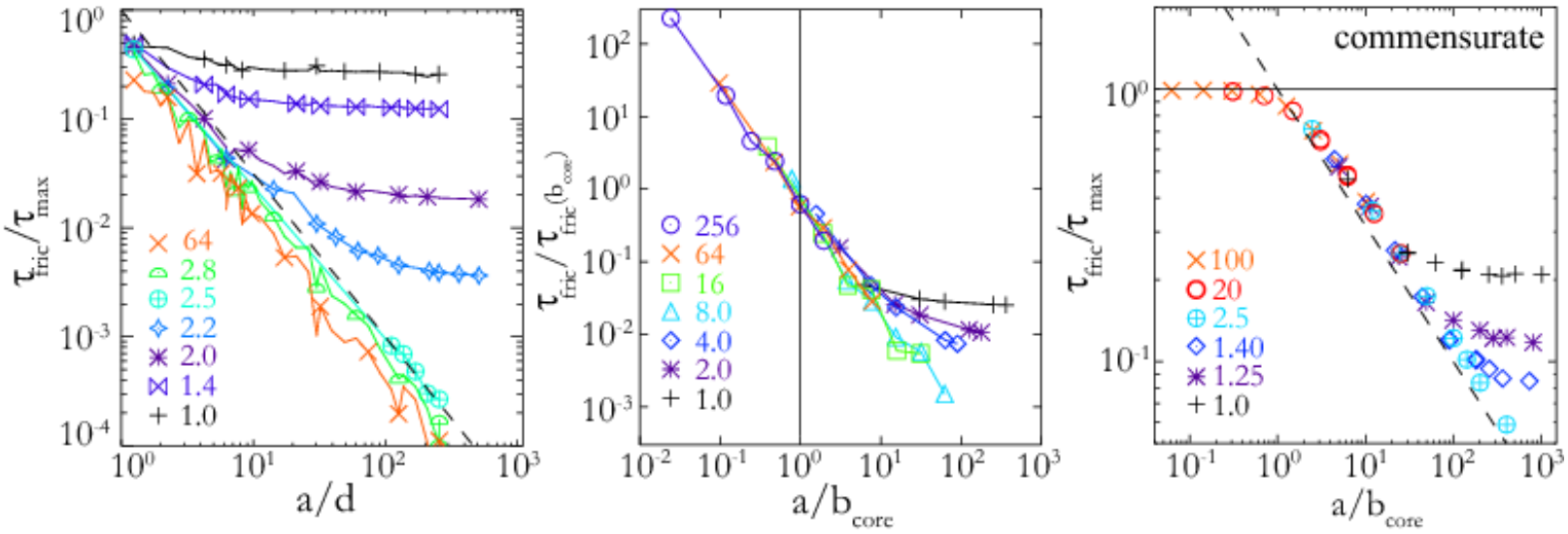

Figure 6.2: Static friction stress vs. contact radius for the values of b_{core}/d indicated by symbols in the legend. (a) For incommensurate contacts τ_{fric} decreases as $a^{-3/2}$ (dashed line) and then saturates at a plateau that decreases with increasing b_{core}. (b) Scaling by b_{core} and $\tau_{fric}(b_{core})$ shows that rigid scaling holds for $a < b_{core}$ and τ_{fric} saturates for $a \gg b_{core}$. The rotation angles are (a) 25° and (b) 3.4° to illustrate that similar behavior occurs for all incommensurate surfaces. (c) For commensurate ($\theta = 0°$) surfaces τ_{fric} is constant at $a < b_{core}$ and then drops as $a^{-1/2}$ to a plateau value that decreases with increasing b_{core}.

locations. In the case shown, there were three horizontal dislocations separated by λ at locations where the force changes sign in the rigid case. Sliding produces a nonuniform stress distribution with singularities near the edge of the contact[20] as discussed below. This causes the dislocations to curve as they move and nucleates new dislocations at the contact edge. Fig. 6.1(b) shows a snapshot from steady state sliding. As sliding continues, the dislocations move inwards towards the central ellipse and annihilate while new dislocations nucleate at the edge. The number of dislocations at the peak force corresponding to static friction, increases with a/b_{core}.

Figure 6.2(a) reveals how compliance affects the static friction. As G and b_{core} decrease, the friction deviates from the rigid scaling at smaller and smaller a. At large a the shear stress approaches a constant limiting value that decreases as b_{core} increases. It therefore becomes more difficult to reach saturation at large b_{core} and at sufficiently large b_{core} the stress continues with the rigid scaling for the accessible simulation sizes. Similar behavior is observed for all rotation angles that produce an incommensurate interface.

The importance of b_{core} is illustrated by the rescaled data for $\theta = 3.4^o$ in Fig. 6.2(b). The radius is normalized by b_{core} and the friction by the rigid prediction for $a = b_{core}$. For $a < b_{core}$ the stress exhibits the power law scaling predicted for rigid surfaces. For $a > b_{core}$, dislocations enter the contact and the interface deforms to lock into local registry. The friction is above the rigid prediction, dropping more slowly and then saturating at large a/b_{core}. Given our limited simulation size it is difficult to reach the asymptotic limit for $b_{core} > 5d$, but the arguments below suggest that the saturating value drops exponentially with increasing b_{core}.

Previous work on interfacial dislocations in circular contacts between 3D solids[27–29] has focused on the commensurate case, $\theta = 0$. Results for this special case are shown in Fig. 6.2(c). Because all atoms are in phase in the rigid limit, the shear stress is independent of a. As a becomes larger than b_{core}, the friction drops below the rigid limit. The initial decrease

scales as $a^{-1/2}$. As shown in a one-dimensional model by Hurtado and Kim,[27] this can be understood from the fact that continuum theory predicts that a uniform displacement in the contact a produces a singular shear stress at the edge of the contact. The stress within b_{core} of the edge scales as $(a/b_{core})^{1/2}$ times the stress in the center. When this edge stress reaches τ_{max}, a dislocation can nucleate at the circumference and propagate across the interface, allowing the whole contact to advance by d. Gao has observed this regime[29] in two dimensional simulations up to $a/b_{core} \sim 50$ and Fig. 6.2(c) extends the scaling regime by more than an order of magnitude.

At very large a/b_{core}, many dislocations are stable in the contact. In this limit one expects[28] that the shear stress approaches the Peierls stress for dislocation motion $\tau_{Peierls}$. Our simulations access this regime for the first time, showing a clear saturation at a force that decreases with increasing b_{core}.

The results shown in Fig. 6.2 suggest that for both commensurate and incommensurate systems the shear stress in large contacts approaches the Peierls stress for dislocation motion. As shown in Fig. 6.1, dislocations make a loop and thus change from edge character at the front and back, to screw dislocations at the sides. We performed a set of simulations with periodic boundary conditions to determine $\tau_{Peierls}$. The same compliant substrate was used but the rigid periodic potential was stretched or skewed to impose a single dislocation per unit cell at the desired orientation. The stress on the top surface was then increased to determine the Peierls stress at which the dislocation moved. As predicted from continuum theory,[24,25] $\tau_{Peierls}/\tau_{max} \propto \exp(-b_{core}/d) = \exp(-G/\tau_{max})$. The solid line in Fig. 6.3 shows a fit to data for an edge dislocation perpendicular to the sliding direction. Stresses for other orientations were both larger and smaller, but also show exponential scaling at large core widths.

Also shown in Fig. 6.3 are the saturation friction stresses for a wide range of θ and b_{core}. A striking conclusion is that similar physics determines the saturating stress in

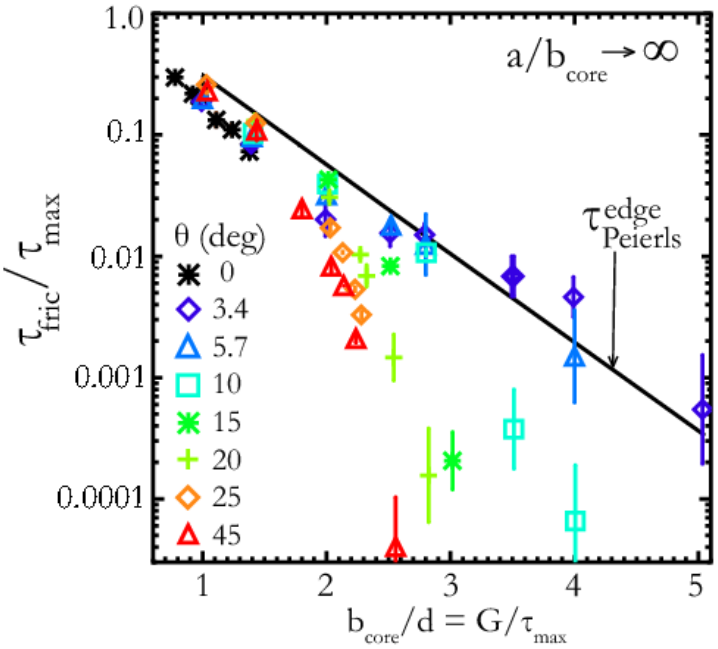

Figure 6.3: Plateau stress for $a/b_{core} \to \infty$ at the indicated rotation angles (symbols) and the Peierls stress for edge dislocations in a periodic system (solid line). There are significant errorbars at large b_{core} where it is difficult to reach full saturation. The top of each errorbar represents an upper bound corresponding to τ_{fric} at the largest a studied (512 to 1024d). The bottom was estimated by linearly extrapolating the tail of log-log plots like Fig. 6.2 to ten times the largest a studied.

both commensurate and incommensurate contacts. In the limit of small θ or small b_{core} commensurate and incommensurate surfaces have similar shear stresses that scale with the Peierls stress for a single edge dislocation. At larger θ and b_{core}, τ_{fric} is depressed and results for each θ seem to decay with a more rapid exponential. In this limit the spacing between intrinsic dislocations $\lambda = d/\theta$ is smaller than b_{core}. Interactions between nearby dislocations are known to reduce the effective Peierls stress. Independent simulations of periodic systems with twist grain boundaries showed similar stresses as the large-size-limit stresses in Fig. 6.3. These simulations used special angles where the surfaces retain the same lattice constant. The results are very similar to those in Fig. 6.3, except at nearly commensurate cases such as $\tan\theta = 3/4$.

Given the strong dependence of Peierls stress on b_{core} it is interesting to consider typical values for real materials. For contact between two identical solids, Eq. 6.1 should give a simple model for interactions between lattice planes in the bulk as well as at the interface. In this case, $G/\tau_{max} \sim 2\pi h/d$ where h is the spacing between lattice planes. Our geometry is consistent with the (001) surface of an fcc crystal and thus $G/\tau_{max} \sim 4.4$. Experimental studies of the friction force on islands may be able to reach scales where saturation to the Peierls stress can be observed.[16] The core width would be smaller and the Peierls stress much larger if the interaction between solids was stronger than the internal interactions. As noted by Müser,[149] such interfaces are likely to be metastable against alloying. However he found no mixing on simulation time scales for systems that would correspond to $b_{core} \sim d$ where our calculated Peierls stress is large.

The directional covalent bonding in silicon and diamond can lead to large yield stresses and small dislocation core widths $b_{core} \sim d$.[152,153] As expected from Fig. 6.3, unpassivated incommensurate surfaces of these materials spontaneously deform to form an interface with a yield stress that is comparable to the bulk. Passivating the dangling covalent bonds at the surface with hydrogen reduces τ_{max} to $\sim$ 10MPa, which is characteristic of

van der Waals interactions.[154] The resulting $b_{core} \sim 10\mu$m and the corresponding Peierls stress would be below the limit of detection in practical experiments. Of course it is difficult to make crystalline surfaces of diamond and silicon that are atomically flat on this scale. For multiasperity rough contacts or disordered surfaces there can be a new mechanism of elastic pinning beyond an elastic correlation length determined by the competition between elasticity and the strength of disorder.[155–158] One source of disorder is the variation in phase and magnitude of friction forces from individual asperities like those considered here.

Large atomically flat surfaces are readily obtained for layer materials like MoS_2 and graphite. In these highly anisotropic materials, the width of interfacial dislocations is determined by the competition between stiff covalent bonds within layers and the weak van der Waals interactions between layers.[159] The value of b_{core}/d will be so large that the Peierls stress is negligible and this must contribute to the success of these materials as solid lubricants.

6.3 Conclusions

The results presented above provide new insight into the competition between geometry, elasticity and interfacial shear stress in determining the friction of two dimensional contacts between three dimensional solids. For small contact radii we find the friction scales according to previously derived rules for rigid solids. For commensurate surfaces there is a constant frictional stress, while τ_{fric} decreases as a power of radius for incommensurate surfaces.

Elasticity becomes important only when the radius exceeds the width of edge dislocation cores, $b_{core} = dG/\tau_{max}$. For commensurate surfaces, nucleation at the circular contact boundary leads to a universal decrease in stress as $\tau_{fric} \sim (a/b_{core})^{-1/2}$. The friction stress then saturates at the Peierls stress for dislocation loops to move across the interface. We see that the stress also saturates at large a/b_{core} for incommensurate cases. Moreover, the Peierls stress is nearly the same for commensurate and incommensurate systems at

small b_{core} and λ. In all cases the saturation stress drops rapidly with G/τ_{max}. Thus there is no true zero friction state in finite contacts but the friction stress may be extremely small in large stiff systems.

Chapter 7

Static friction of a repulsive commensurate spherical asperity

The sliding of a sphere on a flat surface is a fundamental model in tribology. It arises for example when modeling an atomic force microscope (AFM) tip, a surface force apparatus (SFA) experiment, or a single asperity in a rough contact. Textbook analyses based on continuum mechanics typically consider a local friction law that is either proportional to normal pressure or independent of it.[20,22,115] In the first case, associated with non-adhesive contacts, the continuum analysis shows that the static friction of the asperity is simply proportional to normal load. In the second case, associated with adhesive contacts, the static friction is simply proportional to area.

It was therefore notable when Hurtado and Kim[27,28] predicted instead that the friction should depend non-trivially on the size of the contact in the case of commensurate crystalline contact. This was discussed in Ch. 6, where we simulated the problem using an atomic-scale lateral-force model. That model reproduced the scaling predictions of Hurtado and Kim when the model was in the commensurate configuration.

In this chapter, we address the problem with direct molecular dynamics simulation (MD) and use non-adhesive Lennard-Jones surfaces. This model produces size-dependent friction that is quite different from the model of Hurtado and Kim.[27,28]

This chapter shows that for non-adhesive commensurate contacts, the quantity $\alpha a^2/Rb$ determines the asperity static friction, where R is the sphere radius, b is the Burgers vector of dislocations at the interface, and α is the microscopic static friction coefficient.[9,115]

We find that, in small contacts ($\alpha a^2/Rb \lesssim 1$), the surfaces are effectively rigid and the asperity friction coefficient μ equals the microscopic value, $\mu = \alpha$. If the contact radius is increased, the friction coefficient falls as a power law, $\mu \sim \alpha(a^2/bR)^{-2/3}$. In very large spherical contacts the friction coefficient rises again as the pressure increases.

We investigate the origins of this new behavior by returning to the lateral force model of Ch. 6. In Ch. 6 the model used a stress to slip τ_{max} that was a material constant. We refer to this as an adhesive-friction law. In the present chapter, we set the stress to slip to be proportional to the Hertz pressure, $\tau_{max} = \alpha p$. This is the microscopic version of Amonton's law, commonly found to hold in non-adhesive contacts.[9,115]

In the last part of the chapter, to study the role of dislocations in a simpler setting, we return to the model of constant stress to slip, $\tau_{max} = \tau_0$. As discussed in Ch. 6, this model follows the essential scaling predictions of Hurtado and Kim. We show that this is a noteworthy success of their simple theoretical model, since the simulations in this chapter reveal the breakdown of assumptions of radial symmetry and a single Peierls stress.

7.1 Simulation methods

7.1.1 LJ-MD model

Our explicit simulations consider quasi-static sliding of a rigid spherical tip over a flat semi-infinite elastic substrate Fig. 7.1(a). Holding the spherical tip rigid reduces the number of parameters in this study, and this geometry can be mapped to the sliding of two elastic, curved surfaces in continuum theory.[20] We consider only $a/R < 0.1$ since the peak strain is a/R in continuum theory and we limit this study to elastic deformations in the bulk.

The atoms of the crystalline tip form a square grid of spacing b in the x-y plane, displaced in the z direction to the spherical surface. The tip thus resembles a bent (001) surface of an fcc crystal. The substrate surface is commensurate with the same lattice parameters. Interactions across the crystalline interface use the Lennard-Jones (LJ) pair

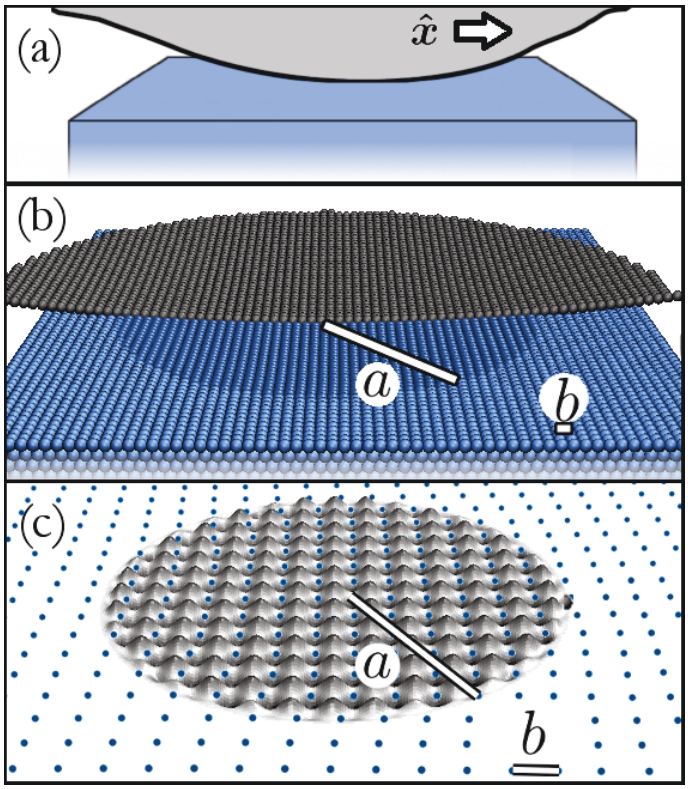

Figure 7.1: We consider an idealized geometry of a sliding asperity with non-adhesive interactions. (a) In the continuum picture the surface is smooth below a specified length scale. (b) MD simulations of a solid include atomic geometry. A bent, commensurate crystalline lattice most closely mimics the continuum picture. In the image, much of the rigid sphere has been cut away to show the atoms that experience a repulsive force (in darker color). (c) In the lateral force model, forces are applied directly to the substrate.

potential $V_{LJ} = 4\epsilon((\sigma/\mathrm{r})^{12} - (\sigma/\mathrm{r})^{6})$ between atoms separated by r. Non-adhesive interactions are created by truncating the potential at its minimum, $\mathrm{r}_{cut} = 2^{1/6}\sigma$, as in previous chapters. We refer to this as the LJ-MD model. A schematic of the LJ-MD sphere is shown in Fig. 7.1(b).

The substrate is simulated using the GF of an isotropic solid with shear modulus G (Sec. 3.8.3). Green's functions of crystalline lattices give similar results, while this GF allows direct comparison with previous work[27,29] (including Ch. 6) and allows us to concentrate on the general effects of the atomic geometry at the interface. A Poisson ratio of $\nu = 0.5$

decouples displacements in different directions under the sphere[20] and allows the substrate to remain essentially commensurate with the sphere during normal loading. Quasi-static sliding occurs by iteratively displacing the rigid sphere in the x-direction by steps of distance 0.01σ at a fixed load and minimizing the energy after each step.

The repulsive LJ wall interaction between these commensurate surfaces produces a local interaction that follows Amontons' law that friction force is proportional to normal force.[141] The microscopic static friction coefficient, α, for this wall interaction is essentially given by the largest surface slope along the sliding path, which is shown as a black line in Fig. 7.2. This means that the lateral stress τ in the LJ-MD model reaches a maximum τ_{max} which is proportional to the normal pressure p, $\tau_{max} = \alpha p$. Since the normal pressure p approximately follows the Hertzian prediction for the pressure under a sphere (Sec. 2.1.1), τ_{max} varies across the contact, going to zero at the contact edge, $r \to a$.

We will see that dislocations form at the interface. As noted in the previous chapter, the characteristic width of the dislocation core is

$$b_{core} \equiv bG/\tau_{max} \tag{7.1}$$

and this scale plays an important role in this chapter as well. Note that the variation of τ_{max} throughout the contact means that $b_{core} \to \infty$ at the edge of the contact. b_{core} has a minimum size at the center, $b_{core} = b_{core}^{(r=0)} = bG/\alpha p_0$, where p_0 is the pressure in the center of the contact. The ratio of the contact radius to this central core width determines the sliding regime. Using the Hertzian relation we find

$$a/b_{core}^{(r=0)} = c\alpha a^2/(bR) \tag{7.2}$$

where $c = 4/(\pi(1-\nu))$.

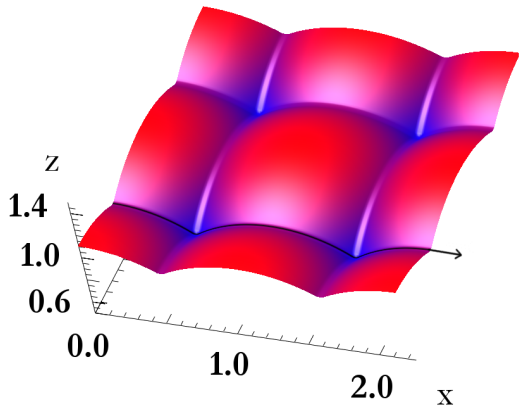

Figure 7.2: The sliding path for non-adhesive, commensurate LJ surfaces. Since the surfaces are commensurate, the surface plotted here is simply the equilibrium height above the substrate of a test atom at a position x-y subject to a z-force of $1\epsilon/\sigma$. The substrate is held rigid and units of the axes are (σ). The sliding path for commensurate surfaces is generally through the minima, shown in black, and the maximum slope of the sliding path is $\alpha \approx 1/\sqrt{2}$. As an aside, this plot also shows the shape of the Γ-surface at normal pressure $1\epsilon/(b^2\sigma)$. The Γ-surface (discussed in Ch. 2) gives the energy as a function of rigid translation of one surface over the other at a given external pressure. Its slope is the lateral force. The shape of the surface is due to changes in interfacial energy and also due to atoms of one surface rising up and over the atoms of the other subject to the applied normal pressure. For the stiff LJ interaction, there is comparatively small variation in the interfacial energy at different x-y positions on this surface, and the Γ-surface is approximately the relative height of the surfaces times the normal pressure.

7.1.2 Lateral force model

We also consider another model where the LJ-MD sphere is replaced by a lateral force field applied directly to the substrate surface atoms (Fig. 7.1(c)). The lateral forces represent the interaction with the atomic sphere. We use a simple sinusoidal force like that used for the Frenkel-Kontorova chain and for the two-dimensional Peierls-Nabarro model.[29,30] The force applied to an atom at position (x, y) is $\boldsymbol{f}(x, y) = f_{max}(r)(sin(2\pi x/b)\hat{\boldsymbol{x}}+sin(2\pi y/b)\hat{\boldsymbol{y}})$. Here, the function $f_{max}(r)$ is the envelope of the corrugation which is zero outside the contact, at $r > a$ (where $r = \sqrt{x^2 + y^2}$). Quasi-static sliding is simulated by iteratively translating the force field 0.01σ in the $+x$-direction and minimizing the energy. That is, after sliding a distance d the force applied to an atom at (x, y) is $\boldsymbol{f}(x - d, y)$. We refer to this model as the lateral force model.

The difference from the model of Ch. 6 is that we consider an envelope function, $f_{max}(r)$, that mimics the local forces in the LJ-MD model. As in many commensurate non-adhesive models[141] the tangential force required for sliding obeys Amontons' law at the microscopic level. The ratio of tangential to normal stress is a constant microscopic friction coefficient α. We therefore set f_{max} equal to α times the normal force distribution predicted for Hertz contact (Sec. 2.1.1). Multiplying the pressure by the area per atom b^2 we have $f_{max}(r) = f_0\sqrt{(1 - (r/a)^2}$, where $f_0 = \alpha p_0 b^2 = \alpha E^* b^2 (2/\pi)(a/R)$ and E^* is the contact modulus, defined as $E^* \equiv 2G/(1 - \nu)$.

Note that the forces and motion remain in the x-y-plane in the lateral force model. According to continuum theory (*e.g.* Mindlin[20]) the only effect of the 3D shape of the sphere is to determine the distribution of normal pressure on the surface which sets the local stress to slide, τ_{max}. We later confirm that the lateral force model realizes the same slip mechanisms as the LJ-MD model. Thus the small changes in slope and 3D separations between atoms in the LJ-MD model are not important to the friction. Another difference

is that the lateral force model corrugation is sinusoidal while the LJ-MD model corrugation is not. We later show that the two datasets collapse when each is characterized by its maximum stress to slide, τ_{max}.

In the final part of this chapter we choose instead an envelope $f_{max}(r) = \tau_0 b^2$, *i.e.* a uniform constant. This allows us to repeat the commensurate result of Ch. 6 and emphasize its differences from the present chapter. Then we analyze the dislocation motion in this simpler case (with uniform f_{max}).

7.2 Results

We observe three slip mechanisms that set the static friction. Qualitatively, the three mechanisms are the same as those reported in Ch. 6 (and Ref. 27). However, in the non-adhesive model the onset of each regime and the friction of each regime are different than in the adhesive-friction model.

We briefly describe each regime, then analyze each regime in its own section. In Regime I, characteristic of small contacts, there is no appreciable elastic deformation on the length scale of the contact during sliding. The substrate surface hops coherently over the opposing surface, as illustrated in Fig. 7.3(a). In larger contacts, elastic deformation occurs and slip is mediated by the nucleation of a lattice dislocation that rapidly moves across the interface. This is Regime II and is illustrated in Fig. 7.3(b). In Regime III, the contact is large enough that many dislocations are arrested at the interface. The static friction is set by the condition for dislocations to depin and move along the interface (Fig. 7.3(c)).

For a given set of parameters we define the coefficient of static friction μ as the ratio of the maximum lateral force to the load. Fig. 7.4 presents results for different sphere radii R and for both the LJ-MD model (black symbols) and lateral force model (colored symbols). Results for all systems collapse when plotted against $a/b_{core}^{(r=0)} = c\alpha a^2/bR$ (Eq. 7.2). The three friction regimes are indicated by labels at the top of the figure. Note that since μ

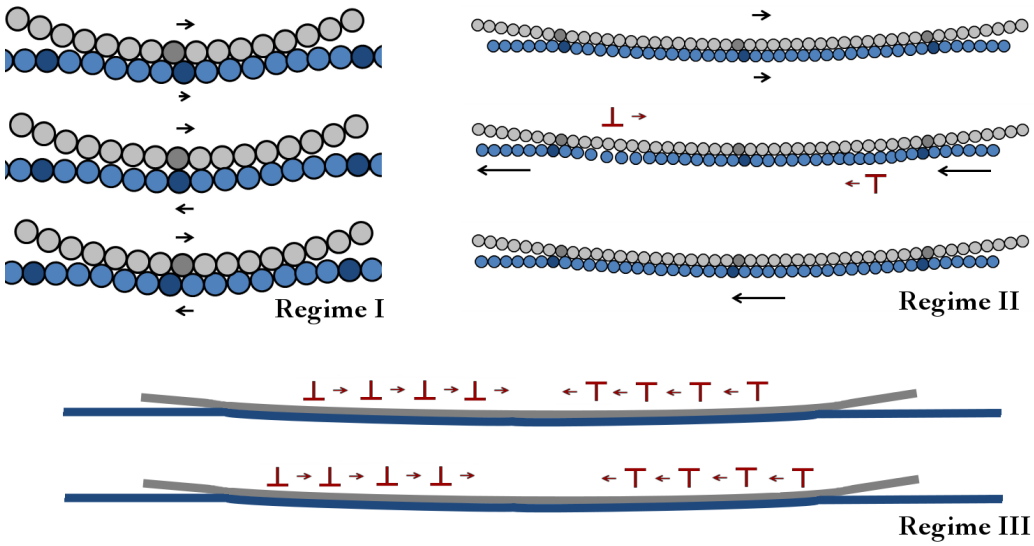

Figure 7.3: Schematic of rigid slip (Regime I), slip by dislocation nucleation (Regime II), and slip by dislocation unpinning (Regime III). In all cases, the top snapshot shows the configuration at maximum friction. Some atoms are labeled with darker colors to show relative motion. In (a), the rigid asperity slides over the substrate and any lateral displacements in the substrate are too small to alter the registry of atoms on opposing surfaces. In (b), the surfaces are initially pinned, but a small displacement nucleates dislocations at the edge of the contact. Edge dislocations are indicated schematically, and they glide through the contact and self-annihilate, resulting in slip of a Burgers vector. In (c), in very large contacts, dislocations become arrested in the contact and further sliding of the asperity is required for them to self-annihilate.

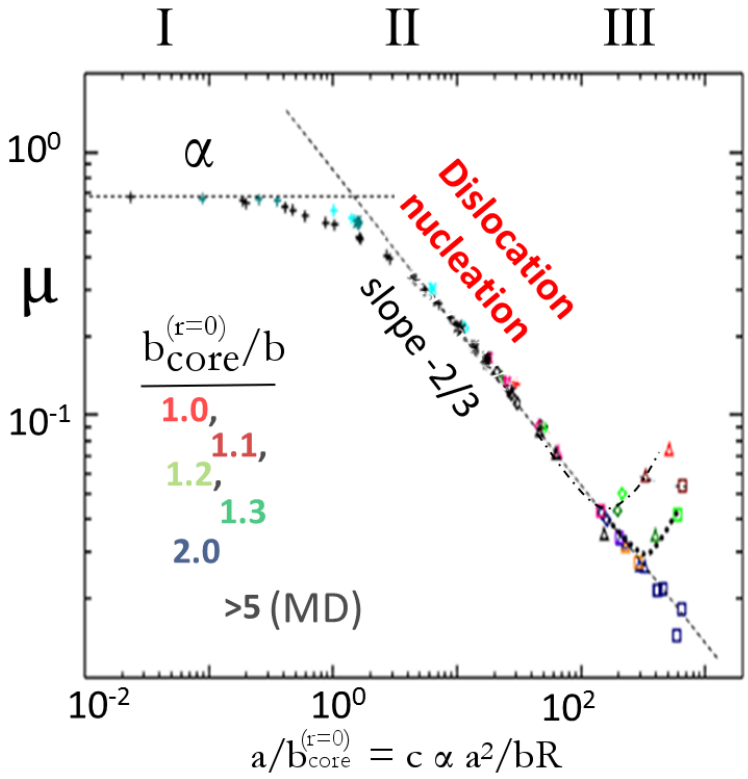

Figure 7.4: Friction coefficient for non-adhesive surfaces plotted against contact radius over central dislocation width (Eq. 7.2). Results are shown for the LJ-MD model (black symbols) and lateral-force model (colored symbols) with different elastic moduli corresponding to the values of $b_{core}^{(r=0)}/b$ in the legend. The three regimes of different sliding mechanism are indicated at the top of the figure. Dashed lines show the constant friction coefficient in Regime I, the power law decrease in μ in Regime II, and the rise in μ in Regime III.

varies with a and a depends on the normal load, the coefficient of friction will only be independent of load for systems in Regime I. The following sections analyze each of the three regimes in turn.

7.2.1 Regime I

In Regime I, atoms in the commensurate contact are not distorted significantly during sliding so that all contribute coherently. In particular, this happens in contacts that are small compared to the dislocation core width. From the Peierls-Nabarro model of dislocations,[23]

the dislocation core width b_{core} is the shortest length over which the interfacial corrugation strains the solids to create mis-registry of approximately the Burgers vector b. A contact of radius $a < b_{core}$ therefore does not get distorted a distance b over its length. If $a \ll b_{core}$ the two contacting surfaces are effectively rigid on the length scale of the contact. In this case, the atoms are not distorted during sliding so that all contribute forces perfectly coherently as they slide through the corrugation of the opposing surface.

In the lateral force model, to overcome the barrier to slide, the stress in the commensurate contact everywhere reaches the local maximum, $\tau_{max} = \alpha p(r)$, at the same time. Averaging across the contact gives the static friction stress $\tau_{fric} = \langle \tau_{max}(r) \rangle = 2/3\, \alpha p_0$. The static friction coefficient $\mu = \tau_{fric}/\langle p \rangle = \alpha$. In the 3D LJ-MD model, the normal pressure distribution can deviate from the ideal Hertz distribution during sliding, but all atoms still contribute coherently with a stress proportional to the local pressure. Since the sum of local pressures is always equal to the total normal force, the friction coefficient is the same. As shown in Fig. 7.4, μ is independent of contact size in Regime I.

Having only one degree of freedom sliding in an external corrugation, the contact in Regime I is a realization of the single-particle Prandtl-Tomlinson (PT) model.[29,142] The PT model is a model of friction that is like the Frenkel-Kontorova chain (Ch. 2), but simpler, since there is only one atom in the sinusoidal potential. In the PT model, this atom is pulled by a spring of stiffness k attached to an external drive. The dimensionless PT constant λ characterizes the ratio of interfacial stiffness to elastic stiffness. It is defined as $\lambda \equiv 2\pi F_{max}/(bk)$ where F_{max} is the max interfacial force and b is the period of the corrugation. With quasi-static translation of the drive, the atom position varies continuously if $\lambda \leq 1$ or with stick-slip motion otherwise.[142] We now show that if the only compliance contributing to k is that of the contacting solids, λ is always less than 1 in Regime I sliding.

In Regime I, the surfaces are effectively rigid within the contact, and the stiffness of the substrate is $k = 8Ga/(2-\nu)$. The PT constant is $\lambda = \pi(2-\nu)\,\overline{\tau_{max}}\, b/(4Ga)$ where

the average τ_{max} is $\overline{\tau_{max}} = 2\tau_{max}^{(r=0)}/3$. Since the length scale $b_{core}^{(r=0)} \equiv bG/\tau_{max}^{(r=0)}$, λ can be written in terms of $a/b_{core}^{(r=0)}$: $\lambda = (2/3)(a/b_{core}^{(r=0)})(1/4)\pi(2-\nu)b^2/a^2$. The Tomlinson stick-slip instability occurs only when $\lambda > 1$ (which is $(a/b_{core}^{(r=0)}) \gtrsim a^2/b^2$). However, as we will see in Regime II, a dislocation slip instability occurs already when $a/b_{core}^{(r=0)} \gtrsim 1$ and gives a friction dependent on contact radius. The Tomlinson stick-slip instability is therefore superseded by the dislocation instability as long as the contact radius is larger than about 1 atomic diameter, $a > b$. We see therefore that the stick-slip regime of the single-particle Tomlinson model does not describe the motion of commensurate contact between large crystals. Any observed stick slip between commensurate crystals is a result of either additional compliance elsewhere in the system (*i.e.* an AFM tip geometry or cantilever) or is due to different parts of the surface slipping at different times, not as a single degree of freedom. The latter situation occurs in contacts in Regime II.

7.2.2 Regime II

If the contact radius a is increased to be sufficiently larger than $b_{core}^{(r=0)}$, sliding occurs in Regime II. In Regime II the advancing rigid solid drags the commensurate contacting surface of the elastic substrate along to distances greater than atomic distances. One may approximate that the contact all advances together so that the elastic substrate is rigidly displaced up to the static friction. This is the geometry of a displaced contact and the linear elastic analysis is well-known (*c.f.* Sec. 2.1.2 or Ref. 20): the stress field is the lowest at the center and has a $\delta^{-1/2}$ stress singularity at the contact edge, where $\delta \equiv a - r$. This is the same singularity as in the linear elastic analysis of a crack tip, since the geometry is the same near the contact edge. Atomic discreteness cuts off the singularity of the linear elastic analysis.

As an aside, the elastic substrate is not perfectly rigidly displaced, since atomic compliance with respect to the upper solid allows the substrate surface to deform slightly on

the length scale of the (sinusoidal or LJ) corrugation potential well. Indeed if the substrate displacement were perfectly rigid, all atoms would sample the corrugation of the opposing wall in phase, resulting in spatially-uniform stress across the interface. But the atomic-scale displacements from the atomic compliance are small compared to the total displacements and do not change the stress field significantly from that of a uniformly-displaced contact. An exception is near the contact edge, where the atoms experience the anharmonicity of the corrugation when the stresses become comparable to τ_{max}. This same situation arises in the well-known treatment of a crack tip that uses linear elastic analysis and a stress intensity factor.[26]

Fig. 7.5 shows snapshots of the stress within contacts in Regime II. Subfigure (a) shows the LJ-MD model and subfigure (b) shows the lateral force model. The stress builds strongly near the contact edge. A lattice dislocation is nucleated when the stress has built sufficiently (shown just before this point in red symbols in Fig. 7.5). The nucleated dislocation immediately glides through the contact and self-annihilates at the center, causing the full contact to slip one Burgers vector, and lowering the stress. The maximum force to slide is therefore due to the need to nucleate a dislocation at the edge of the commensurately-pinned contact.

We also comment on the predicted radial-symmetry of the stress field. A uniformly-displaced circular contact in isotropic linear elasticity has radially-symmetric stress.[20,27] This radial symmetry is reproduced in the atomic simulations to within a single atom diameter at small displacements (but not exactly due to the discretization of the GF). Increasing the displacement builds the stress near the edge and the anharmonicity of the corrugation potential becomes important. The non-linearity destroys radial symmetry near the contact edge, and a dislocation is nucleated first as screw dislocations from the $\pm y$ directions (as opposed to as edge dislocations from the $\pm x$ directions or from all direction simultaneously). This is because the screw-character has a smaller physical core size than

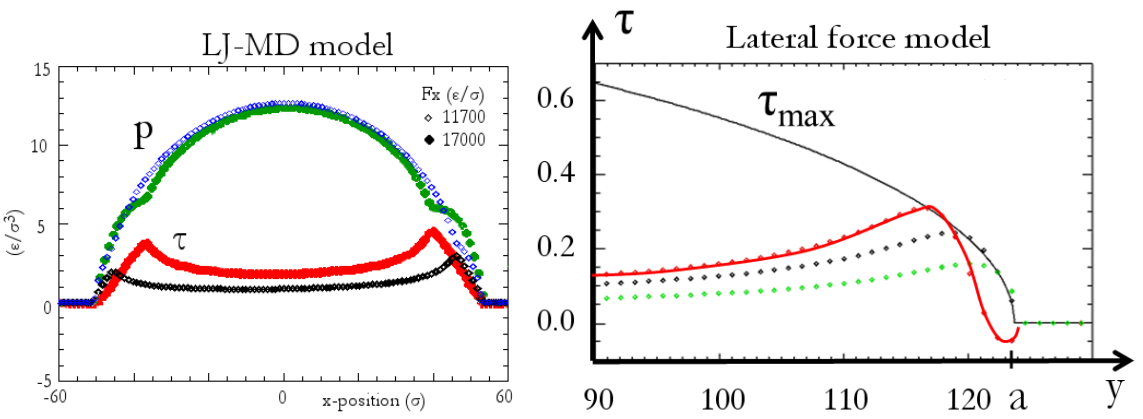

Figure 7.5: The stress $\sigma_{xz} \equiv \tau$ at the surface is plotted along a slice near the edge of a contact in Regime II. The LJ-MD model (a) and the lateral force model (b) are shown. Also shown is the normal pressure $\sigma_{zz} \equiv p$ in (a) and the applied τ_{max} in (b). Sliding a small distance produces a peak in shear stress near the edge and lower stress at the center (black symbols). The stress builds to its maximum just before a dislocation is nucleated (red symbols). An infinitesimal sliding distance further, the dislocation fully nucleates and glides through the contact to the center of the contact, $r = 0$. The result is that the stress has dropped (green, in (b) only).

edge dislocations (discussed later in Fig. 7.8) and its lower energy is known to commonly cause screw dislocations to nucleate more easily than edge. Its effect on the shape of arrested dislocations in the contact is discussed in connection to Sec. 7.2.5.

The static friction is set by the force needed to nucleate the dislocation. Rice and Thompson[160] provide the standard analysis of this situation based on the unstable stacking fault energy of the crystal. The nucleation criterion of Rice and Thompson[160] implies that τ reaches τ_{max} a distance b_{core} from the free surface and contact edge, and this is used in Hurtado and Kim's analysis of the sliding contact.[27,29] In our case, at the edge $b_{core}^{(r\to a)} \to \infty$ because normal pressure vanishes. The nucleation condition must be generalized to include this variation. Since $b_{core}(r)$ gives the scale for variations in displacement at each r, it is natural to assume that the nucleation criterion should be applied at a distance b_{core} from the edge. We define a radius $r^* = a - b_{core}^{(r=r^*)}$ and expect nucleation when the stress at r^*

exceeds the local maximum stress, $\tau_{max}(r)$:

$$\tau(r^*) = \tau_{max}(r^*) \tag{7.3}$$

Far enough from Regime I, r^* is sufficiently close to the edge so that the $\delta^{-1/2}$ singularity dominates and

$$\tau(r^*) \sim \frac{F_x}{\pi a^2}(b_{core}^{(r=r^*)}/a)^{-1/2} \tag{7.4}$$

where F_x is the total lateral force. Meanwhile the Hertzian form of the pressure looks like a square root near the edge, and τ_{max} is proportional to pressure:

$$\tau_{max}(r^*) \sim \frac{F_z}{\pi a^2}(b_{core}^{(r=r^*)}/a)^{1/2} \tag{7.5}$$

Fig. 7.5(b) shows τ_{max} and τ just before a dislocation is nucleated, showing the square-root and inverse-square-root scaling.

To complete the derivation, Eqs. 7.5 and 7.4 are substituted into Eq. 7.3 to solve for the ratio F_x/F_z required to nucleate a dislocation. To put into terms of $b_{core}^{(r=0)}$ instead of $b_{core}^{(r=r*)}$, we first rewrite Eq. 7.4 more explicitly as

$$\tau_{max}(r^*) \approx \tau_{max}(0) \cdot (2b_{core}^{(r=r^*)}/a)^{1/2} \tag{7.6}$$

then substitute in the definition (Eq. 7.1) of $b_{core}^{(r=r^*)} = bG/\tau_{max}(r^*)$ and rearrange to produce

$$(\tau_{max}(r^*))^{3/2} \approx \tau_{max}(0) \cdot (2bG/a)^{1/2} \tag{7.7}$$

Then $b_{core}^{(r=r^*)} \sim (b_{core}^{(r=0)})^{2/3}$ or more precisely,

$$b_{core}^{(r=r^*)} \approx a^{1/3}(b_{core}^{(r=0)})^{2/3}/2. \tag{7.8}$$

Substitution of Eq. 7.8 into Eqs. 7.5 and 7.4 and then into Eq. 7.3 shows that the asperity

x-force required to nucleate a dislocation is given by

$$\mu = F_x/F_z \sim \alpha(b_{core}^{(r=0)}/a)^{2/3}. \tag{7.9}$$

Regime II in Fig. 7.4 shows a friction coefficient that falls with this power law.

The nucleated dislocation has Burgers vector $\boldsymbol{b} = b\hat{x}$. According to the Peach-Koehler law, the dislocation is driven in the glide plane by the shear stress at the interface, τ. τ is approximately radially-isotropic and drives the dislocation to the center where it self-annihilates. We point out that the radial gradient in τ_{max} provides an outward configurational force on the dislocation, since the core energy is lower near the edge where τ_{max} is lower. In Regime II, the net driving force on the dislocation overcomes the Peierls stress. Once nucleated from all directions at the edge of the contact, the dislocation glides to the center where it self annihilates, and the contact has slipped forward one Burgers vector.

7.2.3 Regime III

In Regime III, a dislocation is nucleated at the contact edge while the stress at the center of the contact remains low. The dislocation glides part way through the contact. The stress is insufficient to drive the dislocation against the Peierls stress and the dislocation is arrested in the contact before annihilating. Additional lateral displacement raises the stress and depins the dislocation. The stress can also nucleate new dislocations and cause them to pile up. In Regime III, the static friction is ultimately associated with a Peierls stress to move the many arrested dislocations.

The classic Peierls-Nabarro model shows that the Peierls stress of a dislocation falls exponentially with core width, $\tau_{Peierls}/\tau_{max} \sim exp(-b_{core}/d)$.[25] Accordingly, $\tau_{Peierls}$ is largest at small b_{core}. Under a given size sphere R, increasing contact radius a implies increasing the pressure, which decreases the core width. Correspondingly, the Peierls stress

rises under a given size sphere in Regime III. This is an important difference from the adhesive friction model.

We are unable to reach far into Regime III with the LJ-MD model due to computational limitations. The reason is that the minimum dislocation core width is somewhat large and so the contact size would need to be increased above what the simulations reached. In particular, the nominal dislocation core width in the LJ-MD model is given by $b_{core}^{(r=0)} = bG/\alpha p_0 = (b/\alpha)(R/a)(G/E*)(\pi/2)$ (using the Hertz pressure p_0). From the geometry of the LJ potential, $\alpha \approx 1/\sqrt{2}$. To avoid complications from large surface slopes, $a/R < 0.1$, and therefore the $b_{core}^{(r=0)} \gtrsim 5$. The Peierls stress is correspondingly low and dislocations are only arrested in very large contacts. On the other hand, the lateral force model can reach larger $a/b_{core}^{(r=0)}$ by decreasing $b_{core}^{(r=0)}$ without complications of 3D distortions from small a/R. The lateral force model therefore extends the data further into Regime III. These data points are included as colored symbols in Fig. 7.4.

The dislocation motion that underlies the friction of Regime III will be discussed in more detail in Sec. 7.2.5 after contrasting the above results (non-adhesive friction) with the adhesive-friction model.

7.2.4 Comparison with adhesive friction model

The adhesive friction model was introduced in Ch. 6. That model was the same as the lateral force model discussed in this chapter, except τ_{max} was a material constant and uniform throughout the contact. Ch. 6 used the adhesive model to show that atomic simulations of commensurate contact produce the predicted dislocation slip mechanism. Fig. 7.6 shows the scaling of friction with contact size, which matched the predictions of Hurtado and Kim.[27,28] The friction was strikingly different from the non-adhesive model, shown in Fig. 7.4.

Both models show the same three underlying slip mechanisms and produce three

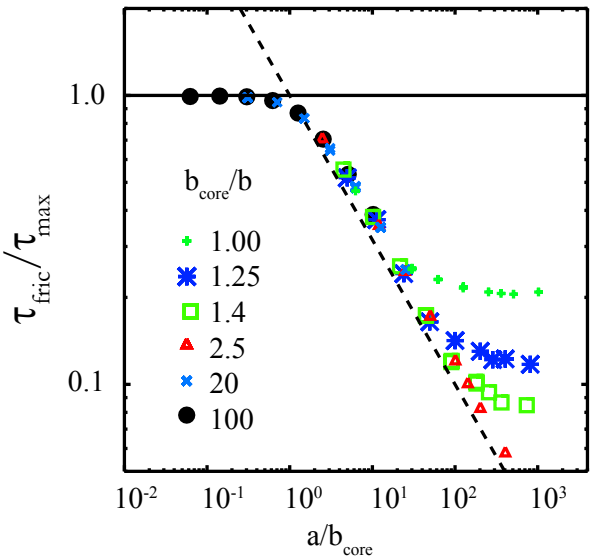

Figure 7.6: The friction force per unit area, τ_{fric}, is plotted for the τ_0-model. Data follows the scaling prediction $\tau_{fric} = (a/b_{core})^{-1/2}$ (dashed line) in Regime II and tends toward a constant in Regimes I and III.

regimes of friction. However, even the axes of Fig. 7.4 and Fig. 7.4 are different. In Regime I, atoms overcome their potential barriers coherently. But for the adhesive friction model, the dimensionless Tomlinson constant is $\lambda = (a/b_{core})1/4\pi(2-\nu)b^2/a^2$. Then contacts in Regime I exhibit a friction stress (friction force per area) that is independent of contact radius (rather than a constant friction coefficient which is a friction force per normal load).

Notably, since τ_{max} is constant throughout the contact of the adhesive model, so is b_{core}. This means that in Regime II the dislocation nucleation criterion (Eq. 7.3) is simpler, since $b_{core}^{(r=r^*)} = b_{core}$. From the $\delta^{-1/2}$ form, the nucleation occurs when the friction force per area is $\tau_{fric} \propto \tau_0(a/b_{core})^{-1/2}$.

Regime III is when the contact is sufficiently large so the stress at the center is low and dislocations become arrested by the Peierls stress. The static friction is therefore set by the stress required to unpin the dislocations. The next section analyzes the dislocation motion in more detail with implications for both adhesive and non-adhesive models.

7.2.5 Additional analysis of dislocation motion in Regime III

In Regime III of both the adhesive (and non-adhesive) lateral force model, many dislocation loops are arrested in the contact. (See Fig. 7.7(d).) The loops are subject to dislocation interactions via the stress field and a Peierls stresses which varies with dislocation character. The configuration may be complex since there is a lack of radial symmetry. Fig. 7.7 shows a few typical configurations. We see initial nucleation in the $\pm y$-direction edges as screw dislocations. This is consistent with the fact that screw dislocations have the tightest core size. By the time the dislocation nucleates at the leading and trailing edge as edge dislocations, the screw dislocation has glided towards the center, and the dislocation loop is elongated in the x-direction. Also, the higher energy of edge dislocations means that the dislocation loop tends to minimize that character, helping to preserve the elongation in the x-direction. In very large contacts with small b_{core}, dislocation kinks (in-plane jogs) also form as some segments of the dislocation are arrested while other segments glide within the plane.

To determine the Peierls stress of a dislocation (Fig. 7.8(a) and (b)), independent simulations are conducted. An edge, screw, or mixed-character dislocation is created in a large system. The dislocation is created by applying a slightly stretched or skewed sinusoidal potential to the Green's function substrate layer. The Green's function of Sec. 3.8.2 is used. To be consistent with the periodic boundary conditions, the distortion corresponds to an integer number of atoms. An isolated dislocation forms where the potential is maximally out of phase. Applying external stress (sliding the corrugation) causes the dislocation to glide. The highest stress is recorded as the Peierls stress.

Fig. 7.9 shows the stress environment at each dislocation throughout a large contact. The dislocations have edge character in the shown slice. Interestingly, the stress at all dislocations is lower than the edge Peierls stress for the core width, as indicated by

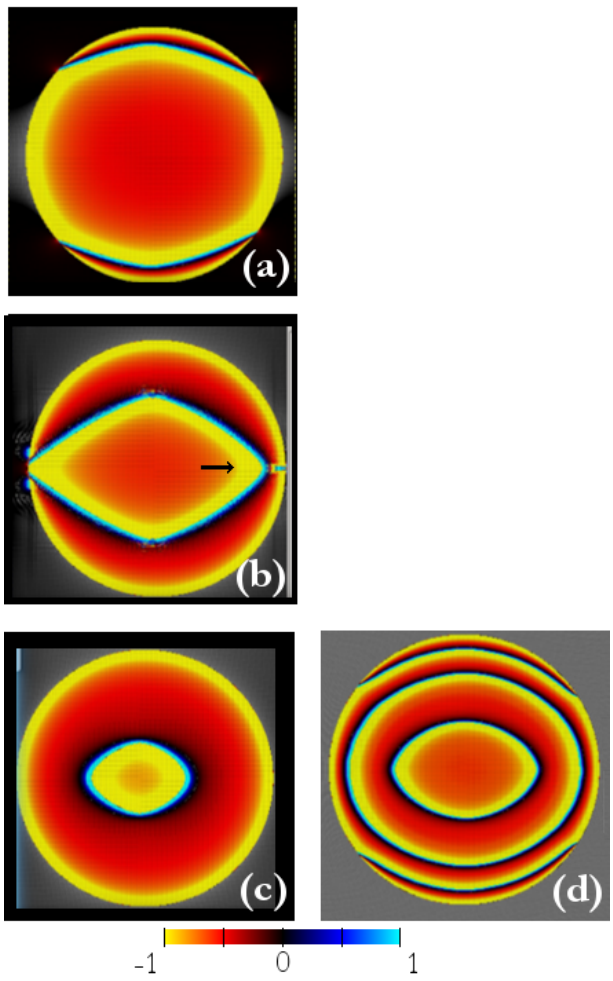

Figure 7.7: Images of dislocation nucleating where the color shows force per atom, where the color bar units are normalized by f_{max}. Radial symmetry is lost already as the first dislocation nucleates: the small core width of screw dislocations leads to nucleation before edge dislocations. (a) (b) and (c) show a contact between Regime II and Regime III (parameters $a = 126b$, $b_{core} = 2b$) so that the dislocation moves slowly though the contact. (d) shows a case with higher Peierls stress with $a = 126b$, $b_{core} = 1b$, so the contact is essentially in Regime III. In that case there are two fully-formed dislocation loops and a third loop still forming. The examples are from the adhesive model (with constant $\tau_{max} = \tau_0$).

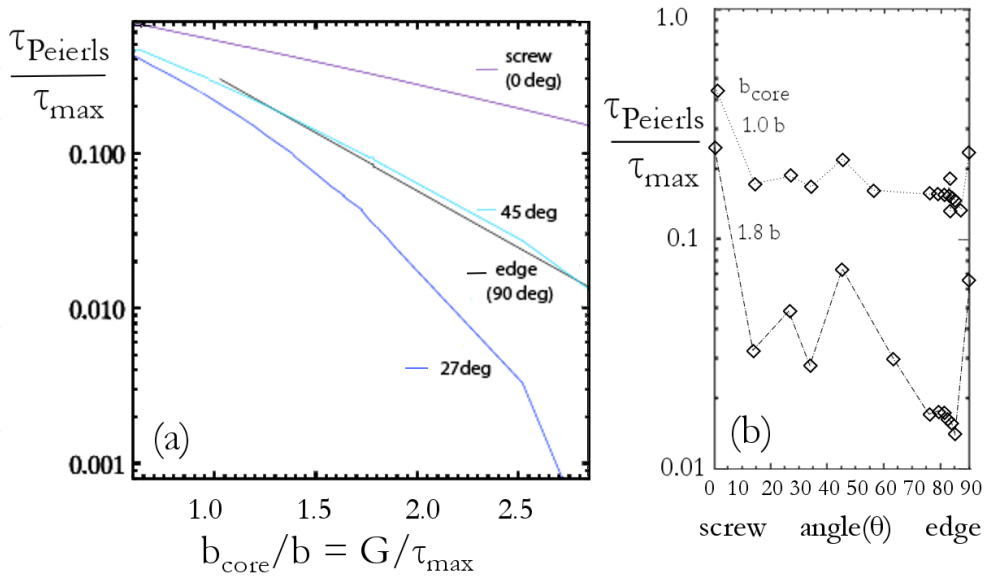

Figure 7.8: The Peierls stress for edge and screw and mixed character dislocations (a) as a function of core width and (b) as a function of character.

the horizontal bar in Fig. 7.9. One reason is that the curved dislocation samples Peierls stresses from all angles from edge to screw. Another reason is because the Peierls stress provides an upper bound for the stress state near the arrested dislocation. The stress around the dislocation cannot be greater than $\tau_{Peierls}$, because then the dislocation would still be moving. At first, it seems that the stress cannot be less than $\tau_{Peierls}$ either, because the dislocation would not have been able to reach its current location. But the stress itself changes as neighboring dislocations glide. The Peierls stress saturation in large contacts is therefore not the same as the Peierls stress of say an edge dislocation, but depends on the configuration and dynamics of the dislocations. The dislocation dynamics can be expected to depend sensitively on the specifics of the crystalline material.

7.3 Conclusions

Elasticity lowers friction in commensurate contacts by allowing different parts to slip at different times. These motions are coherent on a length scale b_{core}. The boundary between

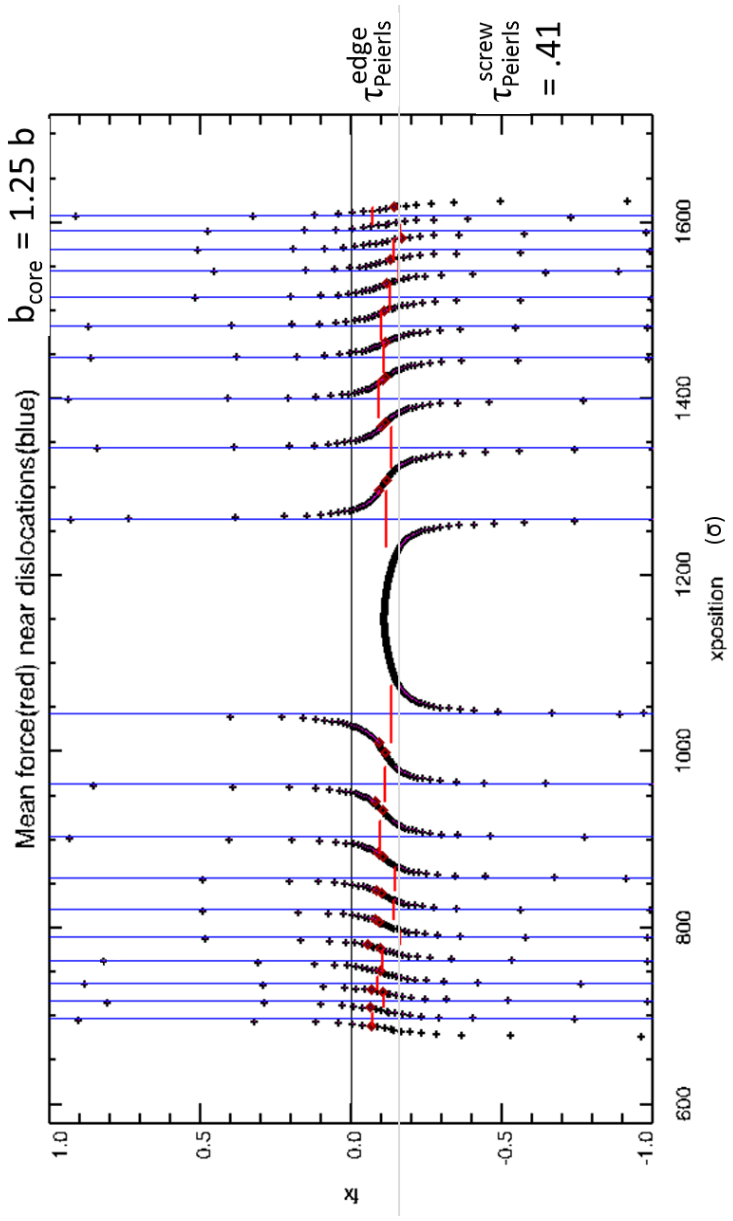

Figure 7.9: Atomic forces as a function of x position in a cross section through a large contact in the lateral force model. The vertical axis is in units of f_{max}. Dislocations are piled up in the contact; they are automatically identified by the large positive and negative forces and labeled with vertical blue lines. The applied stress at each dislocation (indicated with horizontal red bars at the location of each dislocation) is determined by averaging the stress an equal distance on both sides of the dislocation. The dislocations are edge character but the environmental stress is below the Peierls stress of an edge dislocation (indicated with a grey horizontal line). Cross-sections in other directions show essentially the same stresses, though the dislocations have screw and mixed character in those directions.

a slipped and a non-slipped region takes the form of a lattice dislocation at the interface. The local friction law (adhesive vs. non-adhesive friction) sets the emergent asperity-level friction, as encoded in Fig. 7.6 and Fig. 7.4. Fig. 7.4 points out a new power law in size-scaling that occurs when the interface has a pressure-dependent τ_{max} characteristic of non-adhesive contacts. These also represent the first simulations in the Peierls-stress dominated regime for large crystalline contacts. Even with a circular model geometry, considerable complexity emerges due to the large number of degrees of freedom associated with the dislocations. Nonetheless, a near uniform stress is measured through the contact.

The possibility remains open that plastic deformations outside of the contact plane, may sometimes supersede the interfacial instability discussed here. This could depend on the loading configuration and the relative strength of interactions across the interface and in the bulk.

The tribology-inspired description of τ_0-vs-αp can be further generalized with the pressure dependence of the Γ-surface (or generalized stacking fault energy) studied in the context of materials science dislocations. Corrugation near the contact edge may scale with a square-root of the distance to the edge (due to the Hertz pressure as seen here for repulsive LJ interactions) or with a different form due to different atomic interactions. Moreover the corrugation may switch phase or have non-monotonic increase in amplitude near the nucleating edge. The work here emphasizes the sensitivity of the dislocation nucleation criterion to these atomic features as well as to the stresses from the large scale geometry.

Chapter 8

Conclusions

This thesis draws from elasticity, statistical physics, and lattice dislocation theory to address questions about the mechanics of contacting solids. The mechanics were often determined by an interaction of large and small scale geometry, so that neither could be neglected from consideration. This made Green's function molecular dynamics, described in Ch. 3, a natural tool to simulate these systems. Several important limitations of previous Green's function formulations were overcome to increase the range of problems that can be addressed. First the approach for pair interactions was corrected.[161] Next the effect of periodic boundary conditions was eliminated so that single-asperity contacts could be studied. Finally, the approach was extended to many-body potentials such as EAM and Stillinger-Weber. This opens the door to a wide variety of material-specific problems in the future.

Ch. 4 initiated the investigation into the contact properties of rough solids, testing predictions from continuum theory with numerical simulations. Simulations of atomic solids with bent surfaces followed the predicted linear relationship between contact area and load. We also verified the predicted exponential increase in load with decreasing separation. As a result, the derivative of normal load with separation, or normal contact stiffness, was proportional to load. The normal contact stiffness was shown to depend only on the geometry of the current contacting regions and is insensitive to atomic structure. In sharp contrast, the stiffness resisting lateral motion depends sensitively on atomic-scale interactions and can be orders of magnitude lower than normal stiffness.

Ch. 5 revisited the contact mechanics of solids with additional realistic atomic features. The distribution of contact pressure and contact area can depend on small-scale

features like atomic surface steps, compliant atomic interactions at the interface, and the yield stress of the material. In rough elastic contacts the pressure probability distribution shows an exponential-like tail indicating that very small regions of the contact carry pressure far above the mean contact pressure. For materials that can yield, pressures that are large compared to the yield stress can produce plasticity. Since some regions of the surface carry pressure far above the mean, even surfaces with moderately low surface slope produce atomic-scale plasticity, and one might naively conclude that analysis of purely elastic contacts is irrelevant in most practical situations. However, since high pressure is only exerted in a very small fraction of the contact, we found that contact area is the same for purely-elastic and for finite-yield-stress materials, as long as the roughness is sufficiently low, as shown in Fig. 5.13. That figure shows that "sufficiently low" is determined by a combination of roughness amplitude and geometry (h'_{rms}, L_{min}, and surface steps). Rougher surfaces can increase the contact area several-fold. Several variations of the definition of contact area all followed similar trends, supporting the physical relevance of the term "contact area." Atomic features do not significantly change the normal contact stiffness across the whole range of parameters investigated, but they do rearrange the spatial distribution of contact pressure at scales of the crystalline steps.

Ch. 6 considered the static friction of a crystalline asperity and its dependence on contact radius. Previous work had suggested that friction stress (force per contact area) goes to zero as the contact radius between incommensurate crystals goes to infinity. When and in what way elastic effects become important for friction were not understood. This work varies contact size, lattice mismatch, and material modulus to reveal the friction produced between sliding crystals. When the contact radius is below a material length-scale related to the core size of dislocations, elasticity plays no role and the friction of incommensurate contacts follows the experimentally observed phenomenon of rigid structural superlubricity. At larger contact radius, dislocations can form in the contact. Dislocation motion sets a

lower bound on the minimum friction stress that can be achieved by increasing contact radius. In contrast to some predictions,[148,162] the explicit simulations in this thesis show that the saturation friction is independent of mismatch at small mismatch. In this case the saturation value is similar to the limiting stress of commensurate surfaces. The precise value of the friction saturation comes about from the interactions of many dislocations with varying character (edge, screw and mixed) pinning and unpinning at different times in a complicated motion. We find that the shear stress to slide in the model is near the Peierls stress of edge dislocations. At larger mismatch, the surfaces nowhere relax into regions of the lowest-surface-energy alignment, but in all cases the limiting shear stress measured falls rapidly with the nominal dislocation core size. Thus between stiff materials the elastic contribution to the friction can be exceedingly small.

Ch. 7 continues investigating the static friction of a crystalline asperity, focusing on the commensurate case. The size-dependence of static friction is found to depend on whether there are adhesive or non-adhesive interactions. In the first case, when local frictional stresses are independent of pressure, characteristic of adhesive contacts, the asperity static friction stress is independent of contact radius for small contact radius. When the contact radius exceeds the scale of dislocation cores, the asperity friction stress falls as a power law of radius, with exponent $-1/2$, down to a limiting value related to dislocation motion. In the second case, when local frictional stresses are proportional to pressure, characteristic of non-adhesive contacts, it is the friction coefficient that is independent of contact radius in small contacts. When the contact radius exceeds a value related to the asperity curvature, the friction coefficient again falls as a power law of radius, but with exponent $-4/3$. At very large contact radius, the friction coefficient of the asperity actually rises with contact radius. These behaviors are explained by analyzing the nucleation and Peierls stress of the dislocations that mediate slip. The condition for dislocation nucleation is especially sensitive to the properties near the edge of the contact, where the adhesive and non-adhesive cases

are very different. The friction of very large contacts emerges as a complex interplay of dislocation dynamics, dependent on many material-specific properties.

The contacts considered here are primarily between clean crystalline surfaces. This may be realized in carefully-controlled, engineered systems or in systems that effectively self-clean. The latter may be more common[17,37,137,163] than one might first expect. Clean crystalline contacts also provide a starting point for an understanding of the deformation mechanisms. Future directions for this work could investigate how quickly new effects are introduced by disorder. Additional disorder from the crystalline system could be adsorbed monolayers that often underlie friction,[9] crystalline defects like grain boundaries,[24] or thermal fluctuations.

In general, the number of degrees of freedom N is tremendously large in most tribological systems of interest, and the $3N$-dimensional phase space is too vast to explore even short distances in all directions. It is clearly necessary to identify the important coarse-grained structure, deformation mechanisms, and statistics to gain understanding. The statistical quantities and meso-scale deformations described in this thesis may be useful to those trying to gain insight into the properties of solid-solid contacts, especially the properties of rough contact and the mechanisms of friction.

Bibliography

[1] B. Luan and M. O. Robbins, "The breakdown of continuum models for mechanical contacts," *Nature*, vol. 435, no. 7044, pp. 929–932, 2005, http://dx.doi.org/10.1038/nature03700.

[2] E. Gnecco and E. Meyer, *Fundamentals of Friction and Wear on the Nanoscale*. Springer, 2007.

[3] D. Dowson, *History of Tribology*. Longman London, 1979.

[4] J. Field, "David Tabor. 23 October 1913 — 26 November 2005," *Biographical Memoirs of Fellows of the Royal Society*, vol. 54, pp. 425–459, 2008.

[5] J. Archard, "Elastic deformation and the laws of friction," in *Proceedings of the Royal Society of London A: Mathematical, Physical and Engineering Sciences*, vol. 243, no. 1233. The Royal Society, 1957, pp. 190–205.

[6] J. Greenwood and J. Williamson, "Contact of nominally flat surfaces," in *Proceedings of the Royal Society of London A: Mathematical, Physical and Engineering Sciences*, vol. 295, no. 1442. The Royal Society, 1966, pp. 300–319.

[7] S. Hyun, L. Pei, J.-F. Molinari, and M. O. Robbins, "Finite-element analysis of contact between elastic self-affine surfaces," *Physical Review E*, vol. 70, no. 2, p. 026117, 2004.

[8] O. M. Braun, M. Peyrard, D. Stryzheus, and E. Tosatti, "Collective effects at frictional interfaces," *Tribology Letters*, vol. 48, no. 1, pp. 11–25, 2012.

[9] G. He, M. H. Müser, and M. O. Robbins, "Adsorbed layers and the origin of static friction," *Science*, vol. 284, no. 5420, pp. 1650–1652, 1999.

[10] M. H. Müser, L. Wenning, and M. O. Robbins, "Simple microscopic theory of Amontons's laws for static friction," *Physical Review Letters*, vol. 86, no. 7, p. 1295, 2001.

[11] S. Cheng and M. O. Robbins, "Defining contact at the atomic scale," *Tribology letters*, vol. 39, no. 3, pp. 329–348, 2010.

[12] M. Dienwiebel, G. S. Verhoeven, N. Pradeep, J. W. Frenken, J. A. Heimberg, and H. W. Zandbergen, "Superlubricity of graphite," *Physical Review Letters*, vol. 92, no. 12, p. 126101, 2004.

[13] H. Pollock, *Fundamentals of Friction*. Springer Science & Business Media, 1992, vol. 220.

[14] B. N. Persson, *Sliding Friction: Physical Principles and Applications*. Springer Science & Business Media, 2000, vol. 1.

[15] A. M. Homola, J. N. Israelachvili, P. M. McGuiggan, and M. L. Gee, "Fundamental experimental studies in tribology: The transition from interfacial friction of undamaged molecularly smooth surfaces to normal friction with wear," *Wear*, vol. 136, no. 1, pp. 65–83, 1990.

[16] D. Dietzel, M. Feldmann, U. D. Schwarz, H. Fuchs, and A. Schirmeisen, "Scaling laws of structural lubricity," *Physical Review Letters*, vol. 111, no. 23, p. 235502, 2013.

[17] P. A. Romero, T. T. Järvi, N. Beckmann, M. Mrovec, and M. Moseler, "Coarse graining and localized plasticity between sliding nanocrystalline metals," *Physical Review Letters*, vol. 113, no. 3, p. 036101, 2014.

[18] M. H. Müser, "Theoretical aspects of superlubricity," in *Fundamentals of Friction and Wear*. Springer, 2007, pp. 177–199.

[19] C. Campaná and M. H. Müser, "Practical Greens function approach to the simulation of elastic semi-infinite solids," *Physical Review B*, vol. 74, no. 7, p. 075420, 2006.

[20] K. L. Johnson, *Contact Mechanics*. Cambridge University Press, 1985, http://dx.doi.org/10.1017/cbo9781139171731.

[21] R. D. Mindlin, "Compliance of elastic bodies in contact," *Journal of Applied Mechanics*, vol. 16, p. 259, 1949.

[22] I. L. Singer, H. M. Pollack, and O. Vingsbo, *Fundamentals of Friction: Macroscopic and Microscopic Processes (NATO Advanced Science Institute Series, Series E: Applied Sciences, Vol. 220)*. ASME International, 1994, vol. 61, no. 1, http://dx.doi.org/10.1115/1.2901414.

[23] J. P. Hirth and J. Lothe, *Theory of Dislocations*. John Wiley\ & Sons, 1982.

[24] D. Hull and D. J. Bacon, *Introduction to Dislocations, Fifth Edition*. Butterworth-Heinemann, 2011.

[25] F. Nabarro, "Fifty-year study of the Peierls-Nabarro stress," *Materials Science and Engineering: A*, vol. 234-236, pp. 67–76, aug 1997, http://dx.doi.org/10.1016/S0921-5093(97)00184-6.

[26] R. Phillips, *Crystals, defects and microstructures: modeling across scales*. Cambridge University Press, 2001.

[27] J. A. Hurtado and K.-S. Kim, "Scale effects in friction of single-asperity contacts. I. from concurrent slip to single-dislocation-assisted slip," *Proceedings of the Royal Society A: Mathematical, Physical and Engineering Sciences*, vol. 455, no. 1989, pp. 3363–3384, sep 1999, http://dx.doi.org/10.1098/rspa.1999.0455.

[28] J. A. Hurtado and K.-S.Kim, "Scale effects in friction of single-asperity contacts. II. multiple-dislocation-cooperated slip," *Proceedings of the Royal Society A: Mathematical, Physical and Engineering Sciences*, vol. 455, no. 1989, pp. 3385–3400, sep 1999, http://dx.doi.org/10.1098/rspa.1999.0456.

[29] Y. Gao, "A Peierls perspective on mechanisms of atomic friction," *Journal of the Mechanics and Physics of Solids*, vol. 58, no. 12, pp. 2023–2032, dec 2010, http://dx.doi.org/10.1016/j.jmps.2010.09.014.

[30] O. M. Braun and Y. S. Kivshar, *The Frenkel-Kontorova Model: Concepts, Methods, and Applications*. Springer Science & Business Media, 2004.

[31] M. Peyrard and S. Aubry, "Critical behaviour at the transition by breaking of analyticity in the discrete Frenkel-Kontorova model," *Journal of Physics C: Solid State Physics*, vol. 16, no. 9, p. 1593, 1983.

[32] M. Weiss and F.-J. Elmer, "Dry friction in the Frenkel-Kontorova-Tomlinson model: Static properties," *Physical Review B*, vol. 53, no. 11, p. 7539, 1996.

[33] J. A. Zimmerman, H. Gao, and F. F. Abraham, "Generalized stacking fault energies for embedded atom fcc metals," *Modelling and Simulation in Materials Science and Engineering*, vol. 8, no. 2, p. 103, 2000.

[34] M. Hirano and K. Shinjo, "Atomistic locking and friction," *Physical Review B*, vol. 41, pp. 11 837–11 851, Jun 1990, http://link.aps.org/doi/10.1103/PhysRevB.41.11837.

[35] M. Hirano, K. Shinjo, R. Kaneko, and Y. Murata, "Anisotropy of frictional forces in muscovite mica," *Physical Review Letters*, vol. 67, pp. 2642–2645, Nov 1991, http://link.aps.org/doi/10.1103/PhysRevLett.67.2642.

[36] D. Dietzel, T. Mönninghoff, C. Herding, M. Feldmann, H. Fuchs, B. Stegemann, C. Ritter, U. D. Schwarz, and A. Schirmeisen, "Frictional duality of metallic nanoparticles: Influence of particle morphology, orientation, and air exposure," *Physical Review B*, vol. 82, no. 3, p. 035401, 2010.

[37] Z. Liu, J. Yang, F. Grey, J. Z. Liu, Y. Liu, Y. Wang, Y. Yang, Y. Cheng, and Q. Zheng, "Observation of microscale superlubricity in graphite," *Physical Review Letters*, vol. 108, p. 205503, May 2012, http://link.aps.org/doi/10.1103/PhysRevLett.108.205503.

[38] M. M. van Wijk, M. Dienwiebel, J. W. M. Frenken, and A. Fasolino, "Superlubric to stick-slip sliding of incommensurate graphene flakes on graphite," *Physical Review B*, vol. 88, p. 235423, Dec 2013, http://link.aps.org/doi/10.1103/PhysRevB.88.235423.

[39] A. Filippov, M. Dienwiebel, J. Frenken, J. Klafter, and M. Urbakh, "Torque and twist against superlubricity," *Physical Review Letters*, vol. 100, no. 4, jan 2008, http://dx.doi.org/10.1103/PhysRevLett.100.046102.

[40] R. F. Voss, "Random fractals: self-affinity in noise, music, mountains, and clouds," *Physica D: Nonlinear Phenomena*, vol. 38, no. 1, pp. 362–371, 1989.

[41] B. Persson, "Elastoplastic contact between randomly rough surfaces," *Physical Review Letters*, vol. 87, no. 11, p. 116101, 2001.

[42] S. Akarapu, T. Sharp, and M. O. Robbins, "Stiffness of contacts between rough surfaces," *Physical Review Letters*, vol. 106, no. 20, p. 204301, 2011.

[43] G. P. Cherepanov, A. S. Balankin, and V. S. Ivanova, "Fractal fracture mechanicsA review," *Engineering Fracture Mechanics*, vol. 51, no. 6, pp. 997–1033, 1995.

[44] M. Kardar, G. Parisi, and Y.-C. Zhang, "Dynamic scaling of growing interfaces," *Physical Review Letters*, vol. 56, pp. 889–892, Mar 1986, http://link.aps.org/doi/10.1103/PhysRevLett.56.889.

[45] N. Prodanov, W. Dapp, and M. Mser, "On the contact area and mean gap of rough, elastic contacts: Dimensional analysis, numerical corrections, and reference data," *Tribology Letters*, vol. 53, no. 2, pp. 433–448, 2014, http://dx.doi.org/10.1007/s11249-013-0282-z.

[46] G. Carbone and F. Bottiglione, "Asperity contact theories: Do they predict linearity between contact area and load?" *Journal of the Mechanics and Physics of Solids*, vol. 56, no. 8, pp. 2555–2572, 2008.

[47] A. Bush, R. Gibson, and T. Thomas, "The elastic contact of a rough surface," *Wear*, vol. 35, no. 1, pp. 87–111, 1975.

[48] B. N. Persson, "Contact mechanics for randomly rough surfaces," *Surface Science Reports*, vol. 61, no. 4, pp. 201–227, 2006.

[49] B. N. J. Persson "Theory of rubber friction and contact mechanics," *The Journal of Chemical Physics*, vol. 115, no. 8, pp. 3840–3861, 2001.

[50] S. Hyun and M. O. Robbins, "Elastic contact between rough surfaces: Effect of roughness at large and small wavelengths," *Tribology International*, vol. 40, no. 10, pp. 1413–1422, 2007.

[51] L. T. Kong, G. Bartels, C. Campañá, C. Denniston, and M. H. Müser, "Implementation of Green's function molecular dynamics: An extension to LAMMPS," *Computer Physics Communications*, vol. 180, no. 6, pp. 1004–1010, 2009.

[52] R. W. Carpick, D. F. Ogletree, and M. Salmeron, "A general equation for fitting contact area and friction vs load measurements," *Journal of Colloid and Interface Science*, vol. 211, no. 2, pp. 395–400, 1999.

[53] C. Campañá, B. Persson, and M. Müser, "Transverse and normal interfacial stiffness of solids with randomly rough surfaces," *Journal of Physics: Condensed Matter*, vol. 23, no. 8, p. 085001, 2011.

[54] J. R. Kermode, T. Albaret, D. Sherman, N. Bernstein, P. Gumbsch, M. Payne, G. Csányi, and A. De Vita, "Low-speed fracture instabilities in a brittle crystal," *Nature*, vol. 455, no. 7217, pp. 1224–1227, 2008.

[55] S. Kohlhoff, P. Gumbsch, and H. Fischmeister, "Crack propagation in bcc crystals studied with a combined finite-element and atomistic model," *Philosophical Magazine A*, vol. 64, no. 4, pp. 851–878, 1991.

[56] G. Moras, L. C. Ciacchi, C. Elsässer, P. Gumbsch, and A. De Vita, "Atomically smooth stress-corrosion cleavage of a hydrogen-implanted crystal," *Physical Review Letters*, vol. 105, no. 7, p. 075502, 2010.

[57] V. A. Shchukin and D. Bimberg, "Spontaneous ordering of nanostructures on crystal surfaces," *Reviews of Modern Physics*, vol. 71, no. 4, p. 1125, 1999.

[58] R. E. Miller and E. Tadmor, "A unified framework and performance benchmark of fourteen multiscale atomistic/continuum coupling methods," *Modelling and Simulation in Materials Science and Engineering*, vol. 17, no. 5, p. 053001, 2009.

[59] A. Ramasubramaniam and E. A. Carter, "Coupled quantum–atomistic and quantum–continuum mechanics methods in materials research," *MRS Bulletin*, vol. 32, no. 11, pp. 913–918, 2007.

[60] R. E. Miller and E. B. Tadmor, "Hybrid continuum mechanics and atomistic methods for simulating materials deformation and failure," *MRS Bulletin*, vol. 32, no. 11, pp. 920–926, 2007.

[61] V. Shenoy, R. Miller, E. Tadmor, D. Rodney, R. Phillips, and M. Ortiz, "An adaptive finite element approach to atomic-scale mechanicsthe quasicontinuum method," *Journal of the Mechanics and Physics of Solids*, vol. 47, no. 3, pp. 611–642, 1999.

[62] K. Ohsawa, E. Kuramoto, and T. Suzuki, "Lattice statics Green's function for a semi-infinite crystal," *Philosophical Magazine A*, vol. 74, no. 2, pp. 431–449, 1996.

[63] V. Tewary and R. Thomson, "Lattice statics of interfaces and interfacial cracks in bimaterial solids," *Journal of materials research*, vol. 7, no. 04, pp. 1018–1028, 1992.

[64] R. Thomson, S. Zhou, A. Carlsson, and V. Tewary, "Lattice imperfections studied by use of lattice Greens functions," *Physical Review B*, vol. 46, no. 17, p. 10613, 1992.

[65] V. Tewary, "Green-function method for lattice statics," *Advances in Physics*, vol. 22, no. 6, pp. 757–810, 1973.

[66] E. Montroll, G. Weiss, and I. Ipatova, "Theory of lattice dynamics in the harmonic approximation," *Solid State Physics, Suppl*, vol. 3, 1971.

[67] D. Read and V. Tewary, "Multiscale model of near-spherical germanium quantum dots in silicon," *Nanotechnology*, vol. 18, no. 10, p. 105402, 2007.

[68] V. Tewary and D. Read, "Integrated Green's function molecular dynamics method for multiscale modeling of nanostructures: Application to au nanoisland in Cu," *Computer Modeling in Engineering and Sciences*, vol. 6, pp. 359–372, 2004.

[69] V. Tewary, "Multiscale Greens-function method for modeling point defects and extended defects in anisotropic solids: Application to a vacancy and free surface in copper," *Physical Review B*, vol. 69, no. 9, p. 094109, 2004.

[70] S. Barbot and Y. Fialko, "A unified continuum representation of post-seismic relaxation mechanisms: Semi-analytic models of afterslip, poroelastic rebound and viscoelastic flow," *Geophysical Journal International*, vol. 182, no. 3, pp. 1124–1140, 2010.

[71] C. L. Amba-rao, "Fourier transform methods in elasticity problems and an application," *Journal of the Franklin Institute*, vol. 287, no. 3, pp. 241–249, 1969.

[72] I. N. Sneddon, "The relation between load and penetration in the axisymmetric Boussinesq problem for a punch of arbitrary profile," *International Journal of Engineering Science*, vol. 3, no. 1, pp. 47–57, 1965.

[73] M. Ghazisaeidi and D. Trinkle, "Lattice Greens function for crystals containing a planar interface," *Physical Review B*, vol. 82, no. 6, p. 064115, 2010.

[74] W. Cai, M. de Koning, V. V. Bulatov, and S. Yip, "Minimizing boundary reflections in coupled-domain simulations," *Physical Review Letters*, vol. 85, no. 15, p. 3213, 2000.

[75] C. Campañá, "Using Greens function molecular dynamics to rationalize the success of asperity models when describing the contact between self-affine surfaces," *Physical Review E*, vol. 78, no. 2, p. 026110, 2008.

[76] C. Campañá, M. H. Müser, and M. O. Robbins, "Elastic contact between self-affine surfaces: Comparison of numerical stress and contact correlation functions with analytic predictions," *Journal of Physics: Condensed Matter*, vol. 20, no. 35, p. 354013, 2008.

[77] C. Campaná and M. H. Müser, "Contact mechanics of real vs. randomly rough surfaces: A Green's function molecular dynamics study," *EPL (Europhysics Letters)*, vol. 77, no. 3, p. 38005, 2007.

[78] Y. Saito, "Elastic lattice Green's function in three dimensions," *Journal of the Physical Society of Japan*, vol. 73, no. 7, pp. 1816–1826, 2004, http://dx.doi.org/10.1143/JPSJ.73.1816.

[79] W. B. Dapp, A. Lücke, B. N. Persson, and M. H. Müser, "Self-affine elastic contacts: Percolation and leakage," *Physical Review Letters*, vol. 108, no. 24, p. 244301, 2012.

[80] S. J. Plimpton and A. P. Thompson, "Computational aspects of many-body potentials," *MRS Bulletin*, vol. 37, no. 05, pp. 513–521, 2012.

[81] S. Plimpton, "Fast parallel algorithms for short-range molecular dynamics," *Journal of Computational Physics*, vol. 117, no. 1, pp. 1–19, 1995.

[82] The dissipation in bulk solids is typically proportional to some power of the three dimensional wavevector $\vec{q}$. The modes at the Γ-point of the two dimensional Brillouin zone of the surface will have a nonzero normal component q_z of this wavevector. This is the reason collective surface excitations decay at all. Their relaxation time is however long and diverges as $q_z \to 0$.

[83] L. Falicov and F. Yndurain, "Model calculation of the electronic structure of a (111) surface in a diamond-structure solid," *Journal of Physics C: Solid State Physics*, vol. 8, no. 2, p. 147, 1975.

[84] V. Velasco and F. Ynduráin, "Lattice vibrations at (111) surfaces and stacking faults in transition metals: Ni," *Surface Science*, vol. 85, no. 1, pp. 107–124, 1979.

[85] M. O. Robbins and B. Koiller, "Localization properties of random and partially ordered one-dimensional systems," *Physical Review B*, vol. 32, no. 7, p. 4576, 1985.

[86] C. G. da Silva and B. Koiller, "Local density of states in a disordered chain: A renormalization group approach," *Solid State Communications*, vol. 40, no. 3, pp. 215–219, 1981.

[87] N. W. Ashcroft and N. D. Mermin, *Solid State Physics*. Brooks Cole, Philadelphia, 1976, 2010.

[88] R. P. Gupta, "Lattice relaxation at a metal surface," *Physical Review B*, vol. 23, no. 12, p. 6265, 1981.

[89] M. S. Daw and M. I. Baskes, "Embedded-atom method: Derivation and application to impurities, surfaces, and other defects in metals," *Physical Review B*, vol. 29, pp. 6443–6453, Jun 1984, http://link.aps.org/doi/10.1103/PhysRevB.29.6443.

[90] S. M. Foiles and M. I. Baskes, "Contributions of the embedded-atom method to materials science and engineering," *MRS Bulletin*, vol. 37, no. 05, pp. 485–491, 2012.

[91] K. Huang, *Statistical Mechanics*. Wiley, New York, 1987.

[92] L. Onsager, "Crystal statistics. I. A two-dimensional model with an order-disorder transition," *Physical Review*, vol. 65, no. 3-4, p. 117, 1944.

[93] E. Ising, "Beitrag zur theorie des ferromagnetismus," *Zeitschrift für Physik A Hadrons and Nuclei*, vol. 31, no. 1, pp. 253–258, 1925.

[94] M. E. Peskin and D. V. Schroeder, *An Introduction to Quantum Field Theory*. Westview Press, Boulder, CO, 1995.

[95] G. Grochola, S. P. Russo, and I. K. Snook, "On fitting a gold embedded atom method potential using the force matching method," *The Journal of Chemical Physics*, vol. 123, no. 20, p. 204719, 2005.

[96] L. Pastewka, M. Mrovec, M. Moseler, and P. Gumbsch, "Bond order potentials for fracture, wear, and plasticity," *MRS Bulletin*, vol. 37, no. 05, pp. 493–503, 2012.

[97] This potential is implemented as `lj/smooth` in LAMMPS.[80,81]

[98] H. Hertz, "On the contact of elastic solids," *J. reine angew. Math*, vol. 92, no. 156-171, p. 110, 1881.

[99] J. J. Vlassak and W. Nix, "Measuring the elastic properties of anisotropic materials by means of indentation experiments," *Journal of the Mechanics and Physics of Solids*, vol. 42, no. 8, pp. 1223–1245, 1994.

[100] J. Vlassak and W. Nix, "Indentation modulus of elastically anisotropic half spaces," *Philosophical Magazine A*, vol. 67, no. 5, pp. 1045–1056, 1993.

[101] M. T. Knippenberg, P. T. Mikulski, and J. A. Harrison, "Effects of tip geometry on interfacial contact forces," *Modelling and Simulation in Materials Science and Engineering*, vol. 18, no. 3, p. 034002, 2010.

[102] B. Luan and M. O. Robbins, "Contact of single asperities with varying adhesion: Comparing continuum mechanics to atomistic simulations," *Physical Review E*, vol. 74, no. 2, p. 026111, 2006.

[103] P. Meakin, *Fractals, scaling and growth far from equilibrium*. Cambridge University Press, 1998, vol. 5.

[104] C. Putignano, L. Afferrante, G. Carbone, and G. Demelio, "The influence of the statistical properties of self-affine surfaces in elastic contacts: A numerical investigation," *Journal of the Mechanics and Physics of Solids*, vol. 60, no. 5, pp. 973–982, 2012.

[105] H. Tsuzuki, P. S. Branicio, and J. P. Rino, "Structural characterization of deformed crystals by analysis of common atomic neighborhood," *Computer Physics Communications*, vol. 177, no. 6, pp. 518–523, 2007.

[106] J. D. Honeycutt and H. C. Andersen, "Molecular dynamics study of melting and freezing of small Lennard-Jones clusters," *Journal of Physical Chemistry*, vol. 91, no. 19, pp. 4950–4963, 1987.

[107] G. Anciaux and J.-F. Molinari, "Contact mechanics at the nanoscale, a 3d multiscale approach," *International journal for numerical methods in engineering*, vol. 79, no. 9, pp. 1041–1067, 2009.

[108] L. Shilkrot, R. Miller, and W. Curtin, "Coupled atomistic and discrete dislocation plasticity," *Physical Review Letters*, vol. 89, no. 2, p. 025501, 2002.

[109] N. Asmar and G. Jones, *Applied Complex Analysis with Partial Differential Equations*. Prentice Hall, 2002.

[110] R. W. Hockney, "Potential calculation and some applications," Langley Research Center, Hampton, Va., Tech. Rep., 1970.

[111] J. Li and E. Berger, "A semi-analytical approach to three-dimensional normal contact problems with friction," *Computational Mechanics*, vol. 30, no. 4, pp. 310–322, 2003.

[112] R. Pohrt and Q. Li, "Complete boundary element formulation for normal and tangential contact problems," *Physical Mesomechanics*, vol. 17, no. 4, pp. 334–340, 2014.

[113] E. Tadmor, F. Legoll, W. K. Kim, L. M. Dupuy, and R. E. Miller, unpublished.

[114] L. M. Dupuy, E. B. Tadmor, R. E. Miller, and R. Phillips, "Finite-temperature quasicontinuum: Molecular dynamics without all the atoms," *Physical Review Letters*, vol. 95, no. 6, p. 060202, 2005.

[115] F. P. Bowden and D. Tabor, *The Friction and Lubrication of Solids.* Oxford : Clarendon Press, 1964.

[116] L. Pei, S. Hyun, J. Molinari, and M. O. Robbins, "Finite element modeling of elasto-plastic contact between rough surfaces," *Journal of the Mechanics and Physics of Solids*, vol. 53, no. 11, pp. 2385–2409, 2005.

[117] D. Bellow and D. Nelson, "On the experimental investigation of the stiffness of clamped machined surfaces," *Experimental Mechanics*, vol. 10, no. 12, pp. 506–513, 1970.

[118] B. Persson, "Relation between interfacial separation and load: A general theory of contact mechanics," *Physical Review Letters*, vol. 99, no. 12, p. 125502, 2007.

[119] B. N. J. Persson, "Capillary adhesion between elastic solids with randomly rough surfaces," *Journal of Physics: Condensed Matter*, vol. 20, no. 31, p. 315007, 2008.

[120] M. Gonzalez-Valadez, A. Baltazar, and R. Dwyer-Joyce, "Study of interfacial stiffness ratio of a rough surface in contact using a spring model," *Wear*, vol. 268, no. 3, pp. 373–379, 2010.

[121] B. Persson and P. Ballone, "Squeezing lubrication films: Layering transition for curved solid surfaces with long-range elasticity," *The Journal of Chemical Physics*, vol. 112, no. 21, pp. 9524–9542, 2000.

[122] M. H. Müser, "Rigorous field-theoretical approach to the contact mechanics of rough elastic solids," *Physical Review Letters*, vol. 100, no. 5, p. 055504, 2008.

[123] M. Benz, K. J. Rosenberg, E. J. Kramer, and J. N. Israelachvili, "The deformation and adhesion of randomly rough and patterned surfaces," *The Journal of Physical Chemistry B*, vol. 110, no. 24, pp. 11 884–11 893, 2006.

[124] B. Lorenz and B. Persson, "Interfacial separation between elastic solids with randomly rough surfaces: Comparison of experiment with theory," *Journal of Physics: Condensed Matter*, vol. 21, no. 1, p. 015003, 2009.

[125] C. Yang and B. Persson, "Contact mechanics: Contact area and interfacial separation from small contact to full contact," *Journal of Physics: Condensed Matter*, vol. 20, no. 21, p. 215214, 2008.

[126] B. Luan and M. O. Robbins, "Hybrid atomistic/continuum study of contact and friction between rough solids," *Tribology letters*, vol. 36, no. 1, pp. 1–16, 2009.

[127] Simulations performed with LAMMPS http://lammps.sandia.gov.

[128] K. Shinjo and M. Hirano, "Dynamics of friction: Superlubric state," *Surface Science*, vol. 283, no. 1, pp. 473–478, 1993.

[129] B. Persson and E. Tosatti, "Theory of friction: Elastic coherence length and earthquake dynamics," *Solid State Communications*, vol. 109, no. 12, pp. 739–744, 1999.

[130] A. Almqvist, C. Campaná, N. Prodanov, and B. Persson, "Interfacial separation between elastic solids with randomly rough surfaces: comparison between theory and numerical techniques," *Journal of the Mechanics and Physics of Solids*, vol. 59, no. 11, pp. 2355–2369, 2011.

[131] B. B. Mandelbrot, *The Fractal Geometry of Nature*. Macmillan, 1983, vol. 173.

[132] B. Persson, O. Albohr, U. Tartaglino, A. Volokitin, and E. Tosatti, "On the nature of surface roughness with application to contact mechanics, sealing, rubber friction and adhesion," *Journal of Physics: Condensed Matter*, vol. 17, no. 1, p. R1, 2005.

[133] S. Hyun and M. O. Robbins, "Elastic contact between rough surfaces: Effect of roughness at large and small wavelengths," *Tribology International*, vol. 40, no. 10, pp. 1413–1422, 2007.

[134] W. Manners and J. Greenwood, "Some observations on Persson's diffusion theory of elastic contact," *Wear*, vol. 261, no. 5, pp. 600–610, 2006.

[135] L. Pastewka, N. Prodanov, B. Lorenz, M. H. Müser, M. O. Robbins, and B. N. Persson, "Finite-size scaling in the interfacial stiffness of rough elastic contacts," *Physical Review E*, vol. 87, no. 6, p. 062809, 2013.

[136] M. Hirano, K. Shinjo, R. Kaneko, and Y. Murata, "Anisotropy of frictional forces in muscovite mica," *Physical Review Letters*, vol. 67, pp. 2642–2645, Nov 1991, http://link.aps.org/doi/10.1103/PhysRevLett.67.2642.

[137] A. Erdemir and J.-M. Martin, *Superlubricity, Chapter 2, Hirano M.* Elsevier Science, 2007, http://www.sciencedirect.com/science/book/9780444527721.

[138] M. Hirano, K. Shinjo, R. Kaneko, and Y. Murata, "Observation of superlubricity by scanning tunneling microscopy," *Physical Review Letters*, vol. 78, pp. 1448–1451, Feb 1997, http://link.aps.org/doi/10.1103/PhysRevLett.78.1448.

[139] J. Martin, C. Donnet, T. Le Mogne, and T. Epicier, "Superlubricity of molybdenum disulphide," *Physical Review B*, vol. 48, no. 14, p. 10583, 1993.

[140] A. S. de Wijn, "(In) commensurability, scaling, and multiplicity of friction in nanocrystals and application to gold nanocrystals on graphite," *Physical Review B*, vol. 86, no. 8, p. 085429, 2012.

[141] J. Ringlein and M. O. Robbins, "Understanding and illustrating the atomic origins of friction," *American Journal of Physics*, vol. 72, no. 7, pp. 884–891, 2004.

[142] M. H. Müser, M. Urbakh, and M. O. Robbins, "Statistical mechanics of static and low-velocity kinetic friction," *Advances in Chemical Physics*, vol. 126, pp. 187–272, 2003.

[143] M. Cieplak, E. D. Smith, and M. O. Robbins, "Molecular origins of friction: The force on adsorbed layers," *Science*, vol. 265, no. 5176, pp. 1209–1212, 1994.

[144] M. Tomassone, J. Sokoloff, A. Widom, and J. Krim, "Dominance of phonon friction for a xenon film on a silver (111) surface," *Physical Review Letters*, vol. 79, no. 24, p. 4798, 1997.

[145] A. Liebsch, S. Goncalves, and M. Kiwi, "Electronic versus phononic friction of xenon on silver," *Physical Review B*, vol. 60, no. 7, p. 5034, 1999.

[146] N. Varini, A. Vanossi, R. Guerra, D. Mandelli, R. Capozza, and E. Tosatti, "Static friction scaling of physisorbed islands: The key is in the edge," *Nanoscale*, vol. 7, no. 5, pp. 2093–2101, 2015.

[147] J. Friedel and P.-G. de Gennes, "Friction between incommensurate crystals," *Philosophical Magazine*, vol. 87, no. 1, pp. 39–49, 2007.

[148] A. Merkle and L. Marks, "A predictive analytical friction model from basic theories of interfaces, contacts and dislocations," *Tribology Letters*, vol. 26, no. 1, pp. 73–84, 2007.

[149] M. Müser, "Dry friction between flat surfaces: multistable elasticity vs. material transfer and plastic deformation," *Tribology Letters*, vol. 10, no. 1-2, pp. 15–22, 2001.

[150] W. K. Kim and M. L. Falk, "Atomic-scale simulations on the sliding of incommensurate surfaces: The breakdown of superlubricity," *Physical Review B*, vol. 80, p. 235428, Dec 2009, http://link.aps.org/doi/10.1103/PhysRevB.80.235428.

[151] Note that for $\nu \neq 0.5$ frictional stresses change the lattice constant and thus the commensurability.

[152] R. Choudhury, C. Gattinoni, G. Makov, and A. De Vita, "Molecular dynamics studies of the dissociated screw dislocation in silicon," *Journal of Physics: Condensed Matter*, vol. 22, no. 7, p. 074210, 2010.

[153] W. Cai, V. V. Bulatov, J. Chang, J. Li, S. Yip, F. Nabarro, and J. Hirth, *Dislocation core effects on mobility.* Elsevier, Amsterdam, 2004, vol. 12.

[154] G. Zilibotti and M. Righi, "Ab initio calculation of the adhesion and ideal shear strength of planar diamond interfaces with different atomic structure and hydrogen coverage," *Langmuir*, vol. 27, no. 11, pp. 6862–6867, 2011.

[155] A. Volmer and T. Natterman, "Towards a statistical theory of solid dry friction," *Z. Phys. B*, vol. 104, pp. 363–371, 1997.

[156] B. Persson and E. Tosatti, "Theory of friction: elastic coherence length and earthquake dynamics," pp. 179–189, 1996.

[157] C. Caroli and P. Nozieres, "Dry friction as a hysteretic elastic response," in *Physics of sliding friction.* Springer, 1996, pp. 27–49.

[158] M. H. Müser, "Structural lubricity: Role of dimension and symmetry," *EPL (Europhysics Letters)*, vol. 66, no. 1, p. 97, 2004. [Online]. Available: http://stacks.iop.org/0295-5075/66/i=1/a=097

[159] T. Liang, W. G. Sawyer, S. S. Perry, S. B. Sinnott, and S. R. Phillpot, "First-principles determination of static potential energy surfaces for atomic friction in MoS2 and MoO3," *Physical Review B*, vol. 77, no. 10, p. 104105, 2008.

[160] J. R. Rice, "Dislocation nucleation from a crack tip: an analysis based on the Peierls concept," *Journal of the Mechanics and Physics of Solids*, vol. 40, no. 2, pp. 239–271, 1992.

[161] L. Pastewka, T. A. Sharp, and M. O. Robbins, "Seamless elastic boundaries for atomistic calculations," *Physical Review B*, vol. 86, no. 7, p. 075459, 2012, http://dx.doi.org/10.1103/physrevb.86.075459.

[162] Y. Liao and L. Marks, "Modeling of thermal-assisted dislocation friction," *Tribology letters*, vol. 37, no. 2, pp. 283–288, 2010.

[163] D. Berman, S. A. Deshmukh, S. K. R. S. Sankaranarayanan, A. Erdemir, and A. V. Sumant, "Macroscale superlubricity enabled by graphene nanoscroll formation," *Science*, vol. 348, no. 6239, pp. 1118–1122, 2015, http://www.sciencemag.org/content/348/6239/1118.abstract.

Vita

Tristan Sharp grew up in Encinitas, California where he attended La Costa Canyon High School. He enrolled at Harvey Mudd College in Claremont, California and studied Physics. While an undergraduate Tristan served as president of the Barnstormers' Aviation Club and concentrated his research on computational physics with applications to the aerospace industry. On a year-long project he designed, built, and fielded a two-phase fluid flow experiment in micro-gravity aboard NASA's Weightless Wonder aircraft. His thesis project consisted of computational modeling and experiments of scattering of light by soot particles.

Tristan worked for three years at a leading aerospace research and development firm, Areté Associates, in Los Angeles, California where he designed high-speed signal processing and computational physics algorithms, learning from generous mathematicians, scientists, and engineers. In parallel Tristan took classes at the University of California, Los Angeles, attaining a Masters Degree in Mechanical and Aerospace Engineering with a specialization in Computational Fluid Mechanics. In 2009 Tristan moved to Maryland to work with Dr. Mark O. Robbins at The Johns Hopkins University on the atomic-scale mechanics described in this thesis. In 2016 Tristan was awarded his PhD in Physics and accepted a post-doctoral position at the University of Pennsylvania.